Journal of
Materials Chemistry A

ROYAL SOCIETY
OF CHEMISTRY

REVIEW

View Article Online
View Journal | View Issue

Check for updates

Cite this: *J. Mater. Chem. A*, 2021, **9**, 19554

Advances in SnO_2-based perovskite solar cells: from preparation to photovoltaic applications

Pengfei Wu,[ab] Shirong Wang, *[ab] Xianggao Li [ab] and Fei Zhang *[ab]

Received 16th May 2021
Accepted 22nd July 2021

DOI: 10.1039/d1ta04130d

rsc.li/materials-a

Perovskite solar cells (PSCs) have recently demonstrated a rapid power conversion efficiency of above 25%. In terms of physical properties, SnO_2 is similar to TiO_2 but with stronger charge extraction at the interface. Furthermore, the SnO_2 electron transporting layer (ETL) is prepared using new, simple, and efficient methods, resulting in high-performance PSCs. This review initially described recent progress in SnO_2 nanostructures and preparation methods. The passivation options were then divided into elemental doping, bilayer alterations, and interfacial modifications. Finally, we discussed the challenges and limitations of SnO_2 ETL-based PSCs and made recommendations for further research.

1. Introduction

Nowadays, perovskite solar cells (PSCs) have attracted substantial attention due to low expense, facile production, and high power conversion efficiency (PCE).[1–5] Besides, the rapid development of theoretical and practical research has boosted its PCE from 3.8% [6] to 25.5% [3,7–12] in just ten years, which is close to that of polycrystalline silicon solar energy cells (Fig. 1a).

The general chemical formula of perovskite is ABX_3, in which A involves an organic cation group or inorganic metal cations such as Methylammonium ($CH_3NH_3^+$), formamidinium ($NH_2CH{=}NH_2^+$), as well as cesium (Cs^+); B is generally a heavy metal cation such as lead(II) (Pb^{2+}) and tin(II) (Sn^{2+}); X is commonly a halide ion including chlorine (Cl^-), bromide (Br^-), or iodine (I^-).[13,14] (Fig. 1b) The Goldschmidt tolerance factor (t),[15] is a simple way to check whether or not specific compositions can form a stable perovskite structure.

$$t = \frac{r_A + r_X}{\sqrt{2}(r_B + r_X)}$$

where r_A, r_B, and r_X represent the corresponding ionic radius of A, B and X, respectively. The 3D perovskite structure can be stable only when t is located in the range of ~0.8–1.0.[16]

PSC structures are always classified into two types: n-i-p structures and p-i-n structures. The n-i-p structures are of two types: n-i-p mesoporous and n-i-p planar structures, whereas the p-i-n structures are only p-i-n planar structures (Fig. 1c–e).[4,17,18] The n-i-p mesoporous structures are usually composed of a transparent conductive electrode such as fluorine-doped tin oxide (FTO) and indium tin oxide (ITO), an electron transporting layer (ETL), a mesoporous scaffold layer (which is

---

[a] *School of Chemical Engineering and Technology, Tianjin University, Tianjin, 300072, China. E-mail: wangshirong@tju.edu.cn; fei_zhang@tju.edu.cn*

[b] *Collaborative Innovation Center of Chemical Science and Engineering (Tianjin), Tianjin, 300072, China*

Pengfei Wu is currently a PhD candidate in Applied Chemistry at Tianjin University under the supervision of Prof. Shirong Wang. He received his B. S. degree (2019) from China University of Petroleum (East China), China. His current research focuses on low-dimensional perovskites and efficient perovskite solar cells.

Shirong Wang is currently a Professor in the School of Chemical Engineering and Technology at Tianjin University. She received her B. S. degree (1991) and a PhD degree in applied chemistry at Tianjin University. She worked as a postdoctoral researcher in the State Key Laboratory of Fine Chemicals at the Dalian University of Technology. Her main research interests include perovskite solar cells, organic/quantum dot light-emitting diodes, and metal halide perovskite nanocrystals.

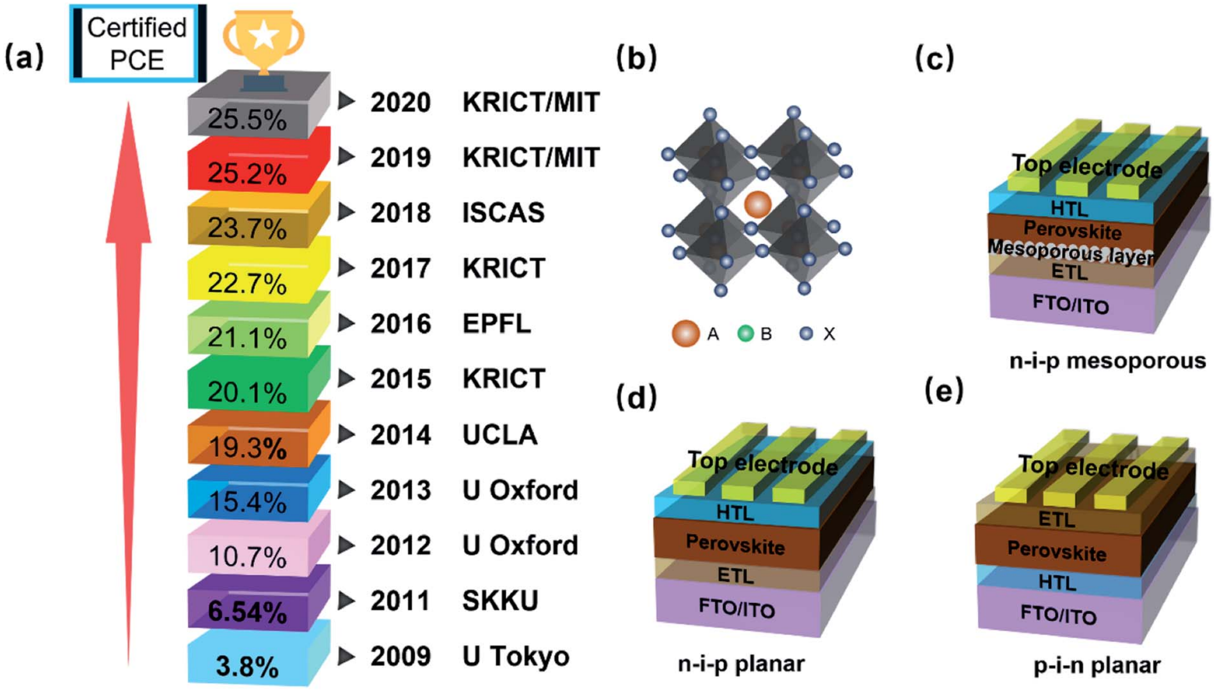

Fig. 1 (a) Brief development history of PSCs (2009,[6] 2011,[28] 2012,[29] 2013,[30] 2014,[31] 2015,[32] 2016,[33] 2017,[34] 2018,[35] 2019,[36] and 2020,[7]). (b) Crystal structure of cubic for metal halide perovskite. (c) PSCs with an n-i-p mesoporous structure. (d) PSCs with a regular n-i-p planar structure. (e) PSCs with a p-i-n planar structure.

always TiO_2 or Al_2O_3), a perovskite absorption layer, a hole transporting layer (HTL) and a top electrode. However, the TiO_2 mesoporous layer is always post-treated at high temperatures (typically above 450 °C) to increase the conductivity and remove the organic material.[19–25] By contrast, the planar structure of n-i-p PSCs without a mesoporous scaffold also achieves a similar efficient power output and long-term stability to the device with the mesoporous configuration.[26,27]

TiO_2 is a widely utilized ETL in PSCs for n-i-p planar structures due to its proper bandgap and good transmittance.[37–40] However, when tested under continuous light illumination, TiO_2 obtains electrons from I^-, leading to perovskite cubic structural damage and generation of I_2.[41–43] Furthermore, TiO_2 has a disadvantage of poor electron mobility (10^{-5} cm^2 V^{-1} s^{-1}) due to impaired intrinsic electron mobility (<1 cm^2 V^{-1} s^{-1}).[44] Furthermore, organic residuals must be removed using high-

---

Xianggao Li is currently a Professor in the School of Chemical Engineering and Technology and the Department of Fine Chemical Engineering Director at Tianjin University. He received his B. S. degree in 1983 from Hunan University and a PhD. degree from the School of Chemical Engineering and Technology at Tianjin University, respectively. His main research interests include perovskite solar cells, organic/quantum dot light-emitting diodes, and metal halide perovskite nanocrystals.

Fei Zhang is currently a Professor in the School of Chemical Engineering and Technology at Tianjin University. He received his B.Eng. (2011) and a PhD degree (2017) under the supervision of Prof. Shirong Wang at Tianjin University. He was a visiting PhD student in LPI at Ecole Polytechnique Fédérale de Lausanne (EPFL) under the supervision of Prof. Michael Grätzel and Dr Shaik Mohammed Zakeeruddin. Then, he worked as a Postdoctoral Researcher in the Chemistry and Nanoscience Center at the National Renewable Energy Laboratory under Dr.Kai Zhu's supervision. His interests concentrate on synthesizing low-dimensional perovskites, lead-free perovskites, and device engineering for perovskite optoelectrical devices.

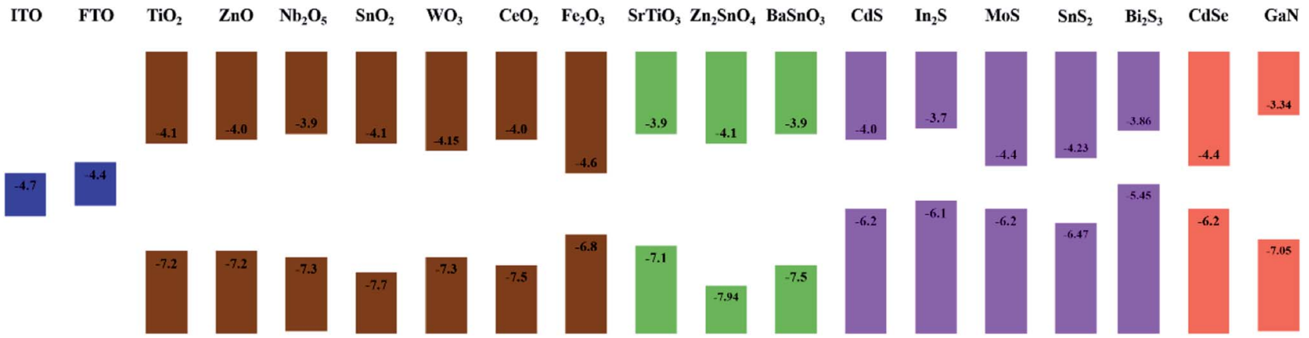

Fig. 2 Conduction band (CB) and valence band (VB) of widely introduced inorganic metal materials as ETLs in PSCs. (blue: metal oxides: green: ternary metal; yellow: metal sulfide; pink: CdSe; and purple: GaN).

temperature procedures, which will take a significant amount of time and energy. For high-performance PSCs, an appropriate and chemically stable ETL is required.

For efficient and stable PSCs, we must adhere to key ETL material principles: (a) high transmittance with minimum optical energy loss, (b) appropriate bandgap matching, (c) high conductivity, (d) low cost and (e) good reproducibility.[45–48] Many metal oxides with unique optical and electrical properties have been reported as potential candidates for replacing TiO_2 (Fig. 2), including metal oxides (ZnO,[49–53] In_2O_3,[54] Nb_2O_5,[55,56] WO_3,[57,58] Fe_2O_3,[59–62] and CeO_2 [63,64]) ternary metal oxides (Zn_2SnO_4,[65,66] $BaSnO_3$ [67–69] and $SrTiO_4$ [70,71]), metal sulfides (MoS,[72,73] CdS,[74–76] In_2S_3,[73] SnS_2 [77] and Bi_2S_3 [78]), GaN[79] and CdSe;[80,81] and $InGaZnO_4$.[82] However, some drawbacks still exist, like low PCE, poor interfacial contact, or high energy consumption.

Since the first report of 6.5% by Dai *et al.* and the subsequent report of above 15% by Yan *et al.* in 2015,[83,84] the performance of SnO_2-based PSCs has exceeded 25%, making SnO_2 an appealing ETL in PSCs and is considered a potential alternative instead of $TiO_2 \cdot SnO_2$ possesses the following remarkable properties: (1) depth CBM and optimal energy level alignment;[85] (2) high bulk electron mobility (significantly greater than TiO_2 ETL) and high conductivity;[86,87] (3) large bandgap (3.6–4.5 eV) and high optical transparency;[88,89] (4) high-temperature flexible deposition; and (5) outstanding stability under light, heat, and moisture, with minimal photoactivity.[90,91] TiO_2 in PSCs usually requires a mesoporous layer and especially high-temperature post-treatment (above 450 °C) to get dense with superior conductivity and crystallinity whether in a spin coating or spraying method, which costs more energy and expense. The SnO_2 ETL is often achieved using spin coating and chemical bath deposition, requiring just post-treatment at low temperatures ($\leq$200 °C), which is advantageous for a large-scale preparation.

In this review, we present an overview of the use of SnO_2 in PSCs, including standard preparation procedures, SnO_2 nanostructures, and performance optimization techniques such as elemental doping, surface modifications, and bilayer design. Then, we go into hysteresis and stability issues in further detail. Finally, we explore the problems and limits of SnO_2 ETL-based PSCs, as well as possible future research directions.

2. Preparation methods of SnO_2

The SnO_2 film is typically prepared through solution processing, chemical bath deposition (CBD), and atomic layer deposition (ALD). Recently, emerging methods for deposition of SnO_2 such as e-beam evaporation, magnetron sputtering, and electrochemical deposition are also reported to improve the conformability of SnO_2 for flexible and large-scale PSCs. Fig. 3 shows the schematic illustration of various processing methods for SnO_2 ETLs. We just picked some of the representative data of reported different preparation methods, even though other factors may have an impact on the performance. So, here, we have talked more about performance optimization strategies in detail in Section 4. Aside from these, the PCE is also influenced by the rigid or flexible substrate, preparation environment (N_2 or air), and electrode types.

2.1 Solution-processable method

The solution process contains the thermal decomposition method, sol–gel method, deposition of synthesized SnO_2 nanoparticles (NPs), and commercialized SnO_2 colloidal precursors.[92–94] In the meantime, spin-coating,[95–98] spray-coating,[99–101] slot-die coating,[100,102,103] roll-to-roll microgravity printing,[104] blade-coating[105,106] and inkjet-printing[107,108] are valuable technologies to fabricate quality SnO_2 films.

2.1.1 Thermal decomposition method. For thermal decompositions, Sn-based salts ($SnCl_2$[109,110] or $SnCl_4$,[111–113] or their hydrates $SnCl_2 \cdot 2H_2O$[114,115] or $SnCl_4 \cdot 5H_2O$[116,117]) were first dissolved in polar solvents such as alcohol and deionized water, which were then deposited on an ITO or a FTO substrate by spin-coating and gradually converted into SnO_2 through thermal annealing in ambient air. It should be noticed that the humidity and temperature of the environment significantly influence the annealing process and the quality of the obtained SnO_2 films.

Zhang and co-workers prepared SnO_2 thin films using $SnCl_4$ as the tin source at low temperatures.[112] Furthermore, they compared the passivation by $SnCl_4$ at FTO/ETL with that at the ETL/perovskite interface to study the effect of the $SnCl_4$ pre-treatment and post-treatment on SnO_2 (Fig. 4a). With the assistance of $SnCl_4$ pre-treatment, the devices based on Cl–SnO_2

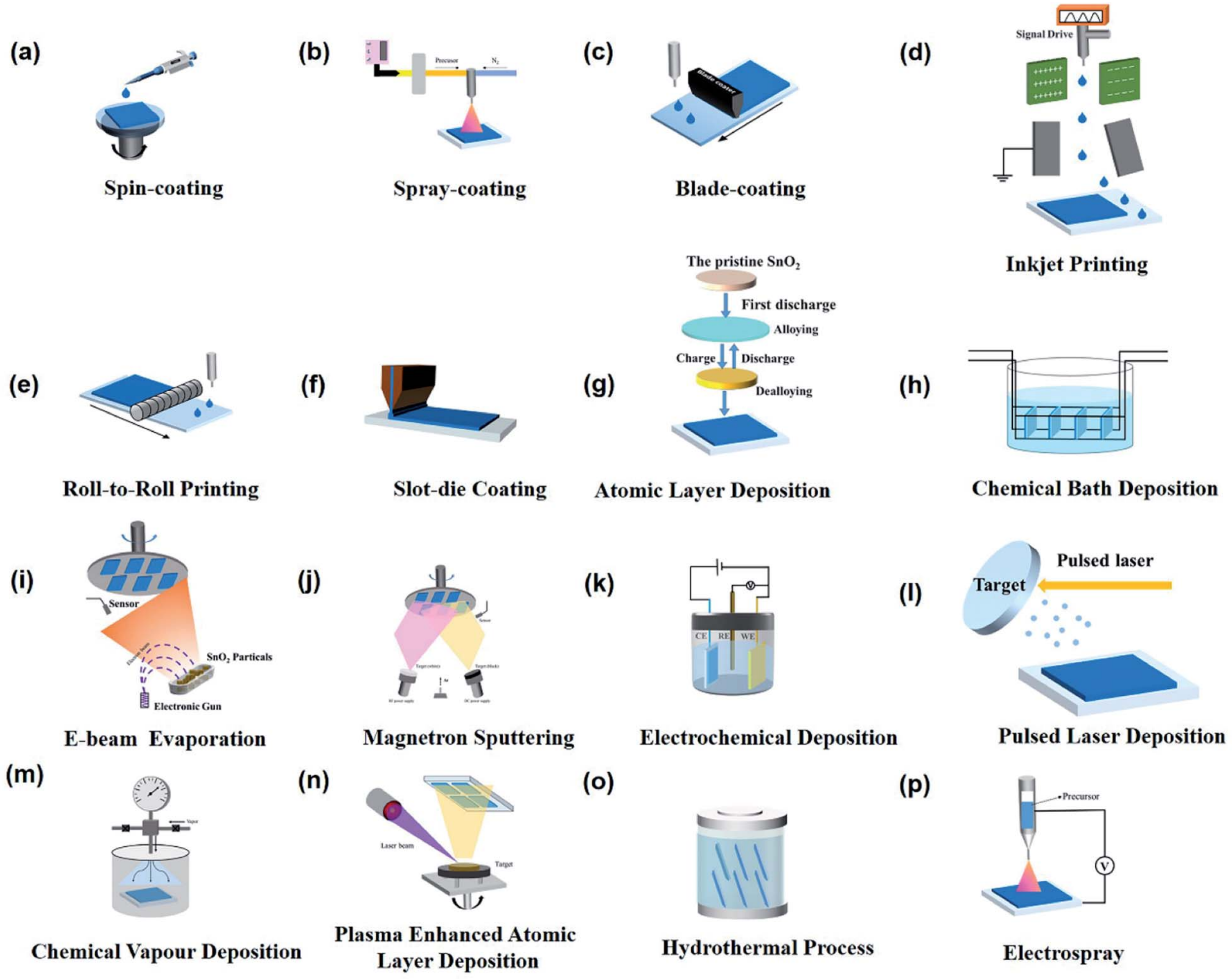

Fig. 3 Schematic illustration of common SnO_2 deposition processes in PSCs. (a) Spin-coating. (b) Spray-coating. (c) Blade-coating. (d) Inkjet-printing. (e) Roll-to-roll printing. (f) Slot-die coating. (g) Atomic layer deposition. (h) Chemical bath deposition. (i) E-beam evaporation electrospray. (j) Magnetron sputtering. (k) Electrochemical deposition. (l) Pulsed laser deposition. (m) Chemical vapor deposition. (n) Plasma enhanced atomic layer deposition. (o) Hydrothermal process. (p) Electrospray.

ETL obtained the best efficiency of 18.6% as compared to the post-treatment process (17.3%). The results confirmed that both modifications could boost the photovoltaic performance of the PSCs. However, $SnCl_4$ pre-treatment increased SnO_2 ETL in electron coupling with FTO, leading to higher electron mobility and better charge extraction efficiency.[112]

Annemarie Pucci and co-workers prepared SnO_2 thin films using $SnCl_2 \cdot 2H_2O$ as the tin source. Their work elucidated the influence of two different solvents and various annealing temperatures on the layer morphology of SnO_2 thin films. It was found that different morphologies were mainly observed during the spin-coating process and not the subsequent annealing process. Furthermore, high annealing temperatures (≈ 400 °C) do not entirely omit the differences in morphology, which were processed from the two kinds of solution systems. Although this device still showed severe hysteresis, the device with inkjet-printed SnO_2 layers presented the highest output efficiency of about 19%.[107]

2.1.2 Sol–gel method. Sol–gel is one of the most commonly used methods to produce thin dense films and powder catalysts at large homogeneous concentrations and under stoichiometry control because of the simplicity, low energy, reliability, reproducibility, and relatively mild fabrication conditions.[118–121]

Lee and co-workers introduced a simple sol–gel method to form a SnO_2 bilayer (Bi–SnO_2) as ETL with dopant-free and amorphous–crystalline heterophase propertie by a sequential spin-coating process. Bi–SnO_2 demonstrated a smooth morphology, low density of energy level traps, and appropriate bandgap matching. As a consequence, Bi–SnO_2 PSCs with active areas (≈ 3.55 cm^2) reached up to about 15% with less hysteresis.[122] Xu *et al.* optimized the aging time, and the PSCs based on the sol–gel SnO_2 film yielded the best PCE of 19% with excellent light trapping ability and a textured SnO_2 structure. But the sol–gel SnO_2 film suffered from poor interfacial contact electrical properties with the perovskite absorber layer because of the annealing effects, resulting in the degradation of performance of PSCs.[123]

Wang *et al.* reported a whole sol–gel crystallized SnO_2 fabrication process below 80 °C (Fig. 4b).[114] Participation of environmental O_2 and H_2O *via* various methods of refluxing is

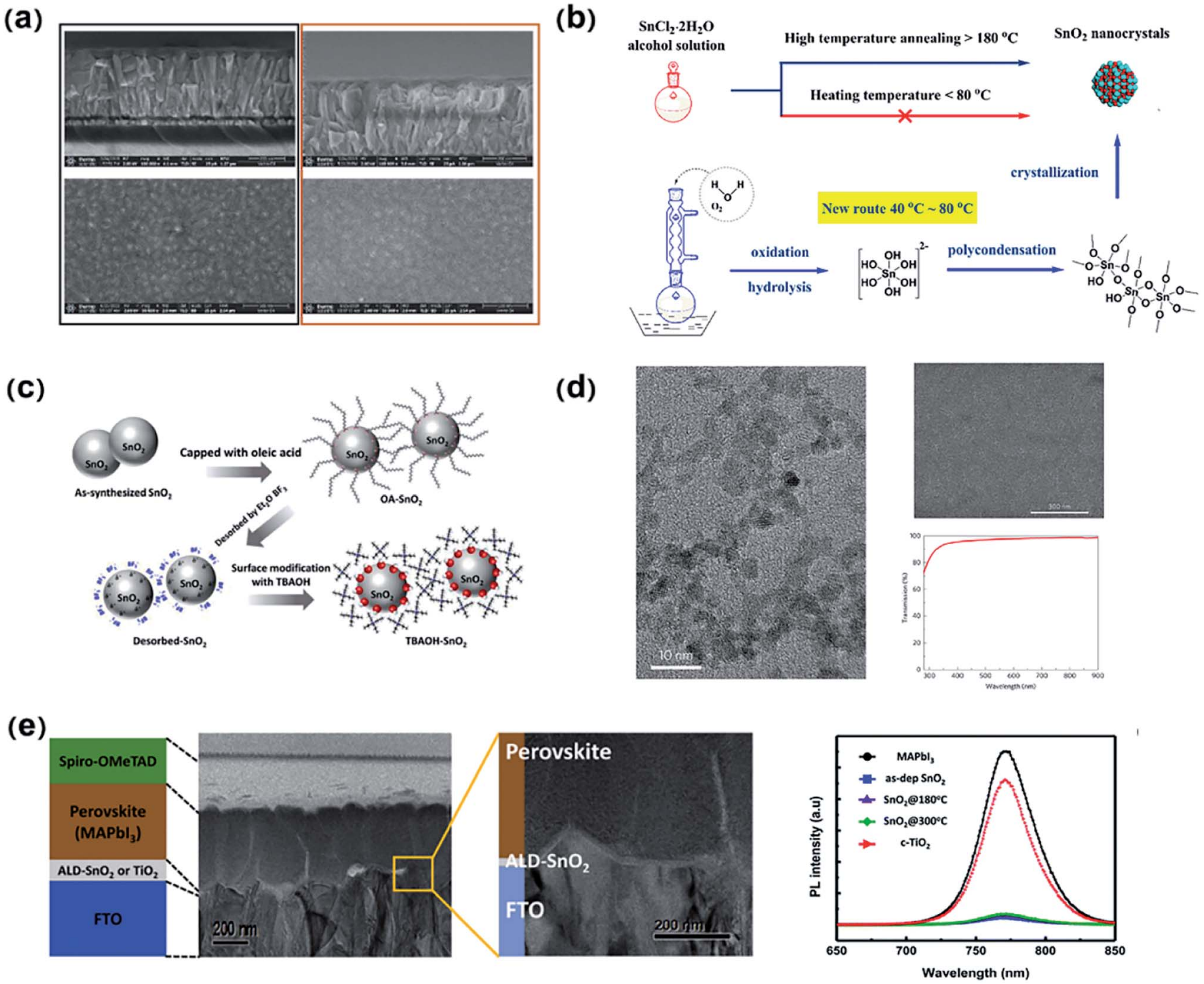

Fig. 4 (a) Cross-sectional and top-view SEM images (left) of the FTO/SnO_2 NC substrate and (right) FTO/Cl–SnO_2. Reproduced with permission.[112] Copyright 2020, Elsevier. (b) Schematic diagram of the wet chemical route to synthesize SnO_2 nanocrystals. Reproduced with permission.[114] Copyright 2017, Elsevier. (c) Schematic illustration of the ligand exchange procedure for TBAOH-capped SnO_2 nanoparticles. Reproduced with permission.[124] Copyright 2017, ACS Publishing Group. (d) TEM and SEM images of SnO_2 nanoparticles and the transmission spectrum of SnO_2 films. Reproduced with permission.[44] Copyright 2017, Nature Publishing Group. (e) Device architecture and cross-sectional TEM images, and PL spectra of the device based on the ALD–SnO_2 films. Reproduced with permission.[125] Copyright 2019, Royal Society of Chemistry.

essential as it could substantially lower the Sn^{2+} oxidation and lead to the hydrolysis of $SnCl_2 \cdot 2H_2O$ alcohol solution, alternatively establishing an energetically favorable pathway for SnO_2 crystallization at low temperatures. The devices had a PCE and a steady-state PCE of 19.20% and 18.48%, respectively, which are significantly better than those of the devices based on high temperature annealed TiO_2 ETLs (16.61% and 15.03%).

2.1.3 SnO_2 nanoparticle synthesis method. It is an efficient method to prepare a compact SnO_2 film by depositing synthesized SnO_2 nanoparticles (NPs) for high performance PSCs.[126,127] To reduce the recombination centers in the SnO_2 film, SnO_2 NPs should be washed prior to the removal of residuals after synthesizing SnO_2. The main issues for the utilization of SnO_2 NPs are the dispersibility and the choice of solvent. A suitable solvent should be able to disperse NPs nicely and should not damage the perovskite layer.

Lee and co-workers selected tetrabutylammonium hydroxide (TBAOH) to successfully disperse SnO_2 NPs (TBAOH–SnO_2) well in ethanol *via* the ligand exchange method (Fig. 4c).[124] Using this TBAOH–SnO_2 NPs as ETL, the PSCs effectively reached up to 18.77% because of minor charge accumulation and good energy level alignment. Besides, the device with a TBAOH–SnO_2 NPs layer only reduced approximately 10% in PCE, which showed improved thermal stability by TBAOH treatment.[124] For SnO_2 deposition, the crystallinity and morphology of the SnO_2 films significantly relied on the annealing temperature.

Park and co-workers investigated the SnO_2 formation at different annealing temperatures (RT, 80 °C, 120 °C, 160 °C, and

200 °C). It was found that when SnO_2 was annealed at 120 °C, the champion PCE was obtained (19.0%). Using AFM and UPS, both the smooth surface and suitable band alignment of SnO_2 film deposition at low temperatures have been observed, contributing to obtaining a high PCE and long stability of the device.[73] However, traditional deposition of the SnO_2 film imposes restrictions on the substrate choice and commercial applications because of a relatively high temperature and/or a long-duration sintering step. Many scientists came up with other creative post-annealing processes to deal with this problem, including microwave-assisted annealing,[126] intense pulsed photonic annealing,[128] and UV-sintering methods.[129,130]

2.1.4 SnO_2 colloidal precursor. You *et al.* formed a compact and uniform SnO_2 film by using a commercialized SnO_2 colloidal precursor (Fig. 4d).[44] The process was that the SnO_2 colloidal nanoparticle precursor was spin-coated at the medium speed rate on top of the ITO electrode. These substrates were annealed at 150 °C for 30 min to evaporate water. The device with SnO_2 film deposition at low temperatures initially achieved 19.9% certificated efficiency. Later on, introducing a surface passivation layer of PbI_2 and an organic halide salt phenethylammonium iodide (PEAI) boosted the certificated efficiency to 20.9% [131] and 23.32%.[35] Tan and co-worker added KCl to the SnO_2 colloidal precursor to passivate the ETL/perovskite interface and at the grain boundaries by K/Cl ions (SnO_2–KCl).[132] The strategy can enhance the V_{oc} from 1.077 to 1.137 V, and a corresponding PCE increased from 20.2% to 22.2% for the devices using SnO_2–KCl composite ETL.

2.2 Atomic layer deposition (ALD)

ALD is considered a promising deposition technique to fabricate ultra-thin and dense metal oxide layers with increased light transmittance based on a self-limiting surface reaction. Due to the precise control at the atomic level, the high-quality film of metal oxides has the merits of promoting charge transfer, suppressing the degradation caused by the external environment and internal ionic migration, and enhancing the photoelectric properties of the device.[133,134]

Lee and co-workers prepared planar SnO_2-based PSCs using ALD by modulating the deposition and post-annealing temperatures. It was found that the post-annealing process can effectively passivate the perovskite and SnO_2 interface, leading to reduced charge recombination. As a result, SnO_2 based PSC with post-annealing achieved a PCE of 20% with high reproducibility and stability.[135] Grätzel and co-workers prepared an amorphous SnO_2 film by ALD, which can maintain its dense morphological characteristics even during the annealing process at 450 °C.[87]

Jeong and co-workers deposited thin SnO_2 films by ALD with subsequent annealing at 180 °C as ETLs. In the cross-sectional image by transmission electron microscopy (TEM), the thicknesses of the SnO_2 film were around 12 nm, similar to those of TiO_2 (Fig. 4e). Compared with the c-TiO_2/$MAPbI_3$ sample, SnO_2@180 °C/$MAPbI_3$ showed a much decrease in PL intensity ($\approx$94%), which exhibited an increase in photo-generated electron extraction from perovskite. Finally, PSCs based on SnO_2 with annealing at 180 °C showed the highest PCE (>18%) with better reproducibility.[125] Although ALD has these attractive advantages, it is necessary to deposit thin films under vacuum conditions and a matched operating space for scalable fabrication, resulting in high preparation costs.

2.3 Chemical bath deposition (CBD)

CBD is seen as a valuable technique to deposit a thin film of metal oxides as a buffer layer in photovoltaic cells, which has many advantages such as low fabrication cost, low-temperature process, suitability for different electrodes, and great reproducibility.[136–138]

Jun Hong Noh and co-workers prepared SnO_2 by CBD as ETL and employed poly(3-hexylthiophene) (P3HT) with gallium(III) acetylacetonate ($Ga(acac)_3$) additives. Consequently, they boosted the performance of free-doping PCE over 24% with a V_{oc} of 1.15 V and a FF of 83.8%. It also showed superior water-resistant property for 2000 h under 85% RH without any encapsulation.[139] Ko and co-workers fabricated a self-controlled SnO_2 through a convenient CBD.[140] It was found that the common-ion and precursor concentrations can effectively tune the growth of the SnO_2 film on FTO, leading to a uniform and compact SnO_2 layer. Finally, the device with a hydrolyzed SnO_2 layer presented an excellent PCE of 20.21%.

Yoo and co-workers first prepared SnO_2 as the ETL using CBD by controlling the formation of Sn intermediate species, which depended on the decomposition pathway of the Sn^{2+} precursor ($SnCl_2$), including four stages. Their SEM images of the SnO_2 layer showed that as the reaction time increases, the pH of the reaction solution increased, and the size of the SnO_2 domain increased from around 50 nm to about 100 nm. Especially, a SnO_2 layer formed a complete coverage on FTO at stage A-ii (pH 1.5), which can be observed from TEM images. The XRD confirmed the presence of various Sn intermediate species, which relied on the pH of the reaction solution (Fig. 5). Moreover, they added the $MAPbBr_3$ + MACl additive in perovskite to stabilize the intermediate phase, enhance the perovskite orientation, and introduce alkylammonium bromide for the 2D perovskite passivation. Due to the holistic method, they obtained a certified PCE of 25.2% (Table 1).[36] Despite the merits of simple operation and low cost, the quality of films in CBD is strongly determined by the processing parameters, including the temperature, concentration, and pH. In the meantime, the pollution of residual precursors after fabrication and the necessity for frequent bath replacement are also critical issues for the commercialization of PSCs.

2.4 E-beam evaporation

E-beam evaporation is one of the high vacuum techniques, which generates more compact films and minimal waste of resources in contrast to the spin-coating process and ALD, and is beneficial to the large-scale application and commercialization of PSCs.[141]

Ma and co-worker fabricated SnO_2 as ETL by e-beam evaporation for possible commercialization of PSCs with large-scale manufacture. As the SnO_2 target source evaporated, the e-beam

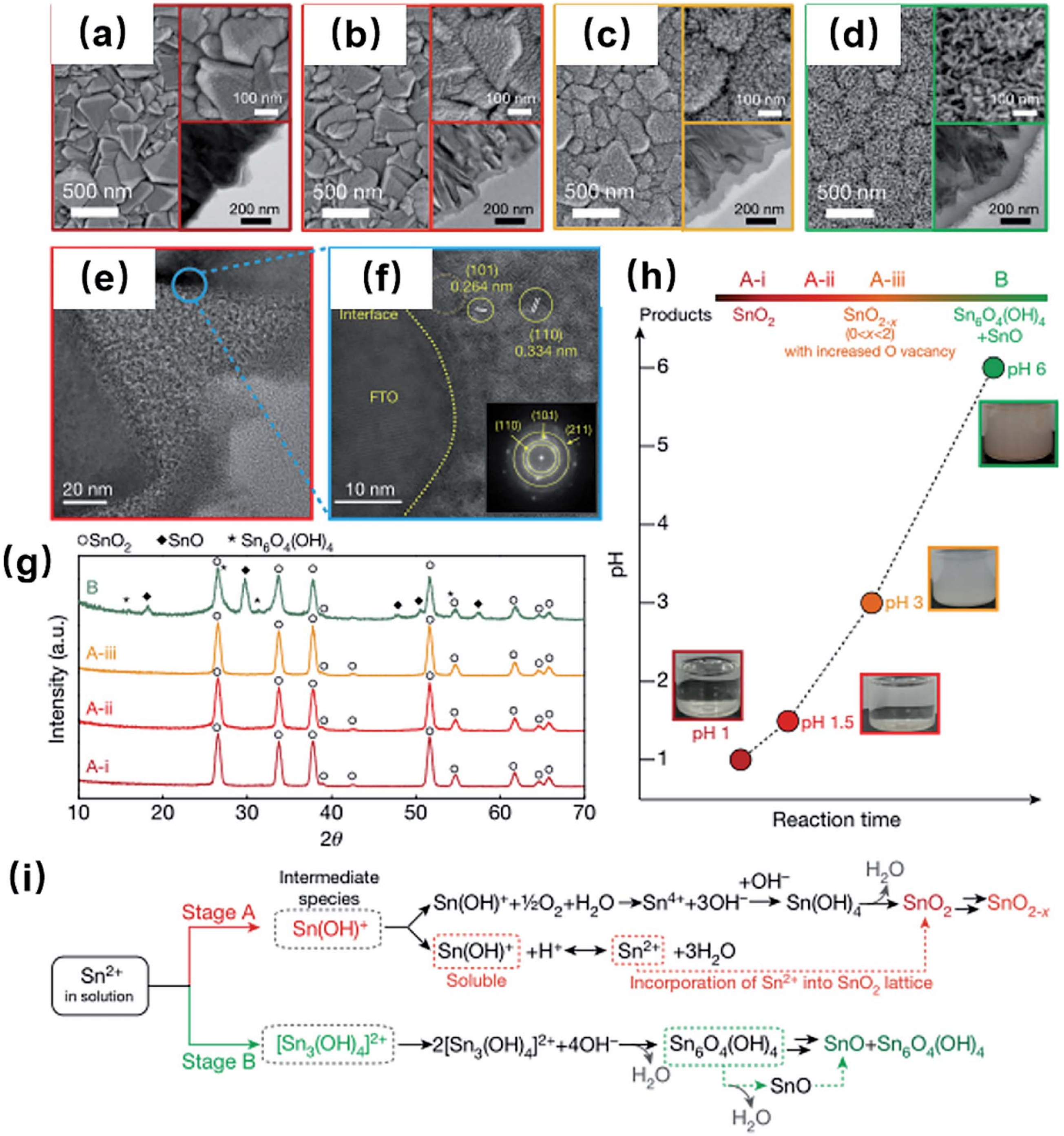

Fig. 5 (a–d) SEM images of SnO$_2$ at different stages: (a) A-i; (b) A-ii; (c) A-iii; and (d) B. The insets shown are SEM (top-right) and the corresponding cross-sectional TEMs (bottom-right). (e) and (f) High-resolution TEM images of SnO$_2$ at stage A-ii (the inset: a fast Fourier transform pattern of the TEM image). (g) XRD patterns of the SnO$_2$ films at different reaction stages. (h) Schematic illustration of the reaction progress with a photograph of the reaction solution at each stage. (i) Schematic illustration of the overall reaction mechanism for forming the SnO$_2$-based films. Reproduced with permission.[36] Copyright 2021, Nature Publishing Group.

evaporation process could simulate thousands of SnO$_2$ film substrates at one time by changing the position of the substrate holder. The advantages of e-beam evaporation were that the thickness and the crystallinity of the SnO$_2$ film could be controlled precisely. Consequently, the PSCs with a uniform SnO$_2$ film by e-beam evaporation demonstrated excellent performance of 18.2% and remarkable waterproof, which retained 97% of its original efficiency value with a relative humidity of 85% for over 34 days.[142] Despite the relatively high deposition rates, e-beam evaporation has the disadvantage of controlling the film composition precisely.

Later, to reduce the resistivity of SnO$_2$, Song and co-workers prepared SnO$_2$ ETL by e-beam evaporation combined with Zn

Table 1 Representative PSCs based on SnO_2 ETL fabricated by different preparation methods[a]

Device structure	Perovskite	Deposition method	Tin source	J_{sc} (mA cm^{-2})	V_{oc} (V)	FF (%)	PCE (%)	Ref.
ITO/SnO_2/PCBM:Bphen/perovskite/HTL(a)/Au	$Cs_{0.04}FA_{0.92}MA_{0.04}PbI_3$	Spin-coating	SnO_2 colloidal precursor	25.15	1.167	78.64	20.39	122
ITO/SnO_2/perovskite/HTL(a)/Au	$MAPbI_3$	Spin-coating	$SnCl_4$	23.2	1.12	71.4	18.6	112
FTO/SnO_2/perovskite/HTL(a)/Au	$MAPbI_3$	Spin-coating	$SnCl_2 \cdot 2H_2O$	22.88	1.06	82.54	18.89	123
ITO/SnO_2/perovskite/HTL(a)/Au	$Cs_{0.05}FA_{0.79}MA_{0.16}PbI_{2.45}Br_{0.55}$	Spray-coating	SnO_2 colloid dispersion	22.2	1.17	76.1	19.8	100
FTO/SnO_2:GQDs/perovskite/HTL(a)/Au	$(FAPbI_3)_{0.85}(MAPbBr_3)_{0.15}$	Spray-coating	$SnCl_2 \cdot 2H_2O$	22.5	1.12	65.8	17.08	99
FTO/SnO_2/perovskite/HTL(a)/Au	$MAPbI_3$	Spray-coating	SnO_2 colloid dispersion	21.63	1.002	78	16.91	101
ITO/SnO_2/perovskite/HTL(a)/Au	$Cs_{0.05}(FA_{0.85}MA_{0.15})_{0.95}Pb(I_{0.85}Br_{0.15})_3$	Slot-die-coating	SnO_2 colloid dispersion	22.60	1.148	79	20.50	103
PEN/ITO/SnO_2/perovskite/HTL(a)/Ag	$FA_xMA_yCs_{1-x-y}Pb(I_zBr_{1-z})_3$	Roll-to-roll	SnO_2 colloid dispersion	19.96	1.07	70.09	16.60	104
ITO/SnO_2/perovskite/HTL(a)/Ag	$Cs/FA_xMA_{1-x}PbI_yBr_{3-y}$	Blade-coating	SnO_2 colloid dispersion	23.1	1.08	72	18	106
FTO/SnO_2/perovskite/HTL(a)/Au	$CsPbI_3$	Blade-coating	SnO_2 colloid dispersion	20.67	1.12	81.98	19	105
ITO/SnO_2/perovskite/HTL(a)/Au	$Cs_{0.10}FA_{0.75}MA_{0.15}Pb(Br_{0.15}I_{0.85})_3$	Inkjet-printing	$SnCl_2 \cdot 2H_2O$	23.6	1.11	72	18.8	107
FTO/SnO_2/perovskite/HTL(a)/Au	$MAPbI_3$	ALD	$C_8H_{24}N_4Sn$	22.6	1.07	75.6	18.3	125
FTO/SnO_2/TiO_2/perovskite/HTL(a)/Au	$(FAPbI_3)_{0.85}(MAPbBr_3)_{0.15}$	ALD	$C_8H_{24}N_4Sn$	22.67	1.13	78	20.03	135
FTO/SnO_2/perovskite/HTL(a)/Au	$FAPbI_3$	CBD	$SnCl_2 \cdot 2H_2O$	25.09	1.194	84.7	25.4	36
FTO/SnO_2/perovskite/HTL(b)/Au	$(FAPbI_3)_{0.95}(MAPbBr_3)_{0.05}$	CBD	$SnCl_2 \cdot 2H_2O$	25.5	1.15	83.8	24.6	139
FTO/SnO_2/perovskite/HTL(a)/Au	$Cs_{0.05}(MA_{0.17}FA_{0.83})_{95}Pb(I_{0.83}Br_{0.17})_3$	E-beam evaporation	SnO_2 powders	22.47	1.08	71	17.38	142
FTO/Zn–SnO_2/perovskite/HTL(a)/Au	$FA_xMA_yCs_{1-x-y}Pb(I_z,Br_{1-z})_3$	E-beam evaporation	SnO_2 powders	22.72	1.11	75	18.95	143
FTO/SnO_2/perovskite/HTL(a)/Au	$Cs_{0.06}MA_{0.27}FA_{0.67}PbI_{2.7}Br_{0.3}$	Magnetron sputtering	SnO_2 target	23.7	1.08	79	20.2	148
FTO/SnO_2/perovskite/HTL(a)/Au	$FA_{0.85}MA_{0.15}Pb(I_{0.85}Br_{0.15})_3$	Magnetron sputtering	SnO_2 target	22.58	1.065	75.6	18.2	149
FTO/SnO_2/PCBM/perovskite/HTL(a)/Au	$MAPbI_3$	PLD	SnO_2 target	21.51	1.11	73	17.29	164
FTO/SnO_2/C_{60}-SAM/perovskite/HTL(a)/Au	$MA_{0.7}FA_{0.3}PbI_3$	PEALD	SnO_2 target	22.71	1.113	80.75	20.41	156
ITO/SnO_2/PCBM/perovskite/HTL(a)/Ag	$MAPbI_3$	Electrodeposition	$SnCl_2$	19.75	1.08	65	13.88	150
FTO/SnO_2/perovskite/HTL(a)/Au	$Cs_{0.05}(MA_{0.17}FA_{0.83})_{0.95}Pb(I_{0.83}Br_{0.17})_3$	Combustion	$SnCl_2 \cdot 2H_2O$	23.85	1.122	78.2	20.92	165
FTO/SnO_2/PCBM/perovskite/HTL(a)/Ag	$MAPbI_3$	CVD	$SnCl_2$	14.7	1.03	67.51	10.2	159
FTO/SnO_2/C60/perovskite/HTL(a)/Au	$MAPbI_3$	Electrospray	$SnCl_2 \cdot 2H_2O$	23.7	1.103	77.3	20.2	163
FTO/SnO_2/perovskite/HTL(a)/Au	$Cs_{0.05}(MA_{0.17}FA_{0.83})_{0.95}Pb(I_{0.83}Br_{0.17})_3$	Hydrothermal	$SnCl_4 \cdot 5H_2O$	22.69	1.129	72.70	18.62	117
FTO/SnO_2/perovskite/HTL(a)/Au	$MAPbI_3$	Thermal evaporation	SnO_2 powder	23.36	1.04	69.2	16.79	161
P-FTO/perovskite/HTL(a)/Au	$MAPbI_3$	*In situ* plasma etching of FTO	Commercial FTO substrate	23.85	1.11	77.12	20.39	160
FTO/G-SnO_2/C–SnO_2/perovskite/HTL(a)/Au	$Cs_{0.05}(MA_{0.17}FA_{0.83})_{0.95}Pb(I_{0.83}Br_{0.17})_3$	Ball-milling	SnO_2 powder	21.16	1.22	80.09	21.09	158

[a] HTL(a): spiro-OMeTAD; HTL(b): poly(3-hexylthiophene) (P3HT); $C_8H_{24}N_4Sn$: tetrakis(dimethylamido)tin(IV); GQDs: graphene quantum dots; CBD: chemical bath deposition; PLD: pulse laser deposition; ALD: atomic layer deposition; CVD: chemical vapor deposition; PEALD: plasma-enhanced atomic-layer deposition.

doping (Zn–SnO_2). Following Zn doping, the Zn–SnO_2 layer improved the charge mobility, inhibited the charge accumulation at the interface, and optimized the SnO_2 energy level structure, resulting in a PCE increase from 18.95% to 20.16% with long-term stability. More importantly, after 100 bending tests, the flexible device maintained a PCE of over 15% (Fig. 6a and b).[143] Furthermore, Li and co-workers used an oxygen plasma-triggered e-beam evaporation approach to create SnO_2 films at ambient temperature without annealing. The oxygen plasma can precisely tune the stoichiometry of SnO_2 films in the evaporation process due to its intense oxidation activity, thereby endowing SnO_2 with uniformity, high transmittance, high Hall mobility, and good hydrophilicity.[144] Aside from the requirement

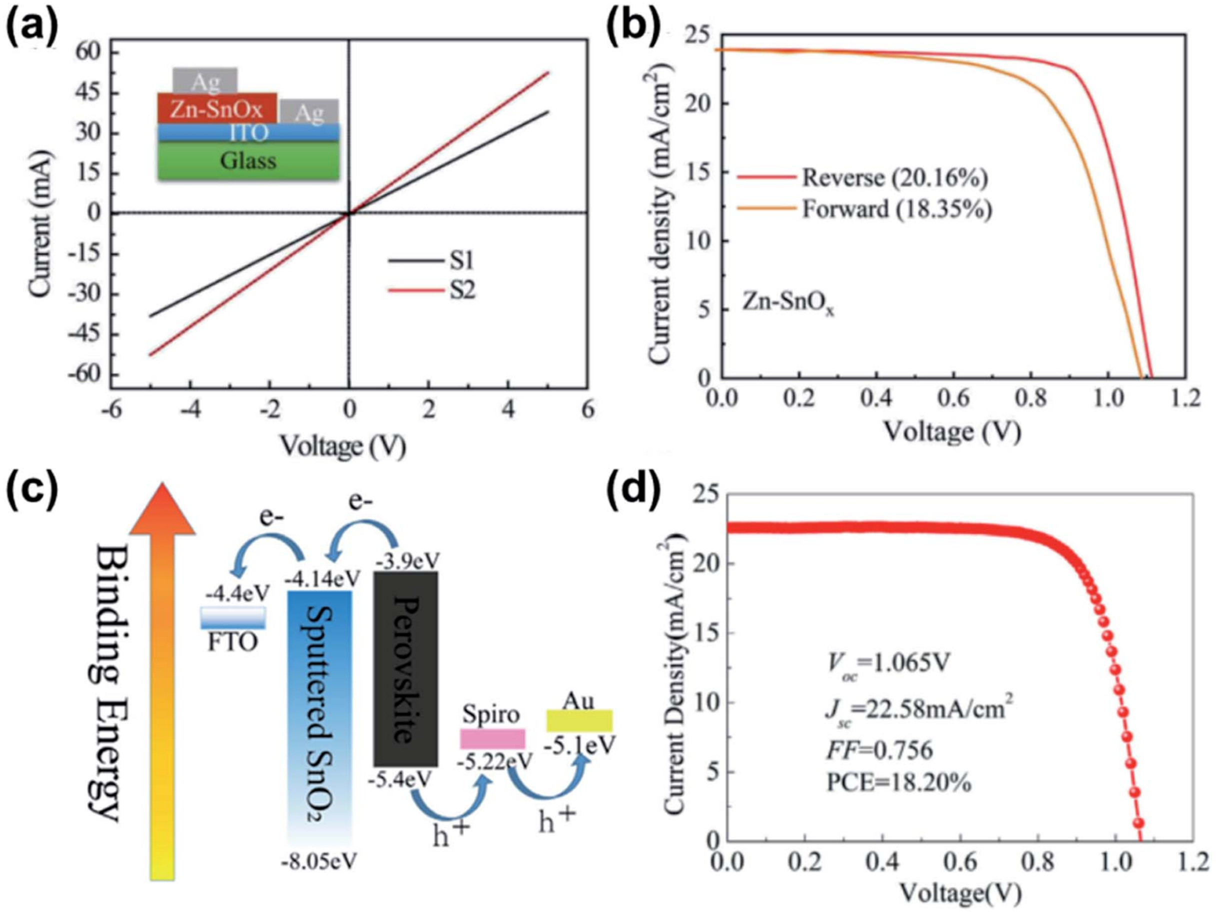

Fig. 6 (a) Conductivity of bare SnO_x (S1) and Zn–SnO_x (S2); (b) the reverse scan J–V curves of the device based on Zn–SiO_x. Reproduced with permission.[143] Copyright 2020, Wiley-VCH. (c) Energy level scheme for various layers in a sputtered SnO_2 based device. (d) J–V curves under the reverse voltage scan of the best device with sputtered SnO_2. Reproduced with permission.[149] Copyright 2019, Elsevier.

for a high vacuum, this approach is limited by X-ray damage on substrates and slow conduction speeds.

2.5 Magnetron sputtering

Magnetron sputtering is a mature and reliable deposition method with the use of low-cost metal-oxide targets to prepare metal-oxide thin films in the lab- and industrial-scale.[145,146] SnO_2 particles are sputtered by high energy argon ions, react with the reaction gas (like high purity oxygen), and then deposited on the top of the FTO, which is a continuous process. Magnetron sputtering has excellent merits, including the precise control of film density and thickness, low waste of raw materials, a mild deposition process, and low production cost. Besides, the deposition process is usually operated in a high vacuum chamber, leading to high repeatability with minor damage to the natural environment.[147]

Qiu and co-workers systematically investigated the chemical and physical characteristics of sputtered SnO_2. It played a significant role in the formation of high quality to control the oxidizing process. Through improvement in the device architecture, the device with sputtered SnO_2 ETL exhibited the champion PCE of 20.2% and a useful life of 625 h under T_{80} measurement, confirming the enhanced conductivity of SnO_2.[148] Meanwhile, Bai and co-workers discovered that while changing the working gas ratio of Ar/O_2 can result in identical shape and crystallinity of sputtered SnO_2, it can also result in different trap states and carrier transit dynamics in PSC devices. The devices based on sputtered SnO_2 ETL demonstrated a champion PCE (up to 18.20%) (Fig. 6c and d).[149] Additionally, Otoufi and co-workers introduced sputtered SnO_2 on the TiO_2 layer to form TiO_2/SnO_2 bilayers to improve electron extraction further and achieve a better PCE of 12.3% in comparison with only TiO_2 as ETL (8.18%).[146] The gas flows played a crucial role in controlling the oxygen vacancies. On the other hand, tail states within the bandgap are caused by the amorphous or nanocrystallinity in the films, which are effectively suppressed by interface passivation.

2.6 Other deposition methods

Besides the solution-processable and vacuum evaporation methods, other creative methods are emerging for high-quality SnO_2 films due to demands for different applications. For example, Chen *et al.* prepared PSCs with SnO_2-ETLs by electrochemical deposition. The PSCs using $MAPbI_3$ as the light-absorbing layer obtained a PCE of 13.88% with negligible hysteresis.[150] The electrochemical deposition was beneficial for SnO_2 preparation at low temperatures (50 °C) without introducing a seed layer or a post-treatment process.[151] The dual-fuel combustion method was usually an excellent choice to control the SnO_2 growth.[152,153] Compared to the conventional solution-process method, as combustion synthesis was ignited, the method not only requires significant external energy input but also is exothermic, leading to reduced production cost.

Additionally, other physical and chemical preparation technologies were also used to deposit SnO_2 ETLs, including plasma-enhanced atomic layer deposition (PEALD),[154–157] high energy ball-milling,[158] chemical vapor deposition (CVD),[159] *in situ* plasma etching of FTO,[160] thermal evaporation,[161] hydrothermal processes,[117,162] and electrospray method.[163] In these methods, the SnO_2 film crystallized well during the deposition process on the substrates without further post-heating treatment. Thus, these methods demonstrate significant advantages for the mass production of flexible PSCs, even though the process tends to take much time.

3. Nanostructures of SnO_2

3D SnO_2 materials such as SnO_2 nanoparticles or nanocrystals are commonly exploited as ETL.[83] However, Zhao *et al.* found that 0D–2D SnO_2 ETLs can reduce light scattering from rough FTO and enlarge the perovskite grain size, leading to improved performance.[166] Nanostructured SnO_2 is a critical factor for high-efficiency PSCs to scale up planar PSCs for industrial applications. On the one hand, it can optimize the surface wettability for smooth perovskite coverage on the substrate. On the other hand, nanostructured SnO_2 (Fig. 7) enhances the interfacial contact to eliminate the notorious electronic trap states, which removes the energy level traps at the interface. So, the dimensional control of SnO_2 is a promising strategy to prepare SnO_2 ETL with a high photoelectrical property.

3.1 SnO_2 nanowires

SnO_2 nanowires (NWs), a one-dimensional (1D) semiconductor material, are a good ETL in the field of PSCs due to their

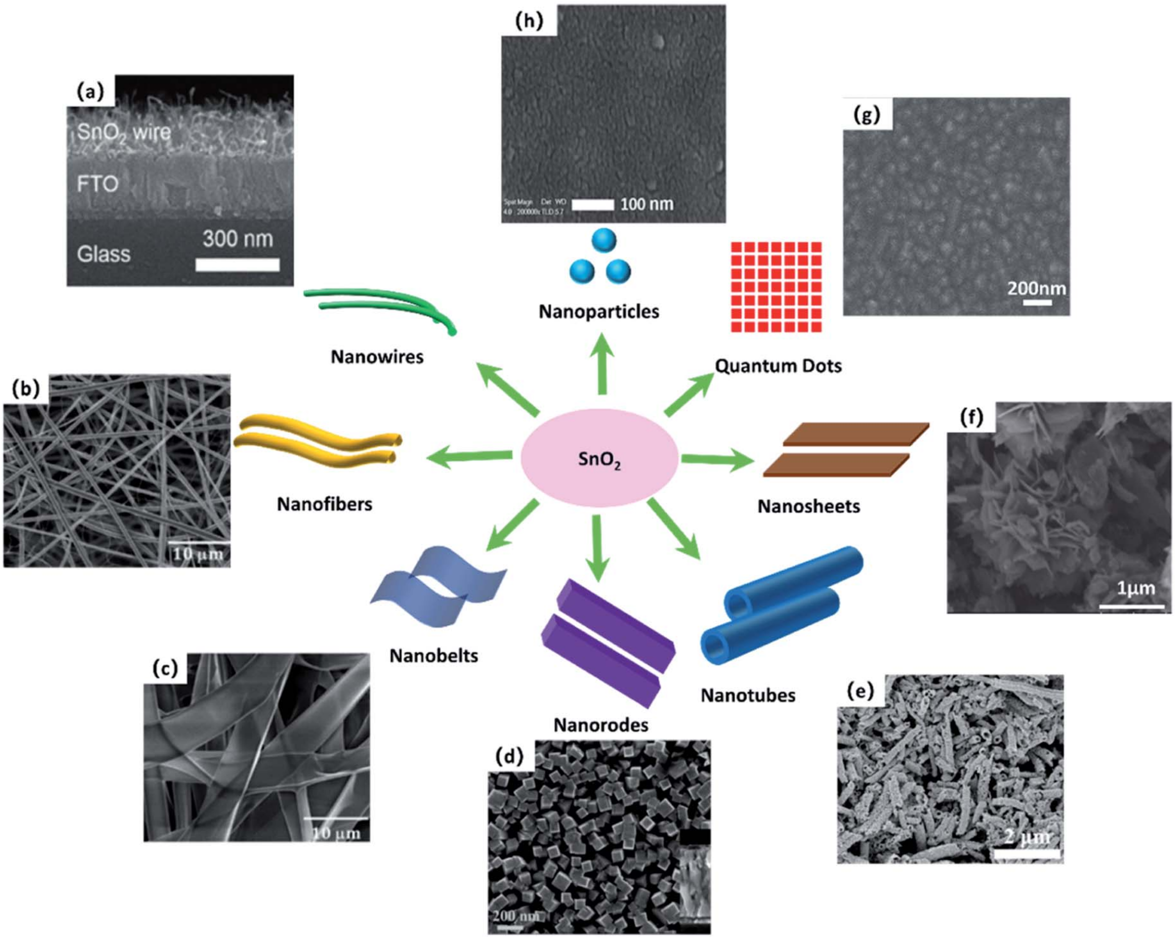

Fig. 7 Schematic diagram of various nanostructures of SnO_2 in accordance with SEM images of various SnO_2 nanostructures: (a) nanowires reproduced with permission.[167] Copyright 2015, Royal Society of Chemistry. (b) Nanofibers and (c) nanobelts. Reproduced with permission.[168] Copyright 2018, Royal Society of Chemistry. (d) Nanorods. Reproduced with permission.[169] Copyright 2018, Wiley-VCH. (e) Nanotubes. Reproduced with permission.[170] Copyright 2020, Elsevier. (f) Nanosheets. Reproduced with permission.[171] Copyright 2016, Elsevier. (g) Quantum dots. Reproduced with permission.[93] Copyright 2018, Wiley-VCH; (h) nanoparticles. Reproduced with permission,[83] Copyright 2015, ACS Publishing Group.

efficient extraction and collection capacity. Besides, 1D nanomaterials have fewer defects like grain boundaries which significantly decrease in dead-ends.[172–176]

Han and co-workers synthesized 1D SnO_2 as the ETL by a vapor–liquid–solid (VLS) reaction for realizing high conductivity for SnO_2 (Fig. 7a). The SnO_2 NWs showed a high transmittance of about 80%, similar to that of the bare FTO substrate, as observed from the UV-vis transmittance spectrum. SnO_2 NWs were modified with TiO_2 nanoshells as TiO_2/SnO_2 NW ETL *via* plasma-enhanced atomic layer deposition (PEALD). Consequently, the TiO_2/SnO_2 NW ETL device displayed over 95% absorbed photon-to-current conversion efficiency (APCE) at 750 nm with a PCE of 14.2% and decreased the electron transport time by one order of magnitude in comparison with that of mp-ETL-based devices.[167]

3.2 SnO_2 nanofibers and nanobelts

1D SnO_2 nanofibers (NFs) and nanobelts (NBs) demonstrate fast electron transport rate and light scattering ability used in the dye-sensitized solar cells (DSSCs).[177–179] Mali and co-workers prepared SnO_2 NFs and NBs with a smooth and uniform morphology as ETL *via* the electrospinning technique.[168] The pure tetragonal rutile phase in SnO_2 NFs and NBs was presented by structural analysis. SEM micrographs exhibited that both the lengths of SnO_2 NFs and NBs reached up to 500 μm with a diameter of about 450–500 nm and a thickness of 180–200 nm, respectively (Fig. 7b and c). Their optimized devices yielded a PCE of >16% based on SnO_2 NBs with good shelf-life stability.[168]

3.3 SnO_2 nanorods

Due to a particular open porous structure, SnO_2 nanorods (NRs) provide more expansive space to effectively fill the pores with the perovskite crystals[180–183] and enhance the light-induced photo utilization of the perovskite layer with good light scattering ability.[184]

Xu and co-workers reported good crystalline SnO_2 NRs as the ETL with a high aspect ratio through the sophisticated solvothermal approach to promote PSCs' stability and photovoltaic performance. They showed that oleic acid (OA) ligands could precisely control the length and the diameter of SnO_2 NRs without complex treatments. Besides, the insulating OA ligands had a weaker impact on the electron mobility of SnO_2 NRs than on TiO_2 NRs. The OA-capped SnO_2 NRs ETL-based PSCs with a planar structure achieved the best efficiency of over 18%, which was much higher than that of PSCs with an OA-capped TiO_2 NR ETL (14.27%).[117] Zhang *et al.* prepared the *in situ* SnO_2 NRs as ETL *via* a convenient hydrothermal method in an acidic solution.[162] The average diameters of SnO_2 NRs increased from 15 to 25 nm by controlling the precursor concentration, and the corresponding area density drops down to several hundreds of μm^{-2}. Later on, to simplify the SnO_2 NR fabrication process and remove the OA ligand, Lv and co-workers reported a facile hydrothermal method to synthesize highly crystalline SnO_2 SRs with good light-harvesting ability (Fig. 7d). In the hydrothermal process, the reaction time and temperature are vital process parameters that determine the morphology of SR, such as the length and the diameter. In addition, a TiO_2 interlayer was inserted between the perovskite absorber layer and the SnO_2 ETL, forming a graded heterojunction configuration, leading to the power output of up to 18.7% with better ambient stability and repeatability.[169]

3.4 SnO_2 nanotubes

SnO_2 nanotubes (NTs) as ETL have higher conductivity and a required conduction band edge (3.6 eV) that can induce superior electrochemical properties than TiO_2 (3.2 eV) (Fig. 7e).[185–188] Gao and co-workers created SnO_2 NTs as ETL *via* an *in situ* template self-etching strategy. The ZnO_2 nanorods as sacrificial templates were covered by smooth nanoporous SnO_2 shells by spin coating. The corresponding EQE spectrum suggested that SnO_2 NTs based PSCs exhibited a high photocurrent of 15.9 mA cm^{-2} with a stable efficiency of 12.1% in more than 1000 s under simulated light illumination.[189]

3.5 SnO_2 nanosheets

The SnO_2 nanosheets (NSs) demonstrate lots of advantages such as improving photo-induced carrier collection, promoting interfacial charge transfer, and processing good weathering performance of PSCs.[163,171,190–192]

Hydrothermal growth is a standard method to synthesize SnO_2 nanosheets. Zhou and co-workers prepared SnO_2 NSs as ETL *via* the hydrothermal method in place of the traditional mesoporous TiO_2 layer in PSCs for the first time (Fig. 7f). The device achieved a maximum efficiency of over 7% by optimizing the perovskite's crystallization time and treating it with $TiCl_4$ aqueous solution.[171] Liu and co-workers deposited a mesoporous layer of SnO_2 NSs on a thin, compact SnO_2 layer by using the low-temperature hydrothermal method to improve the PSC stability. The device with the highest efficiency of 16.17% was obtained through such a facile method and retained 90% of its initial PCE value in ambient after 130 d of storage without encapsulation.[190] To optimize the interfacial contact with the perovskite, doping with yttrium and introduction of a C_{60} interlayer are done in SNs ETL-based devices. Yang and co-workers synthesized a yttrium-doped SnO_2 (Y–SnO_2) as ETL *via* an *in situ* hydrothermal approach at 95 °C. As a result, the Y–SnO_2 based PSC achieved a champion PCE of 17.29% with free hysteresis.

Furthermore, it clearly showed that SnO_2 nanosheet films demonstrated a slightly wider bandgap and a more homogeneous distribution of SnO_2 nanosheet arrays after Y-doping.[192] The introduction of a C_{60} interlayer (Y:SnO_2) between SNs ETL and perovskite was reported by Wu.[191] They found that the C_{60} interlayer can tune the energy level matching, reduce the charge accumulation and thus prolong the electron lifetime and enhance the V_{oc}. The champion PCE obtained was 18.31%, and the device with C_{60}-NSs preserved over 90% of its champion PCE after 500 h of storage at RT in open air.

3.6 SnO_2 quantum dots

Due to the low crystallinity, inferior electron mobility at lower annealing temperatures as well as instability of the SnO_2 film deposited *via* colloidal SnO_2 solution, many researchers synthesized high-crystallinity SnO_2 quantum dots (QDs) as ETL by a facile mild solution method combined with spin coating on FTO to improve the light scattering and electron transport and reduce the charge recombination, leading to a dramatic increase in PCE.[193–197]

Yang and co-workers reported colloidal SnO_2 QDs as ETLs by a facile and repeatable two-step solution-processable method (Fig. 7g). First, they obtained the low concentration of SnO_2 QDs solution by controlling the amount of thiourea in the $SnCl_2\cdot 2H_2O$ water solution, and then spin-coated SnO_2 QDs and changed the annealing temperature to eliminate a mass amount of thiol- and amino-groups, leading to an appropriate energy level matching and changeable carrier dynamics. Finally, the planar PSCs with SnO_2 QDs ETLs achieved a maximum power output of over 20% for the planar PSCs.[93] Vijayaraghavan and co-workers chose SnO_2 QDs as ETL to replace the commonly used mesoporous TiO_2 owing to their excellent electron extraction and hole blocking ability. For low-cost production and superior stability in air for PSCs, they designed the structure of glass/ITO/SnO_2 QDs/perovskite/carbon as HTL-free PSCs and deposited carbon electrodes *via* low-temperature curing to substitute the widely used vacuum-deposition. As a result, the highest power output of 13.64% was obtained.[198] Wang and co-workers used SnO_2 QDs as ETL, which was combined with potassium hexafluorophosphate (KPF6) treatment. KPF6 had the dual-passivation in which organic cation groups were reoriented or redistributed *via* the strong hydrogen bonds between the PF_6^- group and organic cations. Moreover, KPF6 passivated the interfacial traps to suppress the energy level traps to improve the conductivity of SnO_2 through the solid ionic bonds between the PF_6^- group and Sn^{4+}/Sn^{2+}.[199]

4. Passivation strategies of SnO_2 ETLs

Although SnO_2 films have several advantages over other metal oxide films, they also have comparable interface difficulties when used as the ETLs of PSCs. There are many flaws at the interfaces due to the bungle between the metal oxides and perovskite films, which degrade the presentation of PSCs. Therefore, passivations on the SnO_2 film are often used to improve the performance of SnO_2 based perovskite solar cells that include elemental doping, bilayer design, and interface modification. The following are the consequences on passivation: (1) tuning of the energy level that promotes electron transfer at the ETL/perovskite interface; (2) passivation of the interfacial defects and suppress nonradiative recombination; (3) control of the crystallization process and improvement of the crystallinity of the perovskite film; and (4) endowing devices with improved humidity tolerance and long-term stability.

4.1 Elemental doping

Owing to intrinsic defects such as Sn interstitials or O vacancies, there is serious charge recombination and contact resistance at the interface between SnO_2 ETL and perovskite, resulting in a low charge transportation rate.[200–203] To suppress the traps on the SnO_2 film as well as for better energy-level alignment, the researchers demonstrated several halides and metal ions as dopants to improve the conductivity properties of ETL including the halogen ions (Cl^- [204–206] and F^- [207–211]), metal ions (Li^+,[212–215] Mg^{2+},[196,216] Al^{3+},[217,218] Zn^{2+},[143,219] Sb^{3+},[215,220,221] Mo^{2+},[222] Ru^{2+},[209,223] Ga^{3+},[224,225] Zr^{2+},[226,227] Nb^{5+} [228–230] and Ta^{5+} [231]) and rare earth ions (Y^{3+},[192,232] La^{3+} [233]) and Nd^{3+} [165] (Table 2).

Gong and co-workers introduced Cl in SnO_2 nanoparticles (SnO_2–Cl) with a chloroform-D/2-methoxy ethanol solvent (Fig. 8a).[205] The SnO_2–Cl film had a hydrophobic surface as the

Table 2 Representative PSCs based on elemental doped SnO_2 ETL

Doped element	Doping raw material	Device architecture	Perovskite	PCE (%)	Ref.
Cl^-	Chloroform-D/2-methoxy ethanol solvent	FTO/Cl–SnO_2/perovskite/spiro-OMeTAD/Au	$(FAPbI_3)_{0.85}(MAPbBr_3)_{0.15}$	18.1	205
F^-	NH_4F	FTO/F–SnO_2/perovskite/spiro-OMeTAD/Au	$(FAPbI_3)_{0.85}(MAPbBr_3)_{0.15}$	20.2	207
Li^+	Li-TFSI	FTO/SnO_2/Al_2O_3/perovskite/spiro-OMeTAD/carbon	$MAPbI_3$	10.01	214
Mg^{2+}	$MgAc\cdot 4H_2O$	FTO/Mg–SnO_2/perovskite/spiro-OMeTAD/Au	$MAPbI_3$	19.21	196
Al^{3+}	$Al(NO_3)_3$	FTO/Al–SnO_2/perovskite/spiro-OMeTAD/Au	$Cs_{0.05}(MA0_{.17}FA_{0.83})_{0.95}Pb(I_{0.83}Br_{0.17})_3$	17.66	218
Zn^{2+}	$ZnCl_2$	FTO/$ZnSnO_2$/perovskite/CuPc/carbon	$Cs_{0.05}FA_{0.79}MA_{0.16}PbI_{2.5}Br_{0.5}$	17.78	143
Sb^{3+}	$SbCl_3$	ITO/Sb–SnO_2/perovskite/spiro-OMeTAD/Au	$Cs_{0.05}(FA_{0.85}MA_{0.15})_{0.95}Pb(I_{0.85}Br_{0.15})_3$	20.73	221
Mo^{5+}	$MoCl_5$	FTO/Mo–SnO_2/perovskite/spiro-OMeTAD/Au	$MAPbI_3$	10.52	222
Ru^{2+}	$RuCl_3\cdot 5H_2O$	FTO/Ru–SnO_2/perovskite/spiro-OMeTAD/Au	$Cs_{0.05}(MA_{0.10}FA_{0.90})_{0.95}Pb(I_{0.90}Br_{0.10})_3$	22.0	223
Ga^{3+}	$Ga(NO_3)_3\cdot 6H_2O$	ITO/Ga-SnO_2/perovskite/spiro-OMeTAD/Ag	$(FAPbI_3)_{0.97}(MAPbBr_3)_{0.03}$	18.18	224
Zr^{2+}	$ZrCl_2O\cdot 8H_2O$	ITO/Zr–SnO_2/perovskite/spiro-OMeTAD/Au	$(FAPbI_3)_{0.85}(MAPbBr_3)_{0.15}$	19.54	226
Nb^{5+}	$NbCl_5$	FTO/Nb–SnO_2/perovskite/spiro-OMeTAD/Au	$FA_{0.75}MA_{0.2}Cs_{0.05}Pb(I_{0.14}Br_{0.86})_3$	20.5	228
Ta^{5+}	$TaCl_5$	ITO/Ta–SnO_2/perovskite/spiro-OMeTAD/Au	$Cs_{0.05}(MA_{0.10}FA_{0.90})_{0.9}5Pb(I_{0.90}Br_{0.10})_3$	20.8	231
Y^{3+}	$Y(OC_4H_9)_3$	FTO/Y–SnO_2/perovskite/spiro-OMeTAD/Au	$Cs_{0.05}(MA_{0.15}FA_{0.85})_{0.95}Pb(I_{0.85}Br_{0.15})_3$	20.71	232
La^{3+}	$LaCl_3\cdot 5H_2O$	FTO/La–SnO_2/perovskite/spiro-OMeTAD/Au	$MAPbI_3$	17.08	233
Nd^{3+}	$Nd(NO_3)_3\cdot 6H_2O$	FTO/Nd-SnO_2/perovskite/spiro-OMeTAD/Au	$Cs_{0.05}(MA_{0.17}FA_{0.83})_{0.95}Pb(I_{0.83}Br_{0.17})_3$	20.92	165

effect of Cl, which increased the grain size of perovskite crystals (Fig. 9). Furthermore, SnO_2–Cl as an ETL dramatically reduced the electron trap density and inhibited the charge recombination. In contrast to untreated SnO_2 based PSCs, SnO_2–Cl based PSCs achieved a PCE of 18.1%, with significant improvements in J_{sc} and reduced hysteresis. Later, Wang *et al.* reported F-doped SnO_2 ($F{:}SnO_2$) nanocrystals as the ETL by spin-coating $SnCl_2 \cdot 2H_2O$ and NH_4F solution onto fresh FTO substrates in a facile solution-processable method at low temperatures (Fig. 8b).[207] They found that the band offset between the ETL and the perovskite absorber is related to the F doping level in SnO_2 nanocrystals; the band offset was effectively tailored by doping F into the SnO_2 film, which led to an increasing built-in electric field for maximizing the V_{oc} and charge collection simultaneously. Consequently, a champion PCE of 20.2% with a V_{oc} of 1.13 V can be obtained for n-i-p planar PSCs using an F-doped SnO_2 bilayer ETL.

Jung and coworkers reported doped SnO_2 NPs by Zr element, improving the multiple optoelectronic properties of SnO_2 (Fig. 8c). Zr doping reduced the current leakage and suppressed the charge recombination, facilitating the interfacial transfer between the ETL and the perovskite layer. Consequently, they obtained the best PCE of 19.54% with reduced hysteresis. The research demonstrated that the controlled Zr-doping SnO_2 film led to adjusted energy levels, increased electrical conductivities, and decreased surface defect densities for optimal interface properties of PSCs.[226] Some other elements also showed similar positive results.[209,214,223,231]

Fang and co-workers designed a Zr/F co-doped SnO_2 ETL due to its low conduction band position and limited intrinsic carriers; they found that the doping of Zr can increase the CB of SnO_2 for higher V_{oc}, which decreased the energy traps in electron extraction and restrained the interface recombination between the ETL and the perovskite (Fig. 8d). Moreover, as n-type doping, F doping endowed SnO_2 with a mass of free electrons and facilitated the conductivity of the ETL for improvement in short-circuit current (J_{sc}). With the merits of Zr/F co-doping, the device boosted the PCE by over 19% with free hysteresis, which surpassed the undoped device. This result demonstrated the effect of Zr/F co-doping on the regulation of energy level match and conductivity of SnO_2.[234]

4.2 Bilayer ETLs

A mass of pinholes and cracks appear in the SnO_2 film during the fabrication process. The traps reduce the current leakage energy and retard the carrier transfer at the interface, resulting in current leakage in PSCs and a poor photovoltaic

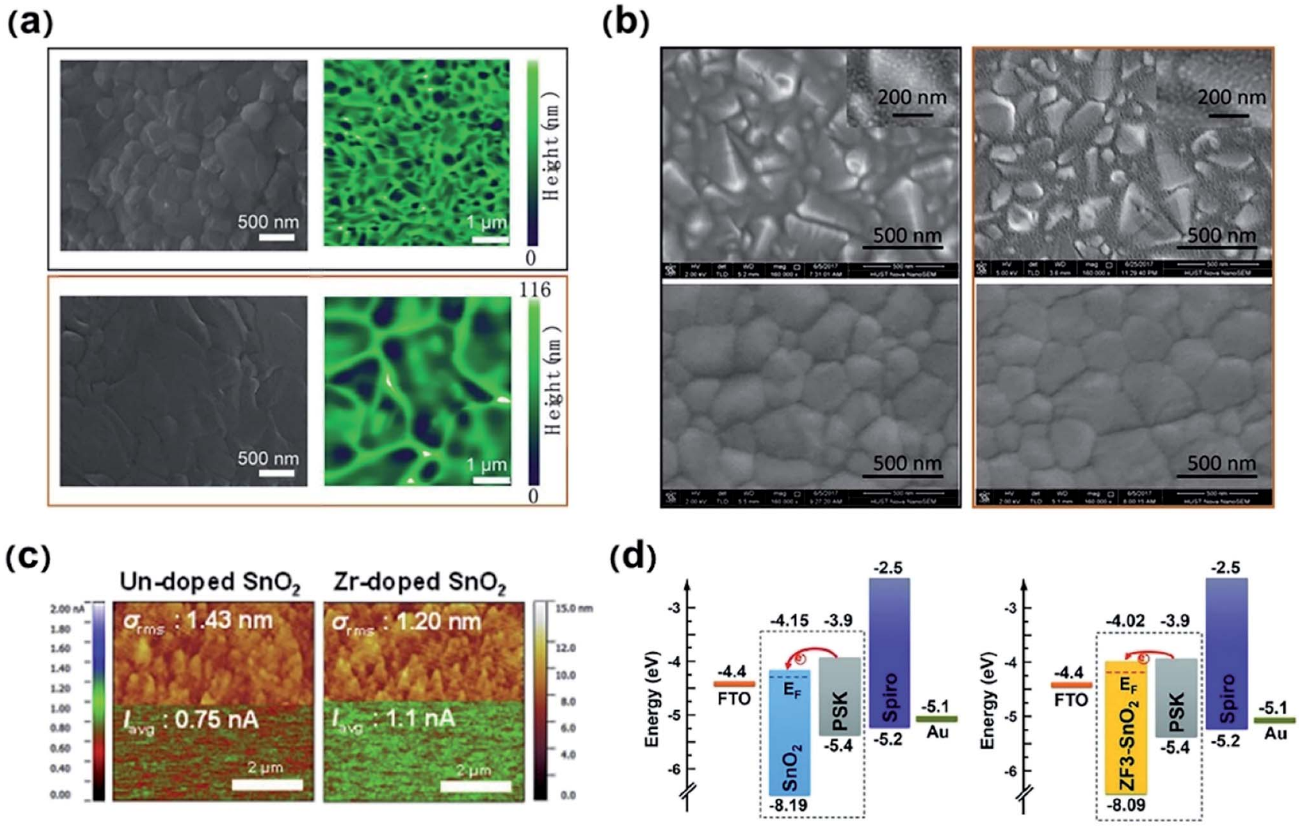

Fig. 8 (a) Top view SEM images and AFM images of perovskite films on (up) FTO/SnO_2 and (down) FTO/SnO_2–Cl. Reproduced with permission.[205] Copyright 2020, Royal Society of Chemistry. (b) SEM images of (left) SnO_2 and its perovskite (right) $F{:}SnO_2$ and its perovskite. Reproduced with permission.[207] Copyright 2020, ACS Publishing Group. (c and a) AFM and c-AFM images (bottom) of SnO_2 NPs thin films with and without Zr-doping. Reproduced with permission.[226] Copyright 2019, Elsevier. (d) Schematic of the energy level arrangement for the pristine SnO_2 device and the Zn/F doped-SnO_2 device. Reproduced with permission.[234] Copyright 2020, Wiley-VCH.

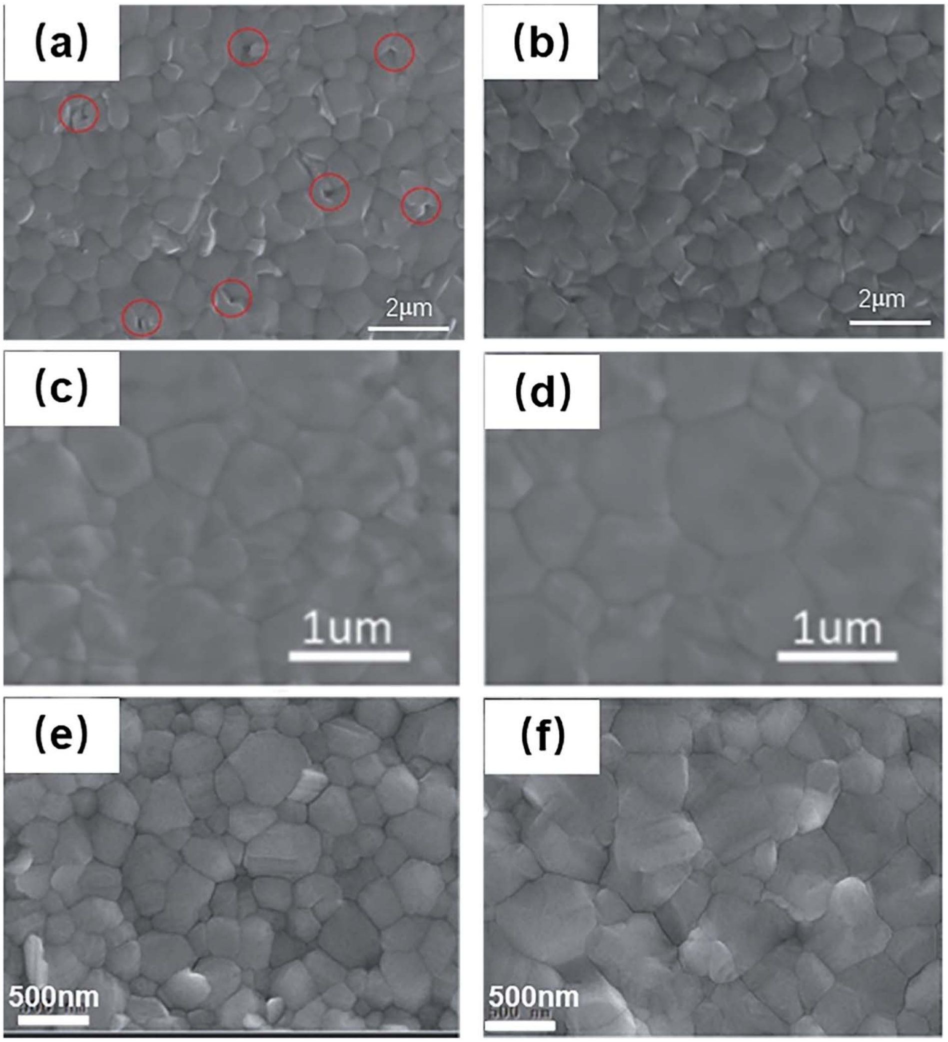

Fig. 9 Top-view SEM images of perovskite films deposited on SnO_2 and SnO_2/metal oxide ETLs. (a) SnO_2 and (b) In_2O_3/SnO_2. Reproduced with permission.[245] Copyright 2020, Wiley-VCH. (c) SnO_2; (d) WO_x/SnO_2. Reproduced with permission.[246] Copyright 2019, Elsevier B.V. (e) P–SnO_2; (f) B–SnO_2. Reproduced with permission.[247] Copyright 2021, Wiley-VCH.

performance. Bilayer ETLs based on SnO_2 films combined with a thin layer of metal oxide (*i.e.* TiO_2,[235,236] Al_2O_3,[214,237] Ga_2O_3,[238] ZnO,[239–242] SnO_2 [122,221] and $ZnTiO_3$ [243]) or organic transporting materials (PCBM and C_{60}) are used to suppress the interface and bulk defects and charge recombination.

4.2.1 SnO_2/metal oxide ETLs. In n-i-p PSC devices, bilayers of metal oxide composite structures are massively used as ETLs. For example, considering the advantages of the high electron mobility of SnO_2 ($\approx 10^{-3}$ cm^2 V^{-1} s^{-1}) compared with that of TiO_2 ($\approx 10^{-5}$ cm^2 V^{-1} s^{-1}) and the high reproducibility of TiO_2 ETLs, Mali and co-workers selected SnO_2 coated c-TiO_2 bilayer ETLs. Owing to its high conductivity, SnO_2 occupied the defect sites, which can suppress the surface traps of the TiO_2 film, leading to efficient electron extraction from the perovskite absorber. Meanwhile, the high mobility of the SnO_2 interfacial layer played a role in maintaining the charge balance of the PSC.[244]

Wang and co-workers reported a convenient low-temperature process to prepare an In_2O_3/SnO_2 bilayer as the ETL (Fig. 9a and b). The introduction of In_2O_3 was beneficial to the formation of smooth, dense, and low-defect-density perovskite films. Besides, the CB of In_2O_3 was lower than that of Sn-doped In_2O_3 (ITO), facilitating the charge transfer at the interface between perovskite and the ETL, thus reducing the V_{oc} loss. The device with a PCE of over 23% was achieved, and a high V_{oc} of 1.17 V was obtained with the potential loss (0.36 V). Additionally, the PSC retained 97.5% initial PCE after 80 days in a N_2 atmosphere without encapsulation and maintained 91% of its original PCE after 180 h under 1 AM illumination.[245]

Wang and co-workers proposed an amorphous WO_x/SnO_2 hybrid ETL to effectively block holes through the defects of the SnO_2 film to ITO, thereby promoting the charge extraction and reducing the electron–hole recombination at the interface (Fig. 9c and d). Moreover, due to the appropriate energy-level alignment and high conductivity, they also obtained better electron transfer channels. In contrast to flexible PSCs with a single SnO_2 ETL, the PSCs with an amorphous WO_x/SnO_2

hybrid ETL showed a better PCE of 20.52%. Moreover, the WO_x/SnO_2 preparation process was at a temperature below 150 °C.[246]

Ye and co-workers proposed a bilayer ETL consisting of two different SnO_2 films at a low temperature (70 °C), combined with various amounts of NH_4Cl as additives (Fig. 9e and f). The novel SnO_2 bilayer tuned the bandgap alignment at the SnO_2/perovskite interface and reduced strain in the perovskite film growth, which resulted in negligible carrier recombination, high conductivity, and low voltage loss. Finally, the best device with a doped SnO_2 bilayer ETL achieved a photovoltaic performance of 21.75% and strongly increased the V_{oc} up to 1.21 V with negligible hysteresis.[247]

4.2.2 SnO_2/fullerene derivative ETLs.

Fullerene and its derivatives with efficient charge extraction are commonly used as the ETL in p-i-n planar PSCs, including C_{60} and phenyl-C_{61}-butyric acid methyl ester ($PC_{61}BM$).[157,248–257] Owing to the drawbacks of SnO_2 in inefficient charge extraction and interfacial charge recombination, many researchers have tried to deposit the SnO_2 film combined with fullerenes or its derivatives as a bilayer to eliminate the issues in achieving efficient and stable PSCs.

Tian and co-workers used 2,5-diphenyl-C_{60}-fulleropyrrolidine (DPC_{60}) to passivate the defects on the SnO_2 film surface, forming a SnO_2/DPC_{60} bilayer structure as the ETL in PSCs (Fig. 10a, b and c). DPC_{60} can reduce charge recombination in the interface of SnO_2/perovskite and offer an appropriate band edge alignment, which led to electron transfer from the perovskite absorber to the FTO electrode. As a result, this reveals that electron extraction can be improved *via* modification on the perovskite/SnO_2 interface with (DPC_{60}). The PCE of 20.4% was obtained for PSCs based on the SnO_2/DPC_{60} bilayer, which was higher than that of 18.8% PSCs based on a single SnO_2 film.[258]

Later on, Raiford and co-workers reported an ultrathin (2 nm) layer of polyethyleneimine ethoxylate (PEIE) to functionalize the surface of C_{60} for the subsequent preparation of SnO_2 by ALD as an electron contact bilayer for p-i-n PSCs. They first used Auger electron spectroscopy (AES) mapping to shed light on the effect of PEIE on SnO_2 nucleation in C_{60}. Through a series of testing conditions in the air atmosphere with simultaneous stressors of heat and illumination, improved nucleation contributed to more stable PSCs. These devices got a high initial PCE of 18.5% with 40% improvement in stability over devices with C_{60}/SnO_2 contacts without modification with PEIE following a continuous operation at 60 °C unencapsulated in the ambient environment for 250 h.[259]

In recent, Palmstrom and co-workers investigated the impacts of SnO_2 on the perovskite film and explored the role of C_{60} as an organic electron extractor at the interface. Furthermore, they offered strategies to remove the C_{60} layer at the perovskite/SnO_2

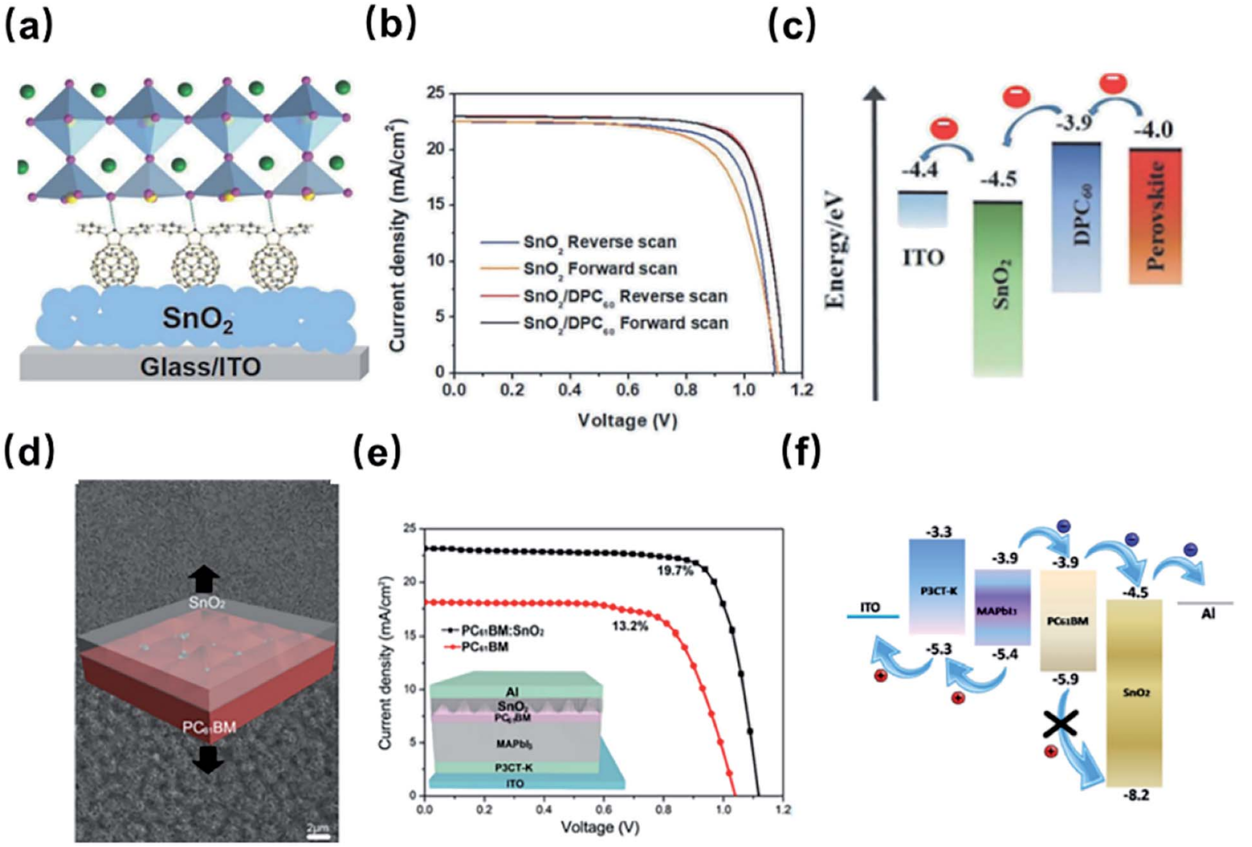

Fig. 10 (a and d) Illustrations of the interfacial treatment. (b and e) Forward and reverse scan J–V curves of devices with and without interfacial modification. (c and f) Energy band diagram of PSCs; (a–c) Reproduced with permission.[258] Copyright 2020, Wiley-VCH. (d–f) Reproduced with permission.[265] Copyright 2018, ACS Publishing Group.

interface.[260] Organic extraction layers reduced the mechanical strength and endowed the perovskite/C_{60} interface with mechanical defects in PSCs.[261,262] Owing to the high fabrication cost and poor mechanical stability of C_{60}, PCBM is desirable to reduce the need for the organic layer in future devices.

In addition to regular PSCs, SnO_2 is used in inverted PSCs as bilayers with organic transport materials, which preserve efficient electron transport and improve ambient stability. Zhu *et al.* first used the hydrothermal method to create highly crystalline SnO_2 nanocrystals (NCs) that could be used as an efficient ETL in conjunction with C_{60}. The best device, owing to its high crystallinity and hydrophobicity, achieves a high PCE of 18.8% and retains more than 90% of its initial PCE after 30 days of storage in an ambient environment with >70% relative humidity.[127] Similarly, Liu used $HClO_4$ to control crystallization during the SnO_2 deposition process. Based on the SnO_2/C_{60} bilayer, the unencapsulated inverted PSCs had a champion PCE of more than 16% and retained more than 80% of its initial PCE value after 90 days (>2100 h) of storage in an air atmosphere.[263] Luo *et al.* reported carbon nanotube films coated with SnO_2 (SnO_2@CSCNT) as ETL in the application of inverted $CH_3NH_3PbI_3$/NiO PSCs and achieved the best PCE of 14.3% with better stability under a high humidity, thermal stress, or continuous light soaking condition.[264]

Wang and colleagues used a $PC_{61}BM:SnO_2$ bilayer as the ETL in inverted PSCs and achieved a high PCE of 19.7% (Fig. 10d, e and f). The device with the $PC_{61}BM:SnO_2$ bilayer outperformed the device based on a single $PC_{61}BM$ ETL by 49.0%. The SEM revealed smooth and compact $PC_{61}BM:SnO_2$ layers with minor pinholes and cracks, promoting electron transfer and reducing charge recombination. Furthermore, the device's stability was improved over the $PC_{61}BM$-only device (Table 3).[265]

4.3 Interface modification

Although SnO_2 has excellent optoelectronic properties, defects or traps appear in SnO_2 films because of improper deposition methods, which will become the center of carrier recombination, resulting in decreased PCE. UV treatment is a common way to remove surface impurities or residuals, suppress the oxygen vacancies, and facilitate surface wettability for perovskite film growth.[102,266–269] To improve the film quality, reduce the surface defects, and facilitate interfacial contact, many researchers introduced a series of materials to passivate interfacial defects and promote the conductivity of the SnO_2 film, which are all very significant to achieve an efficient and stable PSC device, including ammonium salts, quantum dots, self-assembled monolayers, 2D materials, and carbon materials.

4.3.1 Ammonium salts. Despite its high electron mobility, SnO_2 ETL deposited at a low temperature suffers from poor film crystallinity and large defect density, which usually reduce the PSC efficiency. Ammonium salts are introduced for SnO_2 surface modification to reduce the interfacial defects.[97,247,270,271]

Chen and co-workers introduced Girard's Reagent T (GRT) into the SnO_2 NP colloidal solution and obtained a high efficiency of 21.63% with free hysteresis. The AFM and contact angle test results showed better roughness and wettability for the SnO_2 film with GRT modification due to the chemical interaction between GRT and SnO_2 NPs (Fig. 11a and b). As a result, the quality of perovskite films with GRT modification was also improved. Many holes could be effectively eliminated in the perovskite film compared with the control ones. The vertically oriented large grains were across the whole cross-section, which confirmed that GRT modification is beneficial to the SnO_2 NP dispersion and the interfacial contact between the ETL and the perovskite layer.[97]

Jung and co-workers used ammonium fluoride (NH_4F) to modify the SnO_2 surface to eliminate trap sites and change the Fermi level of SnO_2 thin films (Fig. 11c and d). They suggested that an ammonium cation in NH_4F generated ammonia gas and water vapor due to the reaction with hydroxyls on the SnO_2 surface. Besides, fluoride anions would get inserted into the trap sites, resulting in an adjustment of the energy level. PSCs with treated SnO_2 achieved a champion performance of 23.2%.[272]

Huang *et al.* showed that the addition of the IL tetramethylammonium hydroxide $N(CH_3)_4OH$ (TMAH) to the SnO_2 nanoparticle suspension to form a stable and homogeneous suspension could result in a better SnO_2 ETL with lower defect density and higher conductivity for a better FF (Fig. 11e and f).[273] As a result, TMAH-SnO_2-based PSCs showed a higher PCE (20.28%) than that of non-treated SnO_2-based PSCs (18.14%). Ethylenediaminetetraacetic acid (EDTA) is introduced onto SnO_2 to increase the electron mobility of the ETLs, resulting in a PCE of 21.60% and a certified PCE reaching 21.52%.[274]

4.3.2 Quantum dots (QDs). The quantum dots (QDs) had a tunable bandgap together with the quantum confinement and edge effects, which were novel promising zero-dimensional materials to decorate the SnO_2 surface to promote the electron conduction of SnO_2.[103,275]

Chen and co-workers developed a SnO_2/graphitic carbon nitride quantum dot ($g-C_3N_4$ QD) nanocomposite (G-SnO_2) as

Table 3 Representative PSCs based on bilayer ETLs

Bilayer	Depositon method	J_{SC} (mA cm^{-2})	V_{oc} (V)	FF (%)	PCE (%)	Ref.
SnO_2/In_2O_3	Spin-coating	24.45	1.17	87.09	23.24	245
SnO_2/a-WO_x	Vacuum thermal evaporation	23.01	1.11	80.34	20.52	246
L-SnO_2/H–SnO_2	Spin-coating	23.6	1.21	76.2	21.75	247
SnO_2/DPC_{60}	Spin-coating	23	1.14	77.7	20.4	258
SnO_2/C_{60} with PEIE	Vacuum thermal evaporation	19.66	1.154	81.8	18.5	259
$SnO_2/PC_{61}BM$	Spin-coating	23.15	1.12	76	19.7	265

the functional ETL to accurately control the interfacial charge dynamics of efficient n-i-p planar PSCs (Fig. 12a, b and c). The g-C_3N_4 QDs could suppress the oxygen-vacancy-induced traps and facilitate the interfacial charge transfer by redistributing the electronic density around the neighboring SnO_2 crystal unit, resulting in enhanced electrical properties, appropriate bandgap matching and high electron conduction. Employing the SnO_2/g-C_3N_4 QDs-based ETL, a champion PCE of 22.13% can be obtained with negligible hysteresis and long-term stability.[276]

Hui and co-workers recently reported carboxylic-acid- and hydroxyl-rich red-carbon quantum dot (RCQ) modified-SnO_2

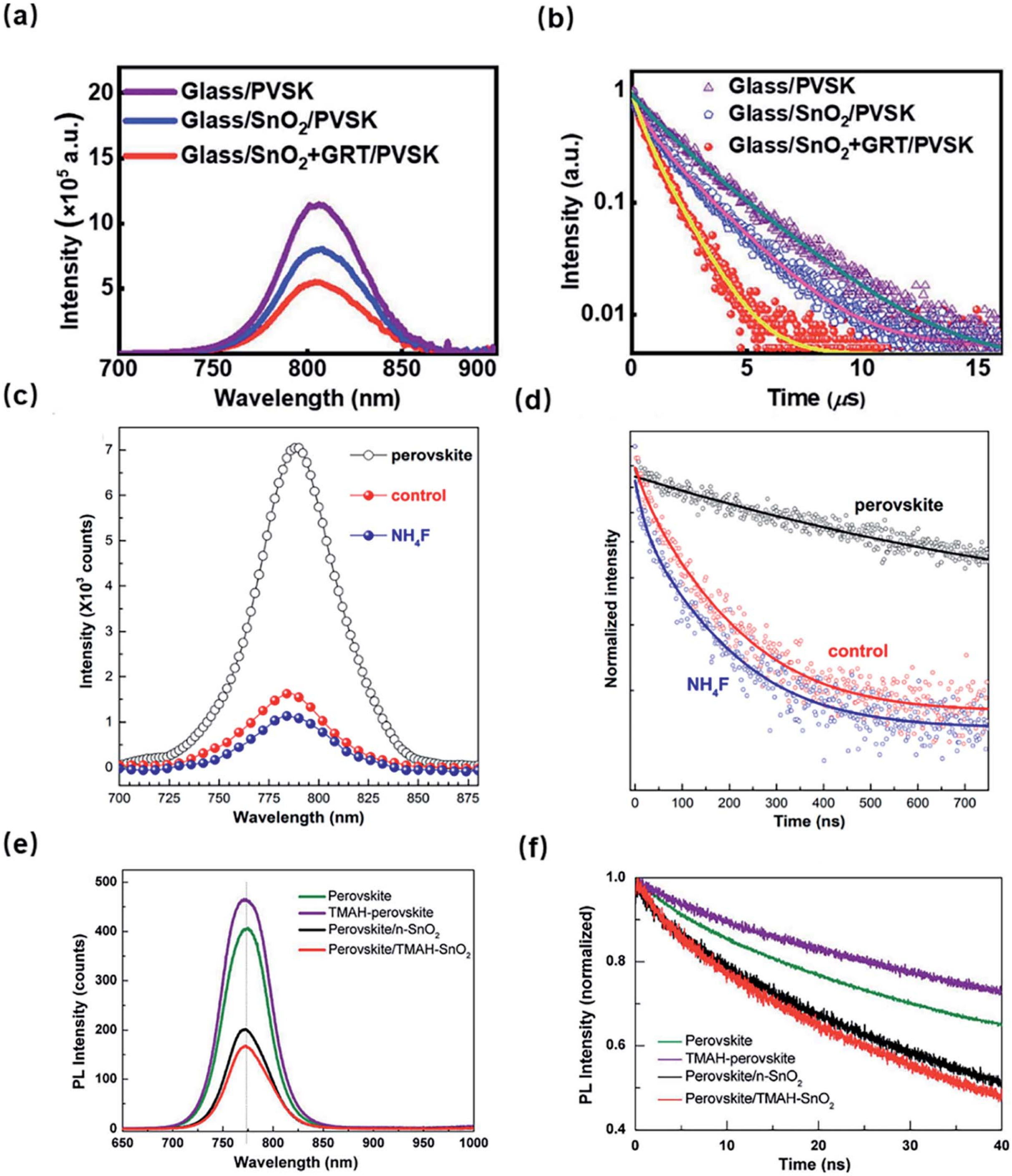

Fig. 11 Steady-state PL spectra of the perovskite film deposited on: (a) SnO_2 and GRT-SnO_2, (c) SnO_2 and NH_4F–SnO_2, (e) SnO_2 and TMAH-SnO_2. Normalized time-resolved PL: (b) SnO_2 and GRT-SnO_2 ETLs, (d) SnO_2 and NH_4F–SnO_2 ETLs, and (f) SnO_2 and TMAH-SnO_2. (a and b) Reproduced with permission.[97] Copyright 2021, Royal Society of Chemistry. (c and d) Reproduced with permission.[272] Copyright 2020, ACS Publishing Group. (e and f) Reproduced with permission.[273] Copyright 2018, Royal Society of Chemistry.

with a suitable band alignment (Fig. 12d, e and f). The calculated electron mobility of SnO_2-RCQs by using the space charge-limited current (SCLC) model was increased by 2 orders of magnitudes, resulting in a significant reduction in the conductivity of SnO_2-RCQs. Simultaneously, the RCQ modified SnO_2 layer not only passivated the ETL/perovskite interface but also facilitated the crystallinity of the perovskite film, with dense and smooth morphology over a large area. This device with modified SnO_2 obtained an outstanding efficiency of 22.77% with negligible hysteresis and showed long-term stability against moisture, maintaining over 95% of the original PCE value after 1000 h storage in an ambient environment.[277]

Xie and co-workers added graphene quantum dots (GQDs) to the SnO_2 precursor to form a SnO_2:GQDs layer as the ETL by a simple spin-coating method (Fig. 12g, h and i). It was found that GQDs effectively promoted electron transport and passivated the electron traps at the interface, which led to improved electron extraction rate and reduced charge accumulation at the ETL/perovskite interface. As a consequence, the best device based on SnO_2:GQDs ETLs exhibited a PCE of 20.23% and a free hysteresis effect.[269]

4.3.3 Self-assembled monolayers (SAMs). Like commonly used metal oxides such as TiO_2, SnO_2, ZnO, MoO_x, or organic charge transport moleculars such as $PC_{61}BM$ and poly(3,4-ethylenedioxy-thiophene)polystyrene (PEDOT:PSS), SnO_2 has hydroxyl groups at the surface of the film, and they cause defects states near the valence band, which can induce a non-radiative recombination at the SnO_2/perovskite interface.[278]

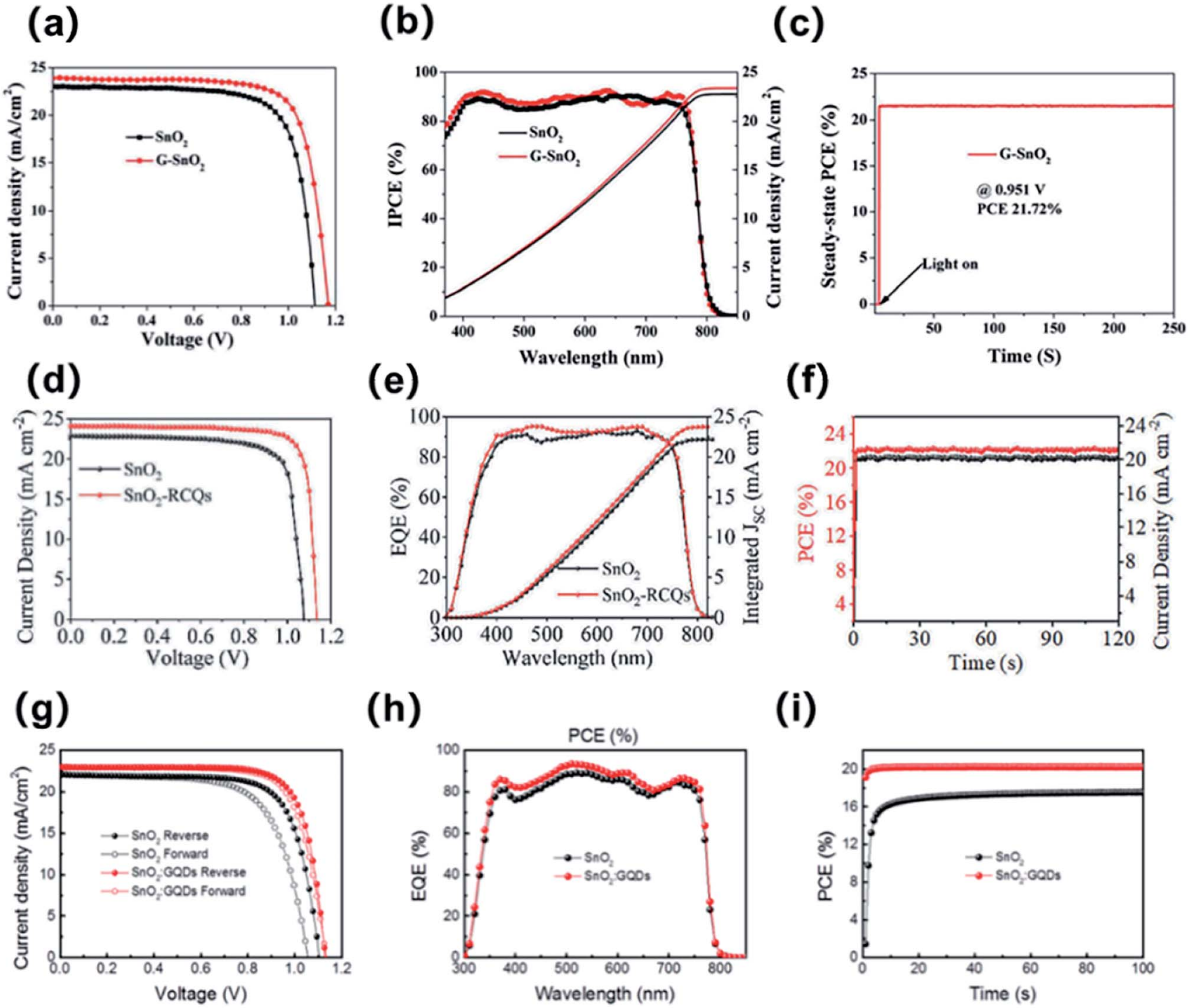

Fig. 12 *J–V* curves of perovskite solar cells based on (a) pristine and g-C_3N_4 QD-treated SnO_2 ETLs; (d) pristine and RCQ-treated SnO_2 ETLs; (g) pristine and G QD-treated SnO_2 ETLs. The corresponding IPCE spectra of (b) pristine and g-C_3N_4 QD-treated SnO_2 ETLs; (e) pristine and RCQ-treated SnO_2 ETLs; and (h) pristine and GQD-treated SnO_2 ETLs. Steady efficiency at the maximum power point of (c) pristine and g-C_3N_4 QD-treated SnO_2 ETLs; (f) pristine and RCQ-treated SnO_2 ETLs; (i) pristine and GQD-treated SnO_2 ETLs. (a–c) Reproduced with permission.[276] Copyright 2020, Royal Society of Chemistry. (d–f) Reproduced with permission.[277] Copyright 2020, Wiley-VCH. (g–i) Reproduced with permission.[269] Copyright 2017, ACS Publishing Group.

Recently, owing to chemical bonding, self-assembled monolayer (SAM) ordered arrays of organic molecules formed by the spontaneous absorption onto a surface of molecular constituents from a vapor or liquid phase, are introduced to modify the SnO_2 surface, which is beneficial to tuning the energy level, regulating the WF at the surface and promoting the charge collection.[49,279–283] Besides, SAMs can reduce the vacancies and crystal traps at the perovskite, resulting in high-quality films and improved performance and stability of PSCs.

Yan and co-workers reported a choline chloride SAM on the surface of SnO_2 (chol-SnO_2) by chemically reacting with the perovskite film to eliminate oxygen vacancies at the interface and lengthen the carrier lifetime (Fig. 13a and d). Finally, the device based on SnO_2 modified by choline chloride achieved a champion photovoltaic performance of 18.90% with free-hysteresis and a high V_{oc} (1.145 V).[284]

Kim and co-workers employed 2-[carbamimidoyl(methyl) amino]acetic acid (creatine), one of the standard amino acids in the human body, on a SnO_2 layer (Fig. 13b and e). Given the chemical structure, creatine can anchor on the surface of SnO_2 by a carboxylic acid functional group and had high polarity, leading to an increase in the charge extraction efficiency. The formamidinium-based perovskite PSC with modified SnO_2 achieved the optimal efficiency of 22.1% and maintained 90% initial performance even after 50 days.[285]

Anizelli and co-workers performed a systematic study of the application of two special SAMs, ethylphosphonic acid (EPA) and 4-bromobenzoic acid (BBA), onto SnO_2 and the NiO_2 ETL for stability. A series of stability tests of films and devices with and without SAM layers, at a working-condition temperature of 75 °C and continuous illumination, were designed. They demonstrated a distinct evolution of perovskite thin films with irradiation time by adopting SAMs, and SAMs also generated several changes in the photoelectric parameters of the devices in view of their chemical propertie and their combination with the SnO_2 and NiO_2 layers. At last, SAMs exhibited a significant effect on the lifetime of PSCs, extending up to five times that of the device's T50% (time for the efficiency to reach half of its initial value) in some cases.[286]

Hysteresis and degradation occurring in traditional PSCs structures with SnO_2 as the ETL has not been well understood. Tumen-Ulzii and co-workers modified the SnO_2 surface by a C_{60} pyrrolidine tris-acid (CPTA) SAM because of the ability to form a strong chemical interaction with the SnO_2 surface (Fig. 13c and f). Furthermore, the SAM can effectively deactivate these hydroxyl groups, which localized the positive ions, leading to the hysteresis and degradation in PSCs. After surface treatment, they obtained free-hysteresis and long-term stability PSCs with no degradation after 1000 h of continuous light incidence.[287] Although PCBM or the C_{60} buffering layer has the merits of suppressing hysteresis behavior and reducing the interfacial charge recombination loss, we do not ignore the drawbacks of difficulties in depositing them. For buffering layers, thermal deposition can precisely control its thickness, but it takes more cost and energy consumption to deposit them in a vacuum environment. On the other hand, solvent orthogonality is required to be solved because the polar solvents used in perovskite precursors like dimethylformamide (DMF) and dimethyl sulphoxide (DMSO) destroy the perovskite crystal structures.

4.3.4 Two-dimensional materials. Recently, two-dimensional (2D) materials such as graphene, MXenes, and metal sulfides have been commonly introduced into SnO_2 based on PSCs owing to their unique photoelectric

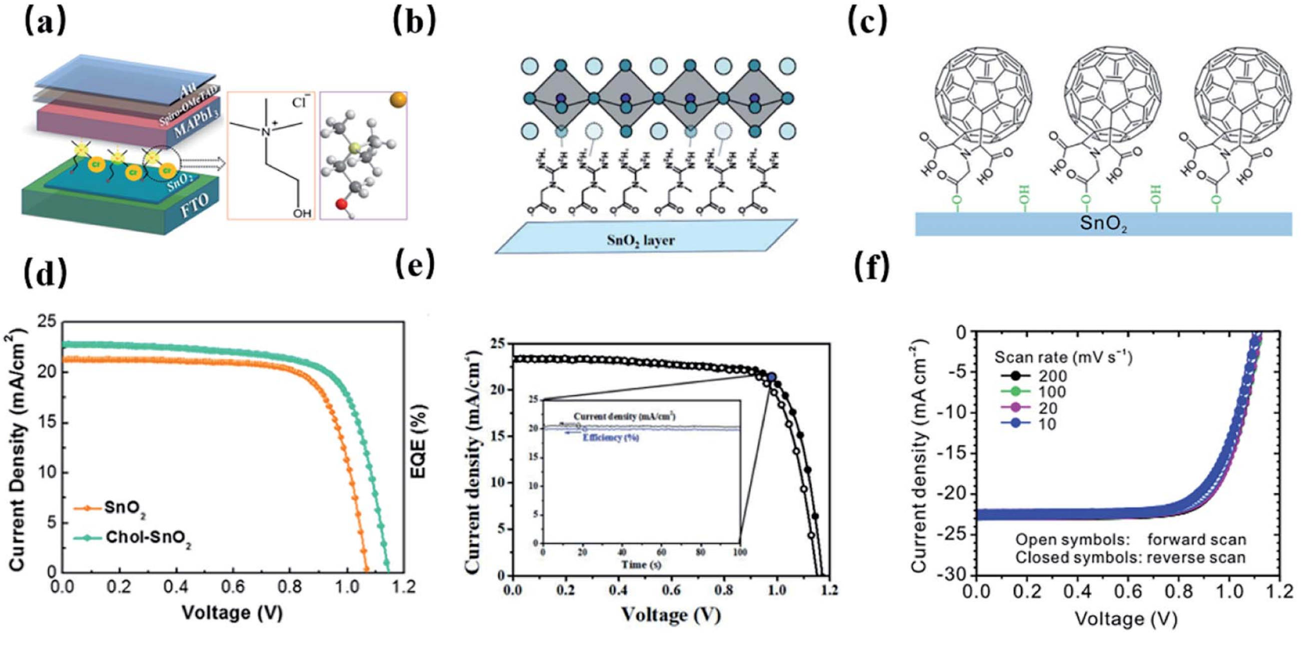

Fig. 13 Schematic illustration of the formation of various self-assembled monolayers adhering to SnO_2 layers and *J*–*V* curve of devices with different SAM treatments. (a and d) Choline chloride treatment. Reproduced with permission.[284] Copyright 2020, ACS Publishing Group. (b and e) 2-[Carbamimidoyl(methyl)amino] acetic acid treatment. Reproduced with permission.[285] Copyright 2015, Royal Society of Chemistry. (c and f) C_{60}-pyrrolidine tris-acid treatment. Reproduced with permission.[287] Copyright 2020, Nature Publishing Group.

properties.[72,77,288–291] MXenes are promising 2D materials that process high electron mobility and less light absorption in the visible range. Their general chemical formula is $M_{n+1}X_nT_x$, in which M displays a type of early transition metal, X usually is a carbon and/or a nitrogen atom, and T is the surface termination group (usually oxygen- and/or fluorine-containing groups).[292–294] Interestingly, the application of MXenes has been reported in PSCs as additives in the perovskite layer and ETLs.[291,295,296]

Wang and co-workers used $Ti_3C_2T_x$ MXene to increase the conductivity and the charge collection ability of the SnO_2 ETL. The MXene-modified SnO_2 ETL also led to a preferable growth of perovskite films with free defects. Consequently, the PSCs obtained the best photovoltaic performance of 20.65% with minimal hysteresis.[290]

Yang and co-workers introduced Ti_3C_2 (the most widely studied MXene) nanosheets into SnO_2 precursors to increase the ETL conductivity *via* a low-temperature method (Fig. 14a, b and c). Through optimizing the Ti_3C_2 contents, the device with the perovskite film of $MAPbI_3$ obtained 18.34%, which was much higher than that of only SnO_2-based PSCs. The enhancement of the PCE can be ascribed to good bandgap alignment, leading to faster charge extraction from the perovskite layer.[291]

Some metal sulfide materials are also good choices to modify the SnO_2 for enhanced electron conductivity. Huang and co-workers spin-coated the 2D TiS_2 layer on the top of SnO_2 as a bilayer ETL (Fig. 14d, e and f). 2D TiS_2 can suppress trap sites of SnO_2 and change the energy level alignment, resulting in improved electron mobility. The highest PCE reached was 21.73% with free hysteresis.[288]

4.3.5 Carbon materials. Carbon-based materials are suitable charge-transfer materials for commercializing large-scale PSCs due to low-expense, high electron conduction, especially low-temperature fabrication (100 °C),[297,298] and similar work function as gold (5.0 and 5.1 eV, respectively).[297] Besides, they possess a highly hydrophobic nature, which protect moisture infiltration into the perovskite layer, resulting in long-term stability without encapsulation.[299] Nowadays, carbon-based materials including graphene, carbon nanotubes (CNTs), and carbon or graphene nanodots are widely used in PSCs as additives in perovskite precursors, interlayers between ETL or HTL with the perovskite layer and cathode.[300–305]

Tang and co-workers prepared SnO_2 and carbon nanotubes (CNTs) hybrid ETL (SnO_2–CNT) by spin-coating method.[116] Besides, carbon nanotubes (CNTs) were modified by oxidative treatment and then dispersed well in $SnCl_4 \cdot 5H_2O$ solution (Fig. 15a and b). As a consequence, the best PCE of 20.33% was obtained with negligible hysteresis, which was attributed to the significant increase in the conductivity of SnO_2 films and decrease in the trap-state density of SnO_2 films. Wang and co-workers firstly introduced carbon nanodots (CNDs) into SnO_2 ETLs by a facile solution method. CNDs could effectively reduce the defect density and promote electron mobility in SnO_2. Finally, the device with ITO/SnO_2: CNDs/perovskite/spiro-OMeTAD/Au structure obtained a high power conversion efficiency (PCE) of over 20% with free hysteresis. Additionally, the SnO_2: CNDs device dropped only 10% of the initial PCE after storage in ambient for 1200 h and showed better UV stability after continuous UV illumination.[306]

Zhang and co-workers firstly introduced graphdiyne (GDY) as a novel carbon material to optimize the charge collocation process of SnO_2 ETL, tune the growth of perovskite and eliminate interfacial defects towards both perovskite crystallization process and subsequent photovoltaic service duration. Through

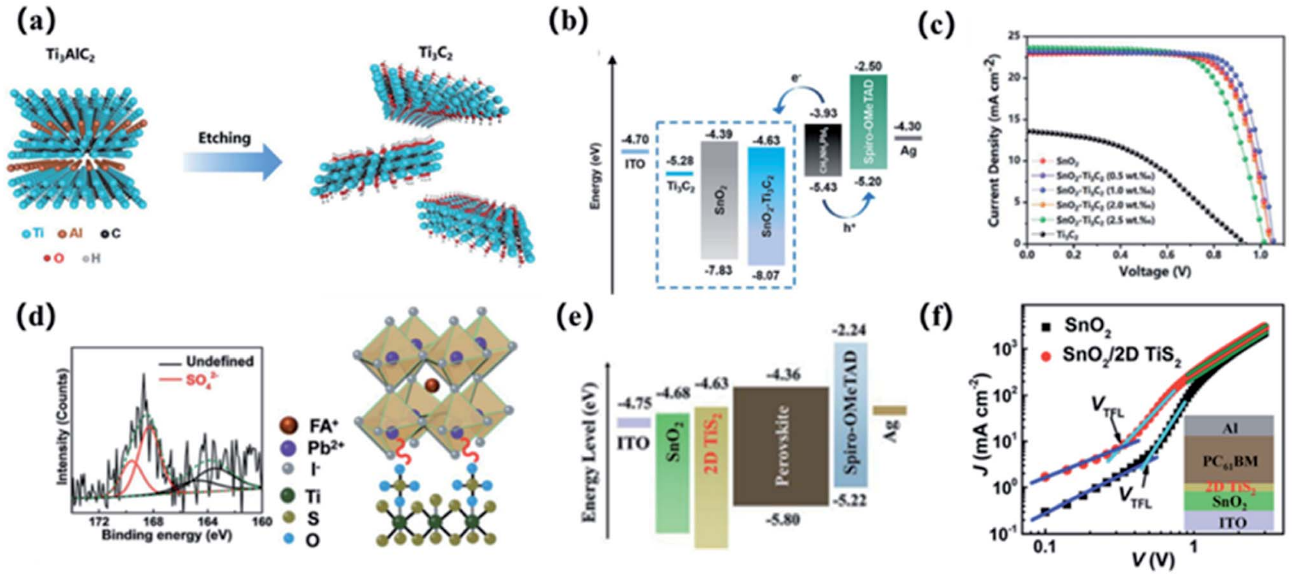

Fig. 14 (a) Schematic diagram of Ti_3C_2 formation. (b and e) Energy level diagram of the components in the semiconductor hybrid perovskite. (c) Backward scan *J*–*V* curves of devices with a SnO_2 ETL and with SnO_2–Ti_3C_2 ETLs at various Ti_3C_2 concentrations. (d) High-resolution XPS spectra of S 2p on the SnO_2–TiS_2 film; working mechanism of 2D TiS_2 interaction with the perovskite crystal; (f) *J*–*V* curves of electron-only devices with the inset illustrating the device structure. (a–c) Reproduced with permission.[288] Copyright 2019, Royal Society of Chemistry. (d–f) Reproduced with permission.[291] Copyright 2019, Royal Society of Chemistry.

the GDY modification, the PCE of over 21% was achieved with 10% improvement together with free hysteresis. It is demonstrated that GDY treated SnO_2 layer improved electron mobility and more facilitated energy level alignment (Fig. 15c and d). Moreover, the improved interfacial hydrophobicity effectively impeded excess heterogeneous perovskite nucleation, leading to the higher crystal grain size of perovskite, fewer grain boundaries, and decreased trap density.[307]

Zhao and co-workers treated SnO_2 nanocrystals by chemically modified graphene as ETL for highly efficient and stable

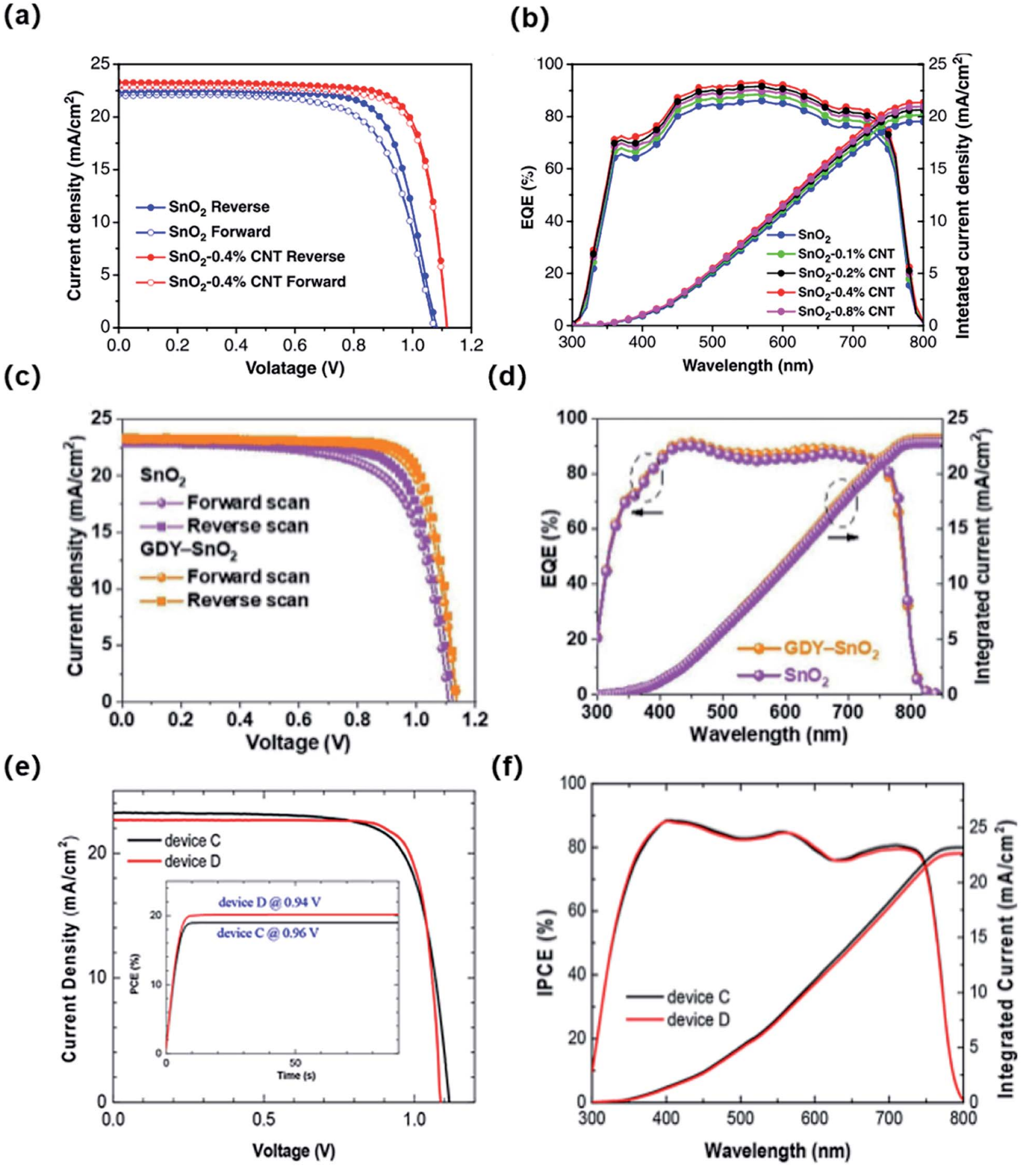

Fig. 15 *J*–*V* curves of (a) SnO_2 and CNT-SnO_2 ETLs; (c) SnO_2 and GDY-SnO_2 ETLs; (e) SnO_2 and graphene-SnO_2 ETLs. EQE spectra of (b) SnO_2 and CNT-SnO_2 ETLs. (d) SnO_2 and GDY-SnO_2 ETLs. (f) SnO_2 and graphene–SnO_2 ETLs. (a and b) Reproduced with permission.[116] Copyright 2020, Wiley-VCH. (c and d) Reproduced with permission.[307] Copyright 2020, Wiley-VCH. (e and f) Reproduced with permission.[308] Copyright 2018, ACS Publishing Group.

PSC (Fig. 15e and f). Besides, they also reported a creative strategy to disperse graphene in an aqueous solution that can preserve any residue on the SnO_2 film. Finally, the best device showed a PCE of over 20% with a high fill factor of up to 82%, which resulted from the enhanced conductivity (Table 4).[308]

5. Hysteresis and stability

The severe hysteresis and inferiority in the stability of PSCs under operation conditions are urgent challenges that quietly inhibit the PSCs from being used in the commercialization of laboratory products.

5.1 Hysteresis suppression

The presence and behavior of hysteresis, the difference in the I–V curve from the reverse scan (open-circuit to short-circuit) and the forward scan (short-circuit to open-circuit), is a fundamental problem in the perovskite solar cell field. This results in obstacles to the progress of the actual performance of the devices in operation. Compared with devices with an n-i-p structure with a scaffold and an inverted p-i-n structure with a fullerene ETL, PSCs with the regular planar structure show much more evidence of the hysteresis effect.

Although the reasons for the appearance of hysteresis in PSCs are not evident, energy defects at the interfaces, the grain boundary in the perovskite film, and capacitive and ferroelectric polarization possibly affect the hysteresis behavior.[309–312] Recently, it seems that hysteresis is induced by ion migration, which caused charge accumulation, unbalanced charge mobility, defects or traps in the instinct of perovskites and perovskite/ETL interfaces.[313–317] As mentioned above, various types of device structures exhibited different hysteresis behaviors. The contact between the perovskite and charge transport layers is the main factor within these other structures, suggesting that the contact could also influence the hysteresis.[318]

Compared with many other metal oxides as ETLs, SnO_2 has the merits of a more bottomless conduction band, higher conductivity, and electron mobility, which is beneficial to charge transfer from perovskite to ETL low charge accumulation at the interface. To date, devices based on the SnO_2 ETL in planar PSCs show a little hysteresis effect than many common metal oxides as ETLs, especially the TiO_2 ETL.[319] For PSCs with n-i-p planar structures, SnO_2 is an ideal electron transport material as the ETL to almost solve the hysteresis problem. As previously mentioned, SnO_2 combined with doped elements,[320] bilayers,[247,321,322] and interfacial engineering[323,324] can retard the formation of the defect states, which improve the carrier transport performance, leading to negligible hysteresis in the device.

Tumen-Ulzii and co-workers treated the SnO_2 surface with a self-assembled monolayer and achieved a hysteresis-free PCE over 18% (Fig. 16). It was found that hydroxyl groups existing at the SnO_2 surface induced positive ion localization, resulting in hysteresis and degradation. Interestingly, a self-assembled monolayer of a fullerene derivative (CPTA-SAM) can effectively deactivate these surface –OH groups. The temperature and scan speed can affect the hysteresis. Besides, with temperature increase or scan speed decrease, more significant hysteresis is apparent in J–V curves. PSCs with CPTA-SAM treatment significantly reduced the J–V hysteresis of PSCs at different scan speeds in contrast to devices without CPTA-SAM treatment. Furthermore, negligible hysteresis was observed in PSCs with the CPTA-SAM even at a high temperature of 60 °C.[287]

Ye and co-workers spin-coated KCl and NaCl on the SnO_2 surface to suppress the hysteresis in flexible PSCs.[325] The KCl and NaCl treatments effectively improve the power output of flexible PSCs. However, devices with NaCl modification showed a profound hysteresis effect in J–V curves. It suggested that the hysteresis relied strongly on alkali metals. With the increase of the ionic radius of alkali metal ions from Li^+ to K^+ and then to Cs^+, the hysteresis effect first gradually decreased and disappeared, and then appeared again and increased, which was strongly related to the trapping density.[326,327] In addition, it can reduce the device hysteresis to use a suitable SnO_2 fabrication process such as ALD, CBD, *etc.*

Table 4 Representative PSCs with interface modification

	Passivation materials	J_{sc} (mA cm^{-2})	V_{oc} (V)	FF (%)	PCE (%)	Ref.
Ammonium salts	Girard's reagent T	22.92	1.146	82.3	21.63	97
Ammonium salts	NH_4F	24.60	1.16	81.4	23.2	272
Ammonium salts	$N(CH_3)_4OH$	22.51	1.14	79	20.28	273
Ammonium salts	EDTA	24.57	1.11	79.2	21.6	274
QDs	g-C_3N_4	23.03	1.176	78.3	22.13	276
QDs	RCQ	24.10	1.14	83	22.77	277
QDs	GQD	23.05	1.134	77.8	20.31	269
SAMs	Choline chloride	22.80	1.145	72.41	18.90	284
SAMs	Creatine	23.4	1.19	75.9	20.8	285
2D materials	$Ti_3C_2T_x$	24.34	1.11	76.4	20.65	290
2D materials	Ti_3C_2	23.14	1.06	75	18.34	291
2D materials	TiS_2	24.57	1.11	79.4	21.73	288
Carbon materials	CNDs	23.26	1.12	78.23	20.33	116
Carbon materials	CNDs	23.14	1.10	79	20.03	306
Carbon materials	Graphdiyne	23.32	1.137	79.62	21.11	307
Carbon materials	Graphene	22.66	1.084	82.1	20.16	308

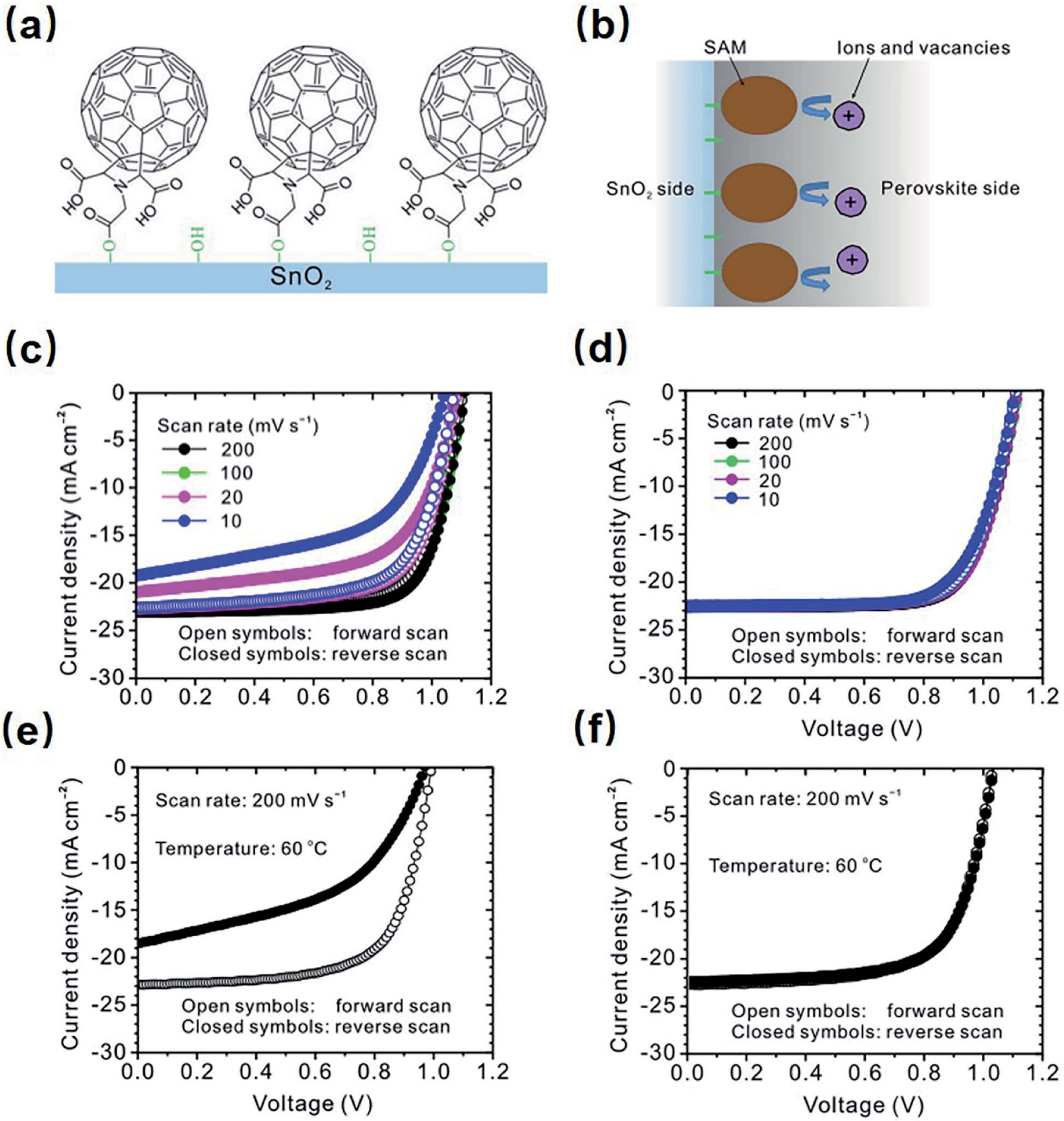

Fig. 16 Positive effect of using a self-assembled monolayer (SAM) on the hysteresis and carrier recombination characteristics in perovskite solar cells. (a) Mixed self-assembled monolayers adhering to the SnO_2 substrates and (b) schematic illustration of reducing localized ionic charges by eliminating –OH groups on the surface; backward and forward scan *J*–*V* curves at different scan speeds: (c) untreated devices and (d) devices with SAM treatment; backward and forward scan *J*-*V* curves measured at a fast scan rate of 200 mV s^{-1} at 60 °C: (e) untreated devices and (f) devices with SAM treatment. Reproduced with permission.[287] Copyright 2020, Nature Publishing Group.

5.2 Device stability

5.2.1 Ambient stability. SnO_2 is more stable in oxygen and moisture than TiO_2, an ideal alternative to the TiO_2 ETL for device stability.[188,328,329] Zhang and co-workers found that using poly(vinylpyrrolidone)-doped SnO_2 as the ETL, 88% of its highest PCE is retained even after 41 days of storage without encapsulation.[330] Huang and co-workers also revealed that the SnO_2 ETL modified with polymer ethoxylated polyethylenimine (PEIE) indicated significant storage device stability, and the device with SnO_2:PEIE ETL preserved 82.1% of its original PCE ($\mathrm{PCE}_{\frac{1}{4}}$, 16.89%) after 70 days of storage.[331] Wang and co-workers designed TiO_2/SnO_2 bilayer as the ETL in $CsPbI_2Br$ all-inorganic perovskite, and the devices showed superior photovoltaic properties, particularly excellent phase and thermal stability. After one month of storage in an N_2 environment without any encapsulation, the PCE can retain about 95% of the original efficiency (Fig. 17a and b).[332]

Apart from SnO_2 as ETLs in regular structures, SnO_2 can be introduced as a protecting layer on the top of the perovskite layer or fullerene layer.[87,127,265,333,334] Wang and co-workers used SnO_2 nanocrystals combined with $HClO_4$ and HCl treatment as a buffer layer, inserting it into the C_{60}/Ag electrode interface (Fig. 17c and d). The devices with the $HClO_4$–SnO_2 ETL without encapsulation increased the PCE up to 16.36% with almost negligible hysteresis and maintained over 80% of their highest PCE after storage in open air for 90 days (>2100 h) and reduced by only about 20% its initial efficiency after 41 h under heating at 85 °C.[263]

5.2.2 Light illumination stability.

TiO_2 is a common metallic oxide used as the ETL, which induces decomposition of PSC under UV illumination owing to their photocatalytic activity. Due to the efficiency and stability degradation, there is a mass of oxygen vacancies in the TiO_2 lattice, which can be generated by UV illumination.[200] The oxygen vacancies cause deep trap states, interacting with molecular oxygen in ambient air, and then cause deep trap sites, which can interact with molecular oxygen in the environment by adsorption, leading to their passivation.[41,335,336] When deep traps are excited by oxygen desorption, the charge recombination easily occurs at the interface, resulting in a PCE loss. Besides, TiO_2 is able to obtain excess electrons from perovskite because of its high photochemical activity, which can cause photo-decomposition of the perovskite crystals, particularly in the humid environment.[337–339]

Liu and co-workers studied the reasons for the degradation process of the perovskite layer deposited on different ETLs (PCBM, TiO_2, and SnO_2) under strong ultraviolet irradiation. Although the SnO_2 layer reduced light-induced chemical activity in contrast to the TiO_2 layer, the serious decomposition of perovskite observed at the perovskite/SnO_2 interface, together with the formation of hole structures, decreases the carrier transfer at the interface, owing to the separation of the perovskite absorber from ETLs and thus rapidly decreased the device performance (Fig. 18b).[340] Wang and co-workers used carbon nanodots (CNDs) to dope SnO_2 as the ETL and found that SnO_2:CNDs based PSCs achieved an efficiency over 20% with nearly free hysteresis and maintained over 90% of the initial PCE in a N_2 atmosphere for 1200 h and showed better UV stability under UV illumination for 200 h.[306]

Similarly, Abate and co-workers reported that Ga doping could improve UV-resistant mesoporous SnO_2. When SnO_2 and TiO_2 based PSCs were exposed to continuous light illumination for 1000 h, both devices exhibited a rapid decrease to 80% in the first 100 h (Fig. 18a). After this, SnO_2 based PSCs retained

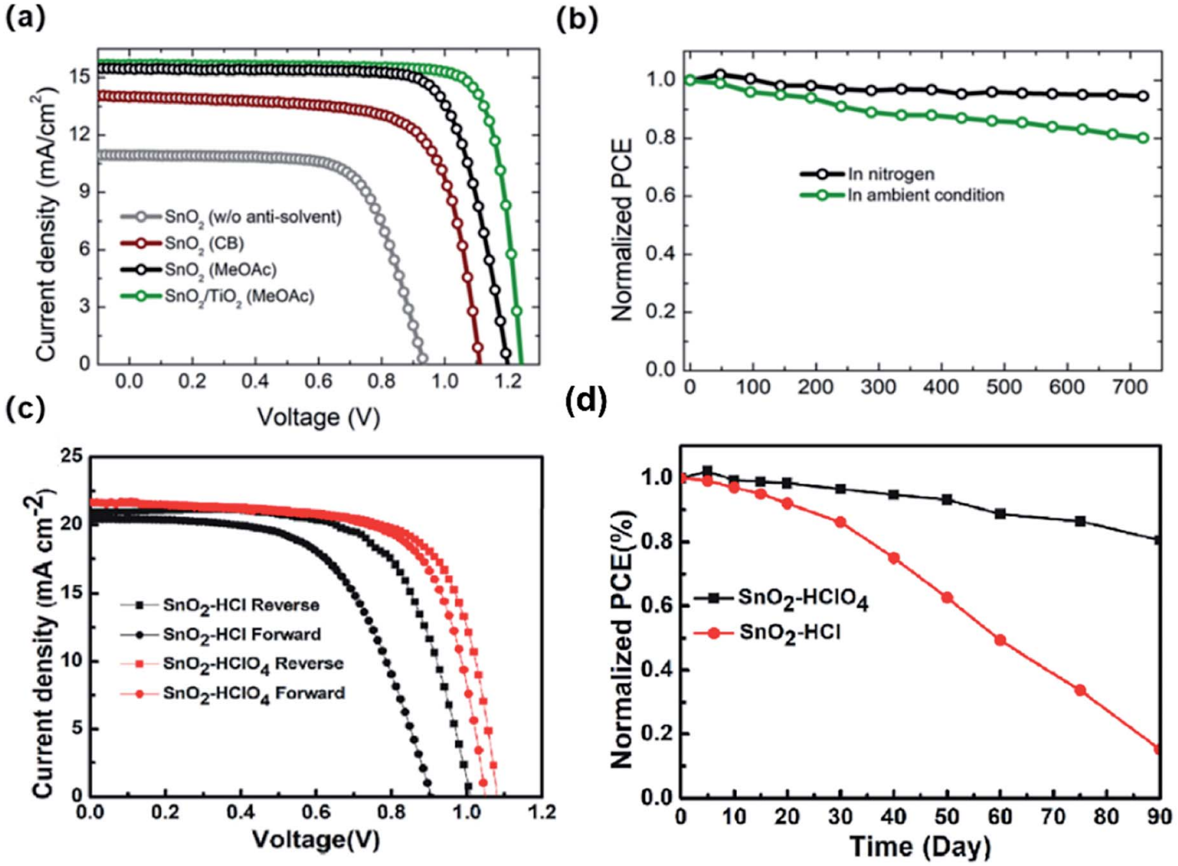

Fig. 17 *J–V* curves of devices based on (a) SnO_2 and TiO_2/SnO_2 ETLs and (c) HCl–SnO_2 and $HClO_4$–SnO_2 ETLs. Stability test of devices on (b) SnO_2 and TiO_2/SnO_2 ETLs in an N_2 – filled glovebox and under ambient conditions (@R.T., 20–30% relative humidity) (d) HCl–SnO_2 and $HClO_4$–SnO_2 ETLs under the humidity of 55% ± 10% at 85 °C in open air. (a and b) Reproduced with permission.[332] Copyright 2020, ACS Publishing Group. (c and d)Reproduced with permission.[263] Copyright 2020, Elsevier.

around 70% of the original efficiency up to 1000 h of full-spectrum illumination. In contrast, the normalized PCE of TiO_2 based PSCs dropped rapidly and stabilized only 20% of the initial PCE after illumination.[339]

Wang and co-workers introduced a chlorine-rich perovskite interlayer (ClMPI) to modify the SnO_2 ETL/perovskite interface through halide exchange to improve the interfacial charge transfer (Fig. 18c). Encouragingly, the ClMPI-based PSC still maintained over 82% of the initial PCE under UV exposure with a high power of 100 mW cm^{-2} after 500 h.[341]

More encouragingly, Gratzel and co-workers designed a bilayer ETL of an amorphous SnO_2 coated TiO_2 scaffold (mp-TiO_2) layer, and they displayed that the devices with a TiO_2/SnO_2 bilayer ETL rendered them more resistant to UV light than devices with only mp-TiO_2 as a single ETL (Fig. 18d).[342]

5.2.3 Heat stability.

In addition to light and humidity, thermal treatment is also the cause of poor stability problems of perovskite solar cells. The temperature of the cells can increase under exposure to sunlight, resulting in accelerated degradation, especially for MA-based perovskite solar cells.[343] Some strategies were reported, such as designing 2D/3D heterojunctions, using a green antisolvent, interface engineering, and additive engineering for SnO_2-based perovskite solar cells.[344–350]

Chen and coworkers deposited 4-imidazoleacetic acid hydrochloride (ImAcHCl) on the top of the SnO_2 film, leading to a chemical bridge between SnO_2 and perovskite through an ester bond with SnO_2 (Fig. 19a). As a result, ImAcHCl could improve the perovskite crystallization, suppress the non-radiative recombination, and the promote carrier lifetime. Moreover, an unencapsulated device with ImAcHCl-modified SnO_2 retained 90% of its initial after 40 h of aging at 80 °C, while PCE was degraded by 53% for the control device.[344]

Zhang and coworkers used ethyl acetate (EA) as a green antisolvent to control the perovskite crystallization process, resulting in smooth and dense perovskite films with free pinholes (Fig. 19b). In the ambient atmosphere, the unencapsulated device maintained about 85% of its initial PCE after more than 1900 h of storage. Meanwhile, the device also showed remarkable thermal stability, retaining 81.03% of the original PCE value at 100 °C for 10 h.[349]

Interface engineering between SnO_2 and the perovskite layer is a common way to improve thermal stability. Tian and coworkers synthesized 2,5-diphenyl C_{60} fulleropyrrolidine (DPC_{60}) as an interfacial layer between perovskite and SnO_2 in planar perovskite solar cells (PSCs) (Fig. 19c). As a result, PSCs modified with DPC_{60} obtained a PCE of 20.4% with high reproducibility. Furthermore, the device retained 82% of its initial efficiency after 200 h of 1 sun continuous irradiation and thermal aging (55 ± 5 °C) due to the suppression of heterogeneous nucleation and improvement in the crystallinity of the perovskite film.[348] Similarly, Choi and coworkers exhibited a PCE of 21.43% by incorporation of SnO_2 with a zwitterionic compound (3-(1-pyridinio)-1-propane sulfonate), which led to improved PCE and thermal stability (Fig. 19d).[345]

6. Commercialization and applications

6.1 Flexible perovskite solar cells (FPSCs)

Because of their potential in portable electronics, flexible perovskite solar cells (FPSCs) have sparked widespread research interest. Because of their low-temperature processability, SnO_2 ETLs play a critical role in realizing highly efficient flexible PSCs.[351–353]

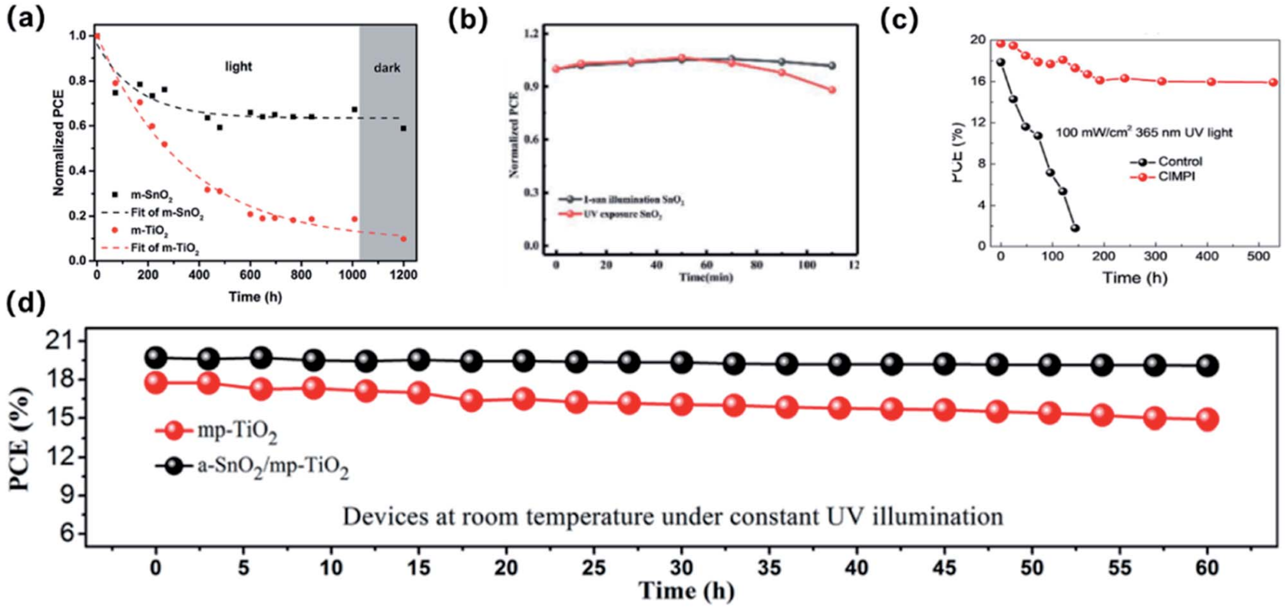

Fig. 18 UV light aging test of devices based on (a) m-SnO_2 and m-TiO_2 under 100 mW cm^{-2} illumination in a N_2 atmosphere; reproduced with permission.[339] Copyright 2018, Royal Society of Chemistry. (b) mp-SnO_2 under one sun illumination and UV exposure in a N_2 atmosphere. Reproduced with permission.[340] Copyright 2020, Royal Society of Chemistry. (c) ClMPI-SnO_2 reproduced with permission.[341] Copyright 2019, Elsevier B.V. (d) mp-TiO_2 and SnO_2/mp-TiO_2. Reproduced with permission.[342] Copyright 2018, ACS Publishing Group.

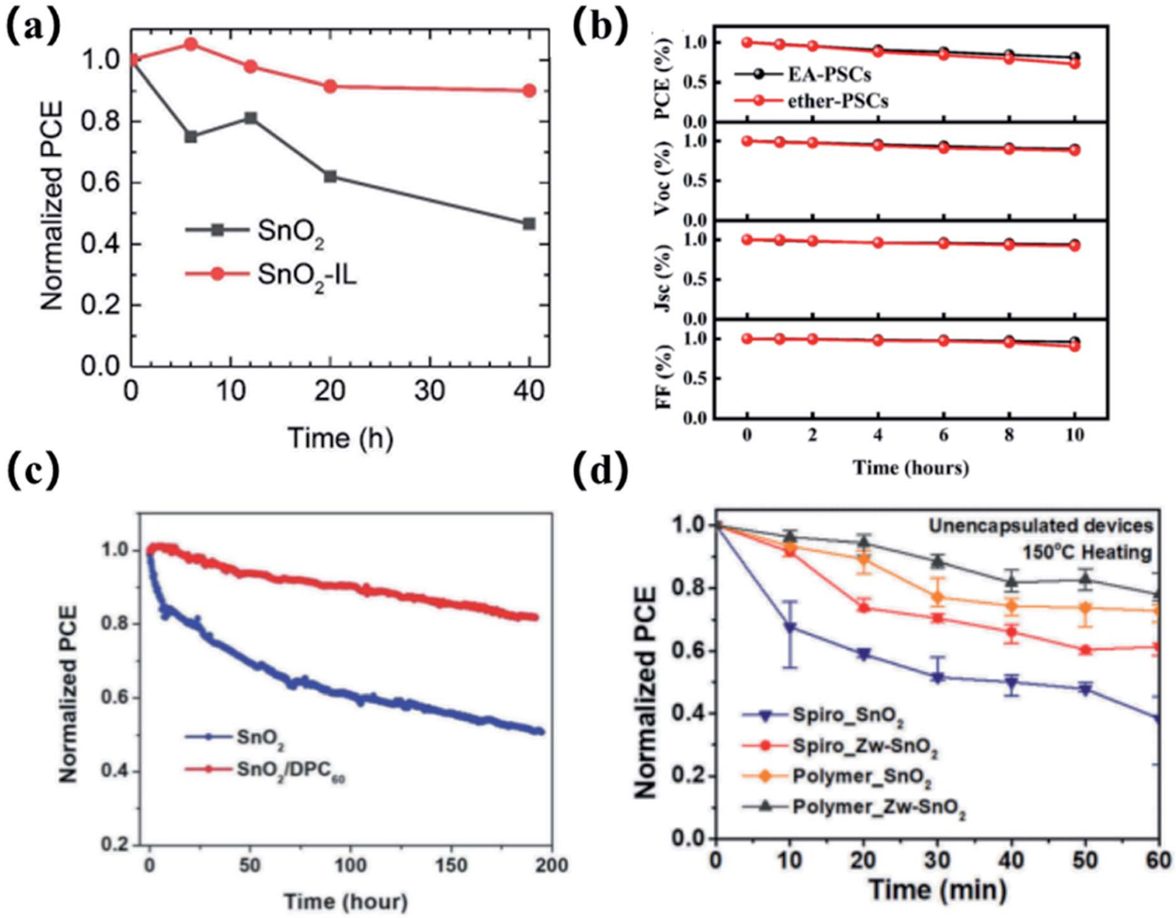

Fig. 19 Device thermal stability of (a) unencapsulated devices at 85 °C in the dark in the glovebox. Reproduced with permission.[344] Copyright 2019, Wiley-VCH. (b) Unencapsulated devices at 100 °C in air. Reproduced with permission.[349] Copyright 2020, Elsevier. (c) MPP tracking of the unencapsulated devices at (55 ± 5 °C) in a N_2 atmosphere. Reproduced with permission.[348] Copyright 2020, Wiley-VCH. (d) Unencapsulated devices at 150 °C in air. Reproduced with permission.[345] Copyright 2018, Royal Society of Chemistry.

Zhou *et al.* reported graphene quantum dots (GQDs)/SnO_2 composites (G@SnO_2) as effective ETLs. GQDs can improve SnO_2 electron mobility and coverage. Furthermore, G@SnO_2 has a higher energy level than that of pristine SnO_2, resulting in increased charge transfer and decreased charge recombination. As a result, the flexible PSCs based on G@SnO_2 ETLs achieved a champion PCE of 17.7% with exceptional mechanical durability, retaining more than 91% of the initial PCE value after 500 bending cycles with a bending radius of 7 mm.[354]

Wang *et al.* reported plasma-enhanced atomic layer deposition (PEALD) for SnO_2 ETLs processed at low temperatures. The PEALD-synthesized SnO_2 is postannealed at 100 °C in the presence of water vapor. Finally, the best flexible PSC demonstrated the highest reported efficiency of 18.36%.[155]

Dong *et al.* used ultraviolet ozone (UVO) pretreatment to introduce controlled trace amounts of surface absorbed water on the FTO or ITO for a full-coverage SnO_2 ETL with desirable morphology and crystallinity. It demonstrated optimal hydrolysis–condensation reactions for SnO_2 regrowth. Compared to the control SnO_2 ETL without UVO pretreatment, the rigid and flexible PSC devices with UVO pretreatment achieved high PCEs of up to 20.5% and 17.5%, respectively.[355]

However, the reported flexible PSCs are almost based on small surface areas to date. It is well known that low-temperature processable SnO_2 provides fundamental support for mass production *via* some scalable fabrication and coating techniques, with enormous potential for practical applications in light, wearable, and portable electronic devices.

6.2 Large-area perovskite solar cells

Large-area fabrication is a critical component in achieving industrial production and commercialization. In general, when the area of the devices is increased to a large scale, the PCE decreases due to the inevitable loss of homogeneity in the films. As a result, various scalable deposition methods and related morphology control strategies for large-area uniform SnO_2 films are developed, determining the performance of large-area flexible PSCs. A solution-based scalable deposition method appears to be promising for preparing large-area SnO_2 films. In the lab, spin-coating is the most commonly used method for producing PSCs; however, it is hard to use it in the large-area fabrication.[356,357] Other new methods for scalable production include slot-die,[103] spray-coating,[358] CBD,[359,360] sputtering,[148,149] and bar coating.[361]

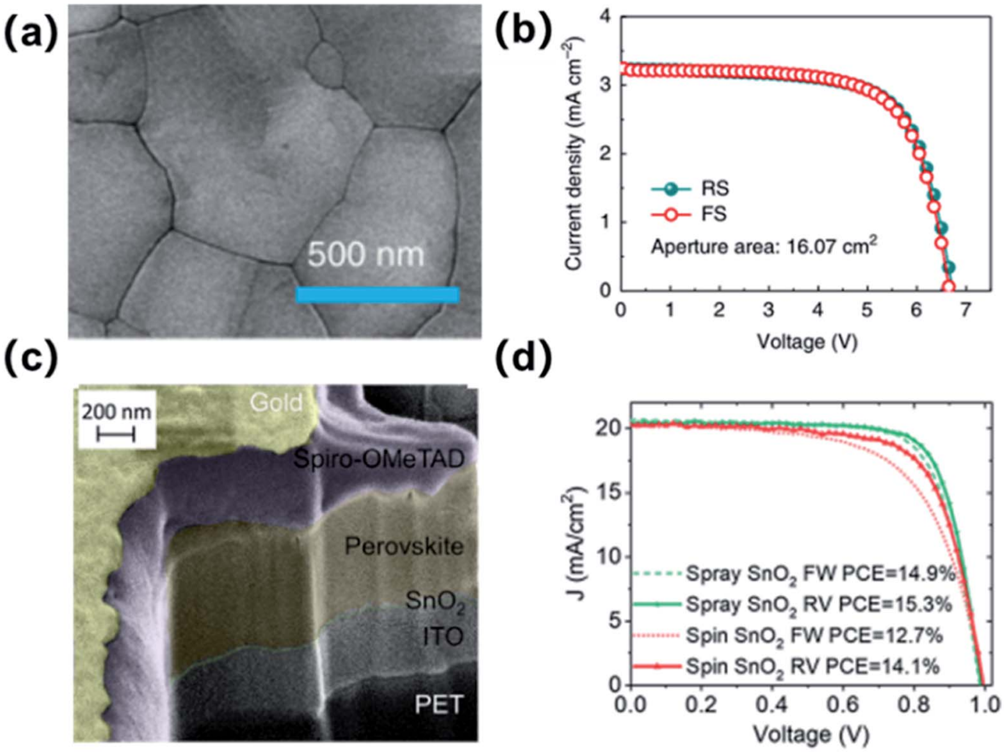

Fig. 20 Top view SEM images of (a) a perovskite film based on SnO_2 fabricated by slot-die coating; (c) the cross-sectional SEM images of a perovskite solar cell based on SnO_2 fabricated by spray-coating; forward/reverse scan J–V curve of (b) the best device based on SnO_2 fabricated by slot-die coating; (d) the best device based on SnO_2 fabricated by spray-coating. (a and b) Reproduced with permission.[103] Copyright 2020, Nature Publishing Group; (c and d) Reproduced with permission.[358] Copyright 2021, ACS Publishing Group.

Bu *et al.* slot-die-coated SnO_2 on 5 × 6 cm^2-sized substrates with a potassium interfacial passivation strategy and achieved a 14.89% efficiency (Fig. 20a and b). The results demonstrated that potassium passivation could stabilize SnO_2 colloids, reducing hysteresis in SnO_2-based devices.[103] Taheri *et al.* pioneered the concept of combining laser scribing optimization with automated spray-coating of SnO_2 layers for FPSCs (Fig. 20c and d). The method produced uniform and dense SnO_2 ETLs with PCEs of 12% and 10.7% with active areas of 16.84 and 21.2 cm^2, respectively.[358] Qiu *et al.* looked into the effect of an oxidizing environment on the formation of SnO_2 films. As an example, the champion device with an aperture area of 22.8 cm^2 demonstrated a PCE of 12.03%. Currently, the largest SnO_2-based PSC obtained by CBD deposition was 53.64 cm^2 (active area) on a 100 cm^2 substrate, with a certified PCE of 17.4%.[360]

The manufacturing cost of SnO_2 films is an important parameter for scalable SnO_2 fabrication. Appropriate deposition methods and raw materials can significantly reduce costs. Instability, on the other hand, can seriously shorten the device's lifespan. As a result, the optimized deposition methods, passivation strategies, and encapsulation have a high potential for scaling up PSCs.

7. Conclusions and outlook

SnO_2 has many merits of direct bandgap, high conductivity, low trap density, and being solution-processable under low-temperature conditions, which has been regarded as an ideal electron transport material in the field of PSCs. So far, the champion efficiency of SnO_2 ETL-based planar PSCs combined with passivation strategy has been increased to 25.2%, which approached the device with the mesoporous structure.

SnO_2-based PSCs have distinctive device structures, including planar, mesoporous, distressed, and flexible substrate-based structures. Different testimony techniques for SnO_2 to suit various structures have been reported. Although the annealing temperature is much lower than that of TiO_2 preparation, it is still excessively high to flexible PSCs or inversed structure PSCs. Subsequently, loads of work should be promoted to bring down the process temperature and simplify the process.

Like other metal oxidation, pristine SnO_2 films contain many bulk and surface defects. As previously mentioned SnO_2 combined with doped elements, bilayers, and interfacial engineering can retard the formation of the defect states, which improves the carrier transport performance, leading to negligible hysteresis in the device. To guide the design of an efficient process, we need to fully characterize the types and density of defects that form in SnO_2 and the followed perovskite to gain a fundamental understanding. In addition, standard characterization protocols should be established to properly evaluate the effect of interfacial modifiers on the performance and stability of PSCs. In principle, a molecular library could be found by investigating the effect of functional groups, the conjugated system, and the substituent of the additives or interfacial modifiers on the passivation capacity. With the research information amassed and distributed in the entire exploration field, we can utilize AI to find the basic standards for choosing the materials and effective processes.

Conflicts of interest

The authors declare no conflict of interest.

Acknowledgements

This work was financially supported by the National Nature Science Foundation of China (21676188).

References

1 Q. A. Akkerman and L. Manna, *ACS Energy Lett.*, 2020, **5**, 604–610.
2 C. Case, N. Beaumont and D. Kirk, *ACS Energy Lett.*, 2019, **4**, 2760–2762.
3 M. Jeong, I. W. Choi, E. M. Go, Y. Cho, M. Kim, B. Lee, S. Jeong, Y. Jo, H. W. Choi and J. Lee, *Science*, 2020, **369**, 1615–1620.
4 X. Lin, D. Cui, X. Luo, C. Zhang, Q. Han, Y. Wang and L. Han, *Energy Environ. Sci.*, 2020, **13**, 3823–3847.
5 F. Zhang, H. Lu, J. Tong, J. J. Berry, M. C. Beard and K. Zhu, *Energy Environ. Sci.*, 2020, **13**, 1154–1186.
6 A. Kojima, K. Teshima, Y. Shirai and T. Miyasaka, *J. Am. Chem. Soc.*, 2009, **131**, 6050–6051.
7 A. R. b. M. Yusoff and M. K. Nazeeruddin, *Adv. Energy Mater.*, 2018, **8**, 1702073.
8 M. Kim, G.-H. Kim, T. K. Lee, I. W. Choi, H. W. Choi, Y. Jo, Y. J. Yoon, J. W. Kim, J. Lee, D. Huh, H. Lee, S. K. Kwak, J. Y. Kim and D. S. Kim, *Joule*, 2019, **3**, 2179–2192.
9 H. Min, M. Kim, S.-U. Lee, H. Kim, G. Kim, K. Choi, J. H. Lee and S. I. Seok, *Science*, 2019, **366**, 749–753.
10 N. J. Jeon, H. Na, E. H. Jung, T.-Y. Yang, Y. G. Lee, G. Kim, H.-W. Shin, S. I. Seok, J. Lee and J. Seo, *Nat. Energy*, 2018, **3**, 682–689.
11 W. S. Yang, B.-W. Park, E. H. Jung, N. J. Jeon, Y. C. Kim, D. U. Lee, S. S. Shin, J. Seo, E. K. Kim and J. H. Noh, *Science*, 2017, **356**, 1376–1379.
12 H. Zhu, Y. Ren, L. Pan, O. Ouellette, F. T. Eickemeyer, Y. Wu, X. Li, S. Wang, H. Liu and X. Dong, *J. Am. Chem. Soc.*, 2021, **143**, 3231–3237.
13 M. Saliba, J. P. Correa-Baena, M. Grätzel, A. Hagfeldt and A. Abate, *Angew. Chem., Int. Ed.*, 2018, **57**, 2554–2569.
14 S. Yun, Y. Qin, A. R. Uhl, N. Vlachopoulos, M. Yin, D. Li, X. Han and A. Hagfeldt, *Energy Environ. Sci.*, 2018, **11**, 476–526.
15 V. M. Goldschmidt, *Naturwissenschaften*, 1926, **14**, 477–485.
16 B. Saparov and D. B. Mitzi, *Chem. Rev.*, 2016, **116**, 4558–4596.
17 J. You, L. Meng, T.-B. Song, T.-F. Guo, Y. Yang, W.-H. Chang, Z. Hong, H. Chen, H. Zhou, Q. Chen, Y. Liu, N. De Marco and Y. Yang, *Nat. Nanotechnol.*, 2016, **11**, 75–81.
18 F. Zhang and K. Zhu, *Adv. Energy Mater.*, 2020, **10**, 1902579.
19 J. Jeong, M. Kim, J. Seo, H. Lu, P. Ahlawat, A. Mishra, Y. Yang, M. A. Hope, F. T. Eickemeyer and M. Kim, *Nature*, 2021, **592**, 381–385.
20 W. Hu, W. Zhou, X. Lei, P. Zhou, M. Zhang, T. Chen, H. Zeng, J. Zhu, S. Dai and S. Yang, *Adv. Mater.*, 2019, **31**, 1806095.
21 D. Yang, R. Yang, J. Zhang, Z. Yang, S. Liu and C. Li, *Energy Environ. Sci.*, 2015, **8**, 3208–3214.
22 F. Zhang, D. Bi, N. Pellet, C. Xiao, Z. Li, J. J. Berry, S. M. Zakeeruddin, K. Zhu and M. Grätzel, *Energy Environ. Sci.*, 2018, **11**, 3480–3490.
23 F. Zhang, W. Shi, J. Luo, N. Pellet, C. Yi, X. Li, X. Zhao, T. J. S. Dennis, X. Li, S. Wang, Y. Xiao, S. M. Zakeeruddin, D. Bi and M. Grätzel, *Adv. Mater.*, 2017, **29**, 1606806.
24 F. Zhang, C. Xiao, X. Chen, B. W. Larson, S. P. Harvey, J. J. Berry and K. Zhu, *Joule*, 2019, **3**, 1452–1463.
25 C. Xiao, F. Zhang, X. Chen, M. Yang, S. P. Harvey, M. C. Beard, J. J. Berry, C.-S. Jiang, M. M. Al-Jassim and K. Zhu, *ACS Energy Lett.*, 2021, **6**, 650–658.
26 S.-H. Lee, S. Jeong, S. Seo, H. Shin, C. Ma and N.-G. Park, *ACS Energy Lett.*, 2021, **6**, 1612–1621.
27 H. Lu, Y. Liu, P. Ahlawat, A. Mishra, W. R. Tress, F. T. Eickemeyer, Y. Yang, F. Fu, Z. Wang, C. E. Avalos, B. I. Carlsen, A. Agarwalla, X. Zhang, X. Li, Y. Zhan, S. M. Zakeeruddin, L. Emsley, U. Rothlisberger, L. Zheng, A. Hagfeldt and M. Grätzel, *Science*, 2020, **370**, eabb8985.
28 J.-H. Im, C.-R. Lee, J.-W. Lee, S.-W. Park and N.-G. Park, *Nanoscale*, 2011, **3**, 4088–4093.
29 M. M. Lee, J. Teuscher, T. Miyasaka, T. N. Murakami and H. J. Snaith, *Science*, 2012, **338**, 643–647.
30 M. Liu, M. B. Johnston and H. J. Snaith, *Nature*, 2013, **501**, 395–398.
31 H. Zhou, Q. Chen, G. Li, S. Luo, T.-b. Song, H.-S. Duan, Z. Hong, J. You, Y. Liu and Y. Yang, *Science*, 2014, **345**, 542–546.
32 W. S. Yang, J. H. Noh, N. J. Jeon, Y. C. Kim, S. Ryu, J. Seo and S. I. Seok, *Science*, 2015, **348**, 1234–1237.
33 M. Saliba, T. Matsui, J.-Y. Seo, K. Domanski, J.-P. Correa-Baena, M. K. Nazeeruddin, S. M. Zakeeruddin, W. Tress, A. Abate, A. Hagfeldt and M. Grätzel, *Energy Environ. Sci.*, 2016, **9**, 1989–1997.
34 E. H. Jung, N. J. Jeon, E. Y. Park, C. S. Moon, T. J. Shin, T. Y. Yang, J. H. Noh and J. Seo, *Nature*, 2019, **567**, 511–515.
35 Q. Jiang, Y. Zhao, X. Zhang, X. Yang, Y. Chen, Z. Chu, Q. Ye, X. Li, Z. Yin and J. You, *Nat. Photonics*, 2019, **13**, 460–466.
36 J. J. Yoo, G. Seo, M. R. Chua, T. G. Park, Y. Lu, F. Rotermund, Y. K. Kim, C. S. Moon, N. J. Jeon, J. P. Correa-Baena, V. Bulovic, S. S. Shin, M. G. Bawendi and J. Seo, *Nature*, 2021, **590**, 587–593.
37 A. Agresti, S. Pescetelli, L. Cinà, D. Konios, G. Kakavelakis, E. Kymakis and A. D. Carlo, *Adv. Funct. Mater.*, 2016, **26**, 2686–2694.
38 M. M. Byranvand, T. Kim, S. Song, G. Kang, S. U. Ryu and T. Park, *Adv. Energy Mater.*, 2018, **8**, 1870020.

39 T. Duong, Y. Wu, H. Shen, J. Peng, X. Fu, D. Jacobs, E. C. Wang, T. C. Kho, K. C. Fong and M. Stocks, *Adv. Energy Mater.*, 2017, **7**, 1700228.

40 S. Sidhik, A. Cerdan Pasaran, D. Esparza, T. Lopez Luke, R. Carriles and E. De la Rosa, *ACS Appl. Mater. Interfaces*, 2018, **10**, 3571–3580.

41 T. Leijtens, G. E. Eperon, S. Pathak, A. Abate, M. M. Lee and H. J. Snaith, *Nat. Commun.*, 2013, **4**, 2885.

42 J. Liu, Y. Wu, C. Qin, X. Yang, T. Yasuda, A. Islam, K. Zhang, W. Peng, W. Chen and L. Han, *Energy Environ. Sci.*, 2014, **7**, 2963–2967.

43 B. Wang, Q. Wang, Y. M. Wei and Z. P. Li, *Renewable Sustainable Energy Rev.*, 2018, **90**, 187–194.

44 Q. Jiang, L. Zhang, H. Wang, X. Yang, J. Meng, H. Liu, Z. Yin, J. Wu, X. Zhang and J. You, *Nat. Energy*, 2016, **2**, 1–7.

45 C. C. Chueh, C. Z. Li and K. Y. Jen, *Energy Environ. Sci.*, 2015, **8**, 1160–1189.

46 P. Chen, Y. Bai, S. Wang, M. Lyu, J.-H. Yun and L. Wang, *Adv. Funct. Mater.*, 2018, **28**, 1706923.

47 S. S. Shin, S. J. Lee and S. I. Seok, *Adv. Funct. Mater.*, 2019, **29**, 1900455.

48 L. Lin, T. W. Jones, T. C. J. Yang, N. W. Duffy, J. Li, L. Zhao, B. Chi, X. Wang and G. J. Wilson, *Adv. Funct. Mater.*, 2021, **31**, 2008300.

49 J. Han, H. Kwon, E. Kim, D.-W. Kim, H. J. Son and D. H. Kim, *J. Mater. Chem. A*, 2020, **8**, 2105–2113.

50 H. Zhu, Y. Liu, F. T. Eickemeyer, L. Pan, D. Ren, M. A. Ruiz-Preciado, B. Carlsen, B. Yang, X. Dong, Z. Wang, H. Liu, S. Wang, S. M. Zakeeruddin, A. Hagfeldt, M. I. Dar, X. Li and M. Grätzel, *Adv. Mater.*, 2020, **32**, 1907757.

51 M. A. Mahmud, N. K. Elumalai, M. B. Upama, D. Wang, V. R. Gonçales, M. Wright, C. Xu, F. Haque and A. Uddin, *J. Power Sources*, 2018, **383**, 59–71.

52 M. M. Tavakoli, R. Tavakoli, P. Yadav and J. Kong, *J. Mater. Chem. A*, 2019, **7**, 679–686.

53 P. Chen, X. Yin, M. Que, X. Liu and W. Que, *J. Mater. Chem. A*, 2017, **5**, 9641–9648.

54 X. Guo, Z. Lin, J. Ma, Z. Hu, J. Su, C. Zhang, J. Zhang, J. Chang and Y. Hao, *J. Power Sources*, 2019, **438**, 226981.

55 X. Ye, H. Ling, R. Zhang, Z. Wen, S. Hu, T. Akasaka, J. Xia and X. Lu, *J. Power Sources*, 2020, **448**, 227419.

56 F. Zhao, Y. Guo, X. Wang, J. Tao, J. Jiang, Z. Hu and J. Chu, *Sol. Energy*, 2019, **191**, 263–271.

57 C. Chen, Y. Jiang, Y. Wu, J. Guo, X. Kong, X. Wu, Y. Li, D. Zheng, S. Wu and X. Gao, *Sol. RRL*, 2020, **4**, 1900499.

58 K. Wang, Y. Shi, Q. Dong, Y. Li, S. Wang, X. Yu, M. Wu and T. Ma, *J. Phys. Chem. Lett.*, 2015, **6**, 755–759.

59 Y. Guo, T. Liu, N. Wang, Q. Luo, H. Lin, J. Li, Q. Jiang, L. Wu and Z. Guo, *Nano Energy*, 2017, **38**, 193–200.

60 W. Hu, T. Liu, X. Yin, H. Liu, X. Zhao, S. Luo, Y. Guo, Z. Yao, J. Wang and N. Wang, *J. Mater. Chem. A*, 2016, **5**, 1434–1441.

61 Q. Luo, H. Chen, Y. Lin, H. Du, Q. Hou, F. Hao, N. Wang, Z. Guo and J. Huang, *Adv. Funct. Mater.*, 2017, **27**, 1702090.

62 W. Zhu, Q. Zhang, C. Zhang, D. Chen, L. Zhou, Z. Lin, J. Chang, J. Zhang and Y. Hao, *Dalton Trans.*, 2018, **47**, 6404–6411.

63 X. Wang, L.-L. Deng, L.-Y. Wang, S.-M. Dai, Z. Xing, X.-X. Zhan, X.-Z. Lu, S.-Y. Xie, R.-B. Huang and L.-S. Zheng, *J. Mater. Chem. A*, 2017, **5**, 1706–1712.

64 J. Yang, Q. Zhang, J. Xu, H. Liu, R. Qin, H. Zhai, S. Chen and M. Yuan, *Nanomaterials*, 2019, **9**, 1666.

65 J. Dou, Y. Zhang, Q. Wang, A. Abate, Y. Li and M. Wei, *Chem. Commun.*, 2019, **55**, 14673–14676.

66 F. Sadegh, S. Akin, M. Moghadam, V. Mirkhani, M. A. Ruiz-Preciado, Z. Wang, M. M. Tavakoli, M. Graetzel, A. Hagfeldt and W. Tress, *Nano Energy*, 2020, **75**, 105038.

67 C. W. Myung, G. Lee and K. S. Kim, *J. Mater. Chem. A*, 2018, **6**, 23071–23077.

68 J. Chung, S. S. Shin, G. Kim, N. J. Jeon, T.-Y. Yang, J. H. Noh and J. Seo, *Joule*, 2019, **3**, 1977–1985.

69 S. S. Shin, J. H. Suk, B. J. Kang, W. Yin, S. J. Lee, J. H. Noh, T. K. Ahn, F. Rotermund, I. S. Cho and S. I. Seok, *Energy Environ. Sci.*, 2019, **12**, 958–964.

70 A. Bera, K. Wu, A. Sheikh, E. Alarousu, O. F. Mohammed and T. Wu, *J. Phys. Chem. C*, 2014, **118**, 28494–28501.

71 N. Tsvetkov, B. C. Moon, J. Lee and J. K. Kang, *ACS Appl. Energy Mater.*, 2019, **3**, 344–351.

72 K. Mahmood, A. Khalid, S. W. Ahmad, H. G. Qutab, M. Hameed and R. Sharif, *Sol. Energy*, 2020, **203**, 32–36.

73 A. J. Yun, J. Kim, T. Hwang and B. Park, *ACS Appl. Energy Mater.*, 2019, **2**, 3554–3560.

74 C. D. Wessendorf, J. Hanisch, D. Müller and E. Ahlswede, *Sol. RRL*, 2018, **2**, 1800056.

75 W. A. Dunlap-Shohl, R. Younts, B. Gautam, K. Gundogdu and D. B. Mitzi, *J. Phys. Chem. C*, 2016, **120**, 16437–16445.

76 G. Tong, Z. Song, C. Li, Y. Zhao, L. Yu, J. Xu, Y. Jiang, Y. Sheng, Y. Shi and K. Chen, *RSC Adv.*, 2017, **7**, 19457–19463.

77 E. Zhao, L. Gao, S. Yang, L. Wang, J. Cao and T. Ma, *Nano Res.*, 2018, **11**, 5913–5923.

78 D.-B. Li, L. Hu, Y. Xie, G. Niu, T. Liu, Y. Zhou, L. Gao, B. Yang and J. Tang, *ACS Photonics*, 2016, **3**, 2122–2128.

79 H. Wei, J. Wu, P. Qiu, S. Liu, Y. He, M. Peng, D. Li, Q. Meng, F. Zaera and X. Zheng, *J. Mater. Chem. A*, 2019, **7**, 25347–25354.

80 F. Tan, W. Xu, X. Hu, P. Yu and W. Zhang, *Nanoscale Res. Lett.*, 2017, **12**, 614.

81 L. Wang, W. Fu, Z. Gu, C. Fan, X. Yang, H. Li and H. Chen, *J. Mater. Chem. C*, 2014, **2**, 9087–9090.

82 Z. Rao, B. Du, C. Huang, L. Shu, P. Lin, N. Fu and S. Ke, *J. Alloys Compd.*, 2019, **789**, 276–281.

83 W. Ke, G. Fang, Q. Liu, L. Xiong, P. Qin, H. Tao, J. Wang, H. Lei, B. Li and J. Wan, *J. Am. Chem. Soc.*, 2015, **137**, 6730–6733.

84 Y. Li, J. Zhu, Y. Huang, F. Liu, M. Lv, S. Chen, L. Hu, J. Tang, J. Yao and S. Dai, *RSC Adv.*, 2015, **5**, 28424–28429.

85 Q. Jiang, X. Zhang and J. You, *Small*, 2018, **14**, 1801154.

86 W. Ke, D. Zhao, A. J. Cimaroli, C. R. Grice, P. Qin, Q. Liu, L. Xiong, Y. Yan and G. Fang, *J. Mater. Chem. A*, 2015, **3**, 24163–24168.

87 L. Kavan, L. Steier and M. Grätzel, *J. Phys. Chem. C*, 2017, **121**, 342–350.

88 E. J. Yeom, S. S. Shin, W. S. Yang, S. J. Lee, W. Yin, D. Kim, J. H. Noh, T. K. Ahn and S. I. Seok, *J. Mater. Chem. A*, 2017, **5**, 79–86.
89 A. F. Khan, M. Mehmood, M. Aslam and M. Ashraf, *Appl. Surf. Sci.*, 2010, **256**, 2252–2258.
90 S. Lin, B. Yang, X. Qiu, J. Yan, J. Shi, Y. Yuan, W. Tan, X. Liu, H. Huang and Y. Gao, *Org. Electron.*, 2018, **53**, 235–241.
91 X. Qin, Z. Zhao, Y. Wang, J. Wu, Q. Jiang and J. You, *J. Semicond.*, 2017, **38**, 011002.
92 R. M. Pasquarelli, D. S. Ginley and R. O'Hayre, *Chem. Soc. Rev.*, 2011, **40**, 5406–5441.
93 G. Yang, C. Chen, F. Yao, Z. Chen, Q. Zhang, X. Zheng, J. Ma, H. Lei, P. Qin and L. Xiong, *Adv. Mater.*, 2018, **30**, 1706023.
94 L. Zuo, H. Guo, D. W. deQuilettes, S. Jariwala, N. De Marco, S. Dong, R. DeBlock, D. S. Ginger, B. Dunn, M. Wang and Y. Yang, *Sci. Adv.*, 2017, **3**, e1700106.
95 J. Jia, J. Dong, B. Shi, J. Wu, Y. Wu and B. Cao, *ACS Appl. Mater. Interfaces*, 2021, **13**, 2472–2482.
96 A. E. Shalan, E. Akman, F. Sadegh and S. Akin, *J. Phys. Chem. Lett.*, 2021, **12**, 997–1004.
97 H. Bi, X. Zuo, B. Liu, D. He, L. Bai, W. Wang, X. Li, Z. Xiao, K. Sun, Q. Song, Z. Zang and J. Chen, *J. Mater. Chem. A*, 2021, **9**, 3940–3951.
98 P. Hang, J. Xie, C. Kan, B. Li, Y. Zhang, P. Gao, D. Yang and X. Yu, *Adv. Mater.*, 2021, **33**, 2006910.
99 X. Fan, Y. Rui, X. Han, J. Yang, Y. Wang and Q. Zhang, *J. Power Sources*, 2020, **448**, 227405.
100 J. A. Smith, O. S. Game, J. E. Bishop, E. L. K. Spooner, R. C. Kilbride, C. Greenland, R. Jayaprakash, T. I. Alanazi, E. J. Cassella, A. Tejada, G. Chistiakova, M. Wong-Stringer, T. J. Routledge, A. J. Parnell, D. B. Hammond and D. G. Lidzey, *ACS Appl. Energy Mater.*, 2020, **3**, 5552–5562.
101 B. Taheri, E. Calabrò, F. Matteocci, D. Di Girolamo, G. Cardone, A. Liscio, A. Di Carlo and F. Brunetti, *Energy Technol.*, 2020, **8**, 1901284.
102 G. Mathiazhagan, A. Seeber, T. Gengenbach, S. Mastroianni, D. Vak, A. S. R. Chesman, M. Gao, D. Angmo and A. Hinsch, *Sol. RRL*, 2020, **4**, 2000262.
103 T. Bu, J. Li, F. Zheng, W. Chen, X. Wen, Z. Ku, Y. Peng, J. Zhong, Y.-B. Cheng and F. Huang, *Nat. Commun.*, 2018, **9**, 4609.
104 C. Gong, S. Tong, K. Huang, H. Li, H. Huang, J. Zhang and J. Yang, *Sol. RRL*, 2020, **4**, 1900204.
105 X. Chang, J. Fang, Y. Fan, T. Luo, H. Su, Y. Zhang, J. Lu, L. Tsetseris, T. D. Anthopoulos and S. Liu, *Adv. Mater.*, 2020, **32**, 2001243.
106 Y. Peng, F. Zeng, Y. Cheng, C. Wang, K. Huang, P. Xie, H. Xie, Y. Gao and J. Yang, *Org. Electron.*, 2020, **83**, 105736.
107 V. Rohnacher, F. Ullrich, H. Eggers, F. Schackmar, S. Hell, A. Salazar, C. Huck, G. Hernandez-Sosa, U. W. Paetzold, W. Jaegermann and A. Pucci, *Adv. Mater. Technol.*, 2021, **6**, 2000282.
108 Y. Lin, J. Chen, M. M. Tavakoli, Y. Gao, Y. Zhu, D. Zhang, M. Kam, Z. He and Z. Fan, *Adv. Mater.*, 2019, **31**, 1804285.
109 Z. Guo, A. K. Jena, I. Takei, G. M. Kim, M. A. Kamarudin, Y. Sanehira, A. Ishii, Y. Numata, S. Hayase and T. Miyasaka, *J. Am. Chem. Soc.*, 2020, **142**, 9725–9734.
110 Z. Guo, S. Teo, Z. Xu, C. Zhang, Y. Kamata, S. Hayase and T. Ma, *J. Mater. Chem. A*, 2019, **7**, 1227–1232.
111 J. Duan, Q. W. Yue, Q. Xiong, L. Wang, L. Zhu, K. Zhang, J. Zhang and H. Wang, *Appl. Surf. Sci.*, 2019, **470**, 613–621.
112 D. Zhang, H. Tian, S. Bu, T. Yan and Z. Ge, *J. Alloys Compd.*, 2020, **831**, 154717.
113 K. Zhang, J. Duan, F. Liu, J. Zhang and H. Wang, *J. Mater. Sci.*, 2021, **56**, 677–690.
114 Q. Dong, Y. Shi, C. Zhang, Y. Wu and L. Wang, *Nano Energy*, 2017, **40**, 336–344.
115 X. Qiu, B. Yang, H. Chen, G. Liu, Y. Liu, Y. Yuan, H. Huang, H. Xie, D. Niu and Y. Gao, *Org. Electron.*, 2018, **58**, 126–132.
116 H. Tang, Q. Cao, Z. He, S. Wang, J. Han, T. Li, B. Gao, J. Yang, D. Deng and X. Li, *Sol. RRL*, 2020, **4**, 1900415.
117 X. Xu, Z. Xu, J. Tang, X. Zhang, L. Zhang, J. Wu and Z. Lan, *Chem. Eng. J.*, 2018, **351**, 391–398.
118 U. Akpan and B. Hameed, *Appl. Catal., A*, 2010, **375**, 1–11.
119 A. E. Danks, S. R. Hall and Z. Schnepp, *Mater. Horiz.*, 2016, **3**, 91–112.
120 A. Kołodziejczak-Radzimska and T. Jesionowski, *Materials*, 2014, **7**, 2833–2881.
121 W. K. Tan, H. Muto, G. Kawamura, Z. Lockman and A. Matsuda, *Nanomaterials*, 2021, **11**, 181.
122 H. B. Lee, N. Kumar, M. M. Ovhal, Y. J. Kim, Y. M. Song and J. W. Kang, *Adv. Funct. Mater.*, 2020, **30**, 2001559.
123 H. Xu, Z. Hu, Y. Wang, C. Yang, C. Gao, H. Zhang, J. Zhang and Y. Zhu, *Nanotechnology*, 2020, **31**, 315205.
124 P.-H. Lee, T.-T. Wu, K.-Y. Tian, C.-F. Li, C.-H. Hou, J.-J. Shyue, C.-F. Lu, Y.-C. Huang and W.-F. Su, *ACS Appl. Mater. Interfaces*, 2020, **12**, 45936–45949.
125 S. Jeong, S. Seo, H. Park and H. Shin, *Chem. Commun.*, 2019, **55**, 2433–2436.
126 M. Abulikemu, M. Neophytou, J. M. Barbé, M. L. Tietze, A. El Labban, D. H. Anjum, A. Amassian, I. McCulloch and S. Del Gobbo, *J. Mater. Chem. A*, 2017, **5**, 7759–7763.
127 Z. Zhu, Y. Bai, X. Liu, C. C. Chueh, S. Yang and A. K. Y. Jen, *Adv. Mater.*, 2016, **28**, 6478–6484.
128 M. Zhu, W. Liu, W. Ke, S. Clark, E. B. Secor, T.-B. Song, M. G. Kanatzidis, X. Li and M. C. Hersam, *J. Mater. Chem. A*, 2017, **5**, 24110–24115.
129 L. Huang, X. X. Sun, C. Li, J. Xu, R. Xu, Y. Y. Du, J. Ni, H. K. Cai, J. Li, Z. Y. Hu and J. J. Jianjun, *ACS Appl. Mater. Interfaces*, 2017, **9**, 21909–21920.
130 X. Zhang, F. Zabihi, H. Xiong, M. Eslamian and Q. Zhang, *Chem. Eng. J.*, 2020, **394**, 124887.
131 Q. Jiang, Z. Chu, P. Wang, X. Yang, H. Liu, Y. Wang, Z. Yin, J. Wu, X. Zhang and J. You, *Adv. Mater.*, 2017, **29**, 1703852.
132 P. Zhu, S. Gu, X. Luo, Y. Gao, S. Li, J. Zhu and H. Tan, *Adv. Energy Mater.*, 2020, **10**, 1903083.
133 Y. Zhao, L. Zhang, J. Liu, K. Adair, F. Zhao, Y. Sun, T. Wu, X. Bi, K. Amine, J. Lu and X. Sun, *Chem. Soc. Rev.*, 2021, **50**, 3889–3956.
134 Z. Xing, J. Xiao, T. Hu, X. Meng, D. Li, X. Hu and Y. Chen, *Small Methods*, 2020, **4**, 2000588.

135 Y. Lee, S. Lee, G. Seo, S. Paek, K. T. Cho, A. J. Huckaba, M. Calizzi, D. w. Choi, J. S. Park and D. Lee, *Adv. Sci.*, 2018, **5**, 1800130.

136 J. Bing, S. Huang and A. W. Ho-Baillie, *Energy Technol.*, 2020, **8**, 1901114.

137 Y. Gu, C. Ye, X. Yin, J. Han, H. Shen, J. Li, X. Hao and H. Lin, *Chem. Eng. J.*, 2018, **351**, 791–798.

138 Y. Zhou, X. Li and H. Lin, *Small*, 2020, **16**, 1902579.

139 M. J. Jeong, K. M. Yeom, S. J. Kim, E. H. Jung and J. H. Noh, *Energy Environ. Sci.*, 2021, **14**, 2419–2428.

140 Y. Ko, Y. Kim, C. Lee, T. Kim, S. Kim, Y. J. Yun, H. j. Gwon, N. H. Lee and Y. Jun, *ChemSusChem*, 2020, **13**, 4051–4063.

141 L. Xiong, Y. Guo, J. Wen, H. Liu, G. Yang, P. Qin and G. Fang, *Adv. Funct. Mater.*, 2018, **28**, 1802757.

142 J. J. Ma, X. L. Zheng, H. W. Lei, W. J. Ke, C. Chen, Z. L. Chen, G. Yang and G. J. Fang, *Sol. RRL*, 2017, **1**, 1700118.

143 Z. Song, W. Bi, X. Zhuang, Y. Wu, B. Zhang, X. Chen, C. Chen, Q. Dai and H. Song, *Sol. RRL*, 2020, **4**, 1900266.

144 J. Li, L. Li, W. Chen, Q. Yi and G. Zou, *Nanotechnology*, 2020, **32**, 025606.

145 E. Aydin, J. Troughton, M. De Bastiani, E. Ugur, M. Sajjad, A. Alzahrani, M. Neophytou, U. Schwingenschlögl, F. Laquai and D. Baran, *ACS Appl. Energy Mater.*, 2018, **1**, 6227–6233.

146 M. K. Otoufi, M. Ranjbar, A. Kermanpur, N. Taghavinia, M. Minbashi, M. Forouzandeh and F. Ebadi, *Sol. Energy*, 2020, **208**, 697–707.

147 Y. Mo, J. Shi, P. Zhou, S. Li, T. Bu, Y.-B. Cheng and F. Huang, *Sol. RRL*, 2019, **3**, 1900209.

148 L. Qiu, Z. Liu, L. K. Ono, Y. Jiang, D. Y. Son, Z. Hawash, S. He and Y. Qi, *Adv. Funct. Mater.*, 2019, **29**, 1806779.

149 G. Bai, Z. Wu, J. Li, T. Bu, W. Li, W. Li, F. Huang, Q. Zhang, Y.-B. Cheng and J. Zhong, *Sol. Energy*, 2019, **183**, 306–314.

150 J.-Y. Chen, C.-C. Chueh, Z. Zhu, W.-C. Chen and A. K.-Y. Jen, *Sol. Energy Mater. Sol. Cells*, 2017, **164**, 47–55.

151 Y. S. Seo, E.-Y. Ahn, J. Park, T. Y. Kim, J. E. Hong, K. Kim, Y. Park and Y. Park, *Nanoscale Res. Lett.*, 2017, **12**, 7.

152 M.-G. Kim, M. G. Kanatzidis, A. Facchetti and T. J. Marks, *Nat. Mater.*, 2011, **10**, 382–388.

153 X. Liu, K. W. Tsai, Z. Zhu, Y. Sun, C. C. Chueh and A. K. Y. Jen, *Adv. Mater. Interfaces*, 2016, **3**, 1600122.

154 L. Mai, D. Zanders, E. Subasi, E. Ciftyurek, C. Hoppe, D. Rogalla, W. Gilbert, T. L. Arcos, K. Schierbaum, G. Grundmeier, C. Bock and A. Devi, *ACS Appl. Mater. Interfaces*, 2019, **11**, 3169–3180.

155 C. Wang, L. Guan, D. Zhao, Y. Yu, C. R. Grice, Z. Song, R. A. Awni, J. Chen, J. Wang and X. Zhao, *ACS Energy Lett.*, 2017, **2**, 2118–2124.

156 C. Wang, C. Xiao, Y. Yu, D. Zhao, R. A. Awni, C. R. Grice, K. Ghimire, I. Constantinou, W. Liao and A. J. Cimaroli, *Adv. Energy Mater.*, 2017, **7**, 1700414.

157 C. Wang, D. Zhao, C. R. Grice, W. Liao, Y. Yu, A. Cimaroli, N. Shrestha, P. J. Roland, J. Chen and Z. Yu, *J. Mater. Chem. A*, 2016, **4**, 12080–12087.

158 M. Singh, A. Ng, Z. Ren, H. Hu, H.-C. Lin, C.-W. Chu and G. Li, *Nano Energy*, 2019, **60**, 275–284.

159 M. F. M. Noh, N. A. Arzaee, J. Safaei, N. A. Mohamed, H. P. Kim, J. Jang and M. A. M. Teridi, *J. Alloys Compd.*, 2019, **773**, 997–1008.

160 H. Sun, Y. Zhou, Y. Xin, K. Deng, L. Meng, J. Xiong and L. Li, *Adv. Funct. Mater.*, 2019, **29**, 1808667.

161 Y. Guo, X. Yin, J. Liu, W. Chen, S. Wen, M. Que, H. Xie, Y. Yang, W. Que and B. Gao, *Org. Electron.*, 2019, **65**, 207–214.

162 X. Zhang, Y. Rui, Y. Wang, J. Xu, H. Wang, Q. Zhang and P. Müller-Buschbaum, *J. Power Sources*, 2018, **402**, 460–467.

163 K. Mahmood, A. Khalid, F. Nawaz and M. T. Mehran, *J. Colloid Interface Sci.*, 2018, **532**, 387–394.

164 Z. Chen, G. Yang, X. Zheng, H. Lei, C. Chen, J. Ma, H. Wang and G. Fang, *J. Power Sources*, 2017, **351**, 123–129.

165 J. Jia, J. Dong, J. Wu, H. Wei and B. Cao, *J. Alloys Compd.*, 2020, **844**, 156032.

166 Y. Zhao, J. Zhu, B. He and Q. Tang, *ACS Appl. Mater. Interfaces*, 2021, **13**, 11058–11066.

167 G. S. Han, H. S. Chung, D. H. Kim, B. J. Kim, J.-W. Lee, N.-G. Park, I. S. Cho, J.-K. Lee, S. Lee and H. S. Jung, *Nanoscale*, 2015, **7**, 15284–15290.

168 S. S. Mali, J. V. Patil, H. Kim and C. K. Hong, *Nanoscale*, 2018, **10**, 8275–8284.

169 Y. Lv, P. Wang, B. Cai, Q. Ma, X. Zheng, Y. Wu, Q. Jiang, J. Liu and W. H. Zhang, *Sol. RRL*, 2018, **2**, 1800133.

170 Y. E. Kim, U. C. Baek, J. H. Kim, W. S. Chi and J. T. Park, *Mater. Chem. Phys.*, 2020, **254**, 123538.

171 P. Zhou, J. Wu, Y. Tu, M. Zhen, J. Huo, Y. Wei and Z. Lan, *Sol. Energy*, 2016, **137**, 579–584.

172 K. Deng, H. Lu, Z. Shi, Q. Liu and L. Li, *ACS Appl. Mater. Interfaces*, 2013, **5**, 7845–7851.

173 S. Gubbala, V. Chakrapani, V. Kumar and M. K. Sunkara, *Adv. Funct. Mater.*, 2008, **18**, 2411–2418.

174 Z. Li, Y. Zhou, W. Mao and Z. Zou, *J. Power Sources*, 2015, **274**, 575–581.

175 I. J. Park, S. Park, D. H. Kim, H. Jeong and S. Lee, *Mater. Lett.*, 2017, **202**, 48–51.

176 X. Hou, Y. Hu, H. Jiang, J. Huo, Y. Li and C. Li, *J. Mater. Chem. A*, 2013, **1**, 13814–13820.

177 A. Ashok, G. Gopakumar, S. Vijayaraghavan, S. V. Nair and M. Shanmugam, *IEEE J. Photovolt.*, 2018, **8**, 1044–1050.

178 Q. Wali, Z. H. Bakr, N. A. Manshor, A. Fakharuddin and R. Jose, *Sol. Energy*, 2016, **132**, 395–404.

179 Y.-F. Wang, K.-N. Li, W.-Q. Wu, Y.-F. Xu, H.-Y. Chen, C.-Y. Su and D.-B. Kuang, *RSC Adv.*, 2013, **3**, 13804–13810.

180 P. Chen, X. Yin, M. Que, Y. Yang and W. Que, *RSC Adv.*, 2016, **6**, 57996–58002.

181 A. Fakharuddin, F. Di Giacomo, A. L. Palma, F. Matteocci, I. Ahmed, S. Razza, A. D'Epifanio, S. Licoccia, J. Ismail, A. Di Carlo, T. M. Brown and R. Jose, *ACS Nano*, 2015, **9**, 8420–8429.

182 K. Mahmood, B. S. Swain and A. Amassian, *Adv. Energy Mater.*, 2015, **5**, 1500568.

183 P. Ruankham, D. Wongratanaphisan, A. Gardchareon, S. Phadungdhitidhada, S. Choopun and T. Sagawa, *Appl. Surf. Sci.*, 2017, **410**, 393–400.

184 C. Liu, R. Zhu, A. Ng, Z. Ren, S. H. Cheung, L. Du, S. K. So, J. A. Zapien, A. B. Djurišić and D. L. Phillips, *J. Mater. Chem. A*, 2017, **5**, 15970–15980.
185 U. V. Desai, C. Xu, J. Wu and D. Gao, *J. Phys. Chem. C*, 2013, **117**, 3232–3239.
186 D. J. Kim, S. H. Ahn, C. S. Lee and J. H. Kim, *J. Mater. Chem. A*, 2015, **3**, 17644–17651.
187 H. J. Snaith and C. Ducati, *Nano Lett.*, 2010, **10**, 1259–1265.
188 P. Tiwana, P. Docampo, M. B. Johnston, H. J. Snaith and L. M. Herz, *ACS Nano*, 2011, **5**, 5158–5166.
189 C. Gao, S. Yuan, B. Cao and J. Yu, *Chem. Eng. J.*, 2017, **325**, 378–385.
190 Q. Liu, M. C. Qin, W. J. Ke, X. L. Zheng, Z. Chen, P. L. Qin, L. B. Xiong, H. W. Lei, J. W. Wan and J. Wen, *Adv. Funct. Mater.*, 2016, **26**, 6069–6075.
191 W. Q. Wu, D. Chen, Y. B. Cheng and R. A. Caruso, *Sol. RRL*, 2017, **1**, 1700117.
192 G. Yang, H. W. Lei, H. Tao, X. L. Zheng, J. J. Ma, Q. Liu, W. J. Ke, Z. L. Chen, L. B. Xiong, P. L. Qin, Z. Chen, M. C. Qin, X. H. Lu, Y. F. Yan and G. J. Fang, *Small*, 2017, **13**, 1601769.
193 H. Liu, Z. Chen, H. Wang, F. Ye, J. Ma, X. Zheng, P. Gui, L. Xiong, J. Wen and G. Fang, *J. Mater. Chem. A*, 2019, **7**, 10636–10643.
194 S. Y. Park, M. Y. Baek, Y. Ju, D. H. Kim, C. S. Moon, J. H. Noh and H. S. Jung, *J. Phys. Chem. Lett.*, 2018, **9**, 5460–5467.
195 E. Wang, P. Chen, X. Yin, Y. Wu and W. Que, *Sol. RRL*, 2019, **3**, 1900041.
196 L. Xiong, M. Qin, C. Chen, J. Wen, G. Yang, Y. Guo, J. Ma, Q. Zhang, P. Qin and S. Li, *Adv. Funct. Mater.*, 2018, **28**, 1706276.
197 Y. Zhao, J. Duan, H. Yuan, Y. Wang, X. Yang, B. He and Q. Tang, *Sol. RRL*, 2019, **3**, 1800284.
198 S. Vijayaraghavan, J. Wall, L. Li, G. Xing, Q. Zhang and F. Yan, *Mater. Today Phys.*, 2020, **13**, 100204.
199 Z. Wang, T. Wu, L. Xiao, P. Qin, X. Yu, L. Ma, L. Xiong, H. Li, X. Chen and Z. Wang, *J. Power Sources*, 2021, **488**, 229451.
200 Q. Jiang, L. Wang, C. Yan, C. Liu, Z. Guo and N. Wang, *Eng. Sci.*, 2018, **1**, 64–68.
201 J. Chen, H. Dong, L. Zhang, J. Li, F. Jia, B. Jiao, J. Xu, X. Hou, J. Liu and Z. Wu, *J. Mater. Chem. A*, 2020, **8**, 2644–2653.
202 L. S. Huang, X. W. Zhou, R. Xue, P. F. Xu, S. L. Wang, C. Xu, W. Zeng, Y. Xiong, H. Q. Sang and D. Liang, *Nano-Micro Lett.*, 2020, 12.
203 H. H. Niu, C. L. Fang, X. T. Wei, H. Wang, L. Wan, Y. Li, X. L. Mao, J. Z. Xu and R. Zhou, *Dalton Trans.*, 2021, **50**, 6477–6487.
204 J. Duan, Q. Xiong, B. Feng, Y. Xu, J. Zhang and H. Wang, *Appl. Surf. Sci.*, 2017, **391**, 677–683.
205 W. Gong, H. Guo, H. Zhang, J. Yang, H. Chen, L. Wang, F. Hao and X. Niu, *J. Mater. Chem. C*, 2020, **8**, 11638–11646.
206 J. Liang, Z. Chen, G. Yang, H. Wang, F. Ye, C. Tao and G. Fang, *ACS Appl. Mater. Interfaces*, 2019, **11**, 23152–23159.
207 X. Gong, Q. Sun, S. Liu, P. Liao, Y. Shen, C. Grätzel, S. M. Zakeeruddin, M. Grätzel and M. Wang, *Nano Lett.*, 2018, **18**, 3969–3977.
208 Q. Jiang, F. Liu, T. Li and T. Xu, *J. Mater. Chem. C*, 2014, **2**, 618–621.
209 J. Zhuang, P. Mao, Y. Luan, N. Chen, X. Cao, G. Niu, F. Jia, F. Wang, S. Cao and J. Wang, *Adv. Funct. Mater.*, 2021, 2010385.
210 I. Mondal, G. Bahuguna, M. K. Ganesha, M. Verma, R. Gupta, A. K. Singh and G. U. Kulkarni, *ACS Appl. Mater. Interfaces*, 2020, **12**, 54203–54211.
211 E. P. Nascimento, H. C. Firmino, A. M. Santos, H. B. Sales, V. D. Silva, D. A. Macedo, G. A. Neves, E. S. Medeiros and R. R. Menezes, *J. Am. Ceram. Soc.*, 2021, **104**, 1297–1308.
212 W. Ahmad, D. Liu, J. Wu, W. Ahmad, Y. Wang, P. Zhang, T. Zhang, H. Zheng, L. Chen, Z. D. Chen and S. Li, *IEEE J. Photovolt.*, 2019, **9**, 1273–1279.
213 Y. Huang, S. Li, C. Wu, S. Wang, C. Wang and R. Ma, *Chem. Phys. Lett.*, 2020, **745**, 137220.
214 Y. Qiang, Y. Xie, Y. Qi, P. Wei, H. Shi, C. Geng and H. Liu, *Sol. Energy*, 2020, **201**, 523–529.
215 N. Zhou, Q. Cheng, L. Li and H. Zhou, *J. Phys. D: Appl. Phys.*, 2018, **51**, 394001.
216 L. Xiong, M. Qin, G. Yang, Y. Guo, H. Lei, Q. Liu, W. Ke, H. Tao, P. Qin and S. Li, *J. Mater. Chem. A*, 2016, **4**, 8374–8383.
217 H. Chen, D. Liu, Y. Wang, C. Wang, T. Zhang, P. Zhang, H. Sarvari, Z. Chen and S. Li, *Nanoscale Res. Lett.*, 2017, **12**, 1–6.
218 P. Sakthivel, S. Foo, M. Thambidurai, P. Harikesh, N. Mathews, R. Yuvakkumar, G. Ravi and C. Dang, *J. Power Sources*, 2020, **471**, 228443.
219 H. Ye, Z. Liu, X. Liu, B. Sun, X. Tan, Y. Tu, T. Shi, Z. Tang and G. Liao, *Appl. Surf. Sci.*, 2019, **478**, 417–425.
220 Y. Bai, Y. Fang, Y. Deng, Q. Wang, J. Zhao, X. Zheng, Y. Zhang and J. Huang, *ChemSusChem*, 2016, **9**, 2686–2691.
221 Q. Cao, Z. Li, J. Han, S. Wang, J. Zhu, H. Tang, X. Li and X. Li, *Sol. RRL*, 2019, **3**, 1900333.
222 J. Bahadur, A. H. Ghahremani, B. Martin, T. Druffel, M. K. Sunkara and K. Pal, *Org. Electron.*, 2019, **67**, 159–167.
223 S. Akin, *ACS Appl. Mater. Interfaces*, 2019, **11**, 39998–40005.
224 Z. Ma, W. Zhou, Z. Xiao, H. Zhang, Z. Li, J. Zhuang, C. Peng and Y. Huang, *Org. Electron.*, 2019, **71**, 98–105.
225 B. Roose and R. H. Friend, *Adv. Mater. Interfaces*, 2019, **6**, 1801788.
226 Y. W. Noh, J. H. Lee, I. S. Jin, S. H. Park and J. W. Jung, *Nano Energy*, 2019, **65**, 104014.
227 X. Zhang, X. Liu, H. Ning, W. Yuan, Y. Deng, X. Zhang, S. Wang, J. Wang, R. Yao and J. Peng, *Superlattices Microstruct.*, 2018, **123**, 330–337.
228 E. Halvani Anaraki, A. Kermanpur, M. T. Mayer, L. Steier, T. Ahmed, S.-H. Turren-Cruz, J. Seo, J. Luo, S. M. Zakeeruddin, W. R. Tress, T. Edvinsson, M. Grätzel, A. Hagfeldt and J.-P. Correa-Baena, *ACS Energy Lett.*, 2018, **3**, 773–778.
229 X. Ren, D. Yang, Z. Yang, J. Feng, X. Zhu, J. Niu, Y. Liu, W. Zhao and S. F. Liu, *ACS Appl. Mater. Interfaces*, 2017, **9**, 2421–2429.
230 S. Wang, W. Shen, J. Liu, T. Ouyang, Y. Wu, W. Li, M. Chen, P. Qi, Y. Lu and Y. Tang, *Nanotechnology*, 2021, **32**, 145403.

231 Q. Liu, X. Zhang, C. Li, H. Lu, Z. Weng, Y. Pan, W. Chen, X.-C. Hang, Z. Sun and Y. Zhan, *Appl. Phys. Lett.*, 2019, **115**, 143903.

232 J. Song, W. Zhang, D. Wang, K. Deng, J. Wu and Z. Lan, *Sol. Energy*, 2019, **185**, 508–515.

233 Z. Xu, S. H. Teo, L. Gao, Z. Guo, Y. Kamata, S. Hayase and T. Ma, *Org. Electron.*, 2019, **73**, 62–68.

234 J. Tian, J. Zhang, X. Li, B. Cheng, J. Yu and W. Ho, *Sol. RRL*, 2020, **4**, 2000090.

235 M. Hu, L. Zhang, S. She, J. Wu, X. Zhou, X. Li, D. Wang, J. Miao, G. Mi and H. Chen, *Sol. RRL*, 2020, **4**, 1900331.

236 N. Li, J. Yan, Y. Ai, E. Jiang, L. Lin, C. Shou, B. Yan, J. Sheng and J. Ye, *Sci. China Mater.*, 2020, **63**, 207–215.

237 J. Dagar, S. Castro-Hermosa, G. Lucarelli, A. Zampetti, F. Cacialli and T. M. Brown, *IEEE J. Photovolt.*, 2019, **9**, 1309–1315.

238 H. Dong, S. Pang, Y. Xu, Z. Li, Z. Zhang, W. Zhu, D. Chen, H. Xi, Z. Lin and J. Zhang, *ACS Appl. Mater. Interfaces*, 2020, **12**, 54703–54710.

239 Y. W. Noh, I. S. Jin, K. S. Kim, S. H. Park and J. W. Jung, *J. Mater. Chem. A*, 2020, **8**, 17163–17173.

240 D. Wang, C. Wu, W. Luo, X. Guo, B. Qu, L. Xiao and Z. Chen, *ACS Appl. Energy Mater.*, 2018, **1**, 2215–2221.

241 Y. Yang, T. Wang, Y. Zhang, X. Zhang, N. Li, P. Wang, Y. Qian, Q. Rong, L. Shui and G. Zhou, *Sol. Energy*, 2020, **196**, 22–26.

242 H. Yi, D. Wang, M. A. Mahmud, F. Haque, M. B. Upama, C. Xu, L. Duan and A. Uddin, *ACS Appl. Energy Mater.*, 2018, **1**, 6027–6039.

243 F. Guo, X. Sun, B. Liu, Z. Yang, J. Wei and D. Xu, *Angew. Chem., Int. Ed.*, 2019, **58**, 18460–18465.

244 S. S. Mali, J. V. Patil, H. Arandiyan and C. K. Hong, *J. Mater. Chem. A*, 2019, **7**, 17516–17528.

245 P. Wang, R. Li, B. Chen, F. Hou, J. Zhang, Y. Zhao and X. Zhang, *Adv. Mater.*, 2020, **32**, 1905766.

246 F. Wang, Y. Zhang, M. Yang, J. Du, L. Xue, L. Yang, L. Fan, Y. Sui, J. Yang and X. Zhang, *Nano Energy*, 2019, **63**, 103825.

247 J. Ye, Y. Li, A. A. Medjahed, S. Pouget, D. Aldakov, Y. Liu and P. Reiss, *Small*, 2021, **17**, 2005671.

248 W. Chen, Y. Wu, Y. Yue, J. Liu, W. Zhang, X. Yang, H. Chen, E. Bi, I. Ashraful and M. Grätzel, *Science*, 2015, **350**, 944–948.

249 Y. Hou, X. Du, S. Scheiner, D. P. McMeekin, Z. Wang, N. Li, M. S. Killian, H. Chen, M. Richter and I. Levchuk, *Science*, 2017, **358**, 1192–1197.

250 O. Malinkiewicz, A. Yella, Y. H. Lee, G. M. Espallargas, M. Graetzel, M. K. Nazeeruddin and H. J. Bolink, *Nat. Photonics*, 2014, **8**, 128–132.

251 Y. Shao, Z. Xiao, C. Bi, Y. Yuan and J. Huang, *Nat. Commun.*, 2014, **5**, 1–7.

252 F. Xie, C.-C. Chen, Y. Wu, X. Li, M. Cai, X. Liu, X. Yang and L. Han, *Energy Environ. Sci.*, 2017, **10**, 1942–1949.

253 X. Zheng, B. Chen, J. Dai, Y. Fang, Y. Bai, Y. Lin, H. Wei, X. C. Zeng and J. Huang, *Nat. Energy*, 2017, **2**, 1–9.

254 W. Ke, D. Zhao, C. Xiao, C. Wang, A. J. Cimaroli, C. R. Grice, M. Yang, Z. Li, C.-S. Jiang, M. Al-Jassim, K. Zhu, M. G. Kanatzidis, G. Fang and Y. Yan, *J. Mater. Chem. A*, 2016, **4**, 14276–14283.

255 K. Liu, S. Chen, J. Wu, H. Zhang, M. Qin, X. Lu, Y. Tu, Q. Meng and X. Zhan, *Energy Environ. Sci.*, 2018, **11**, 3463–3471.

256 J. Wang, K. Datta, C. H. Weijtens, M. M. Wienk and R. A. Janssen, *Adv. Funct. Mater.*, 2019, **29**, 1905883.

257 K. Liu, S. Chen, J. Wu, H. Zhang, M. Qin, X. Lu, Y. Tu, Q. Meng and X. Zhan, *Energy Environ. Sci.*, 2018, **11**, 3463–3471.

258 C. Tian, K. Lin, J. Lu, W. Feng, P. Song, L. Xie and Z. Wei, *Small Methods*, 2020, **4**, 1900476.

259 J. A. Raiford, C. C. Boyd, A. F. Palmstrom, E. J. Wolf, B. A. Fearon, J. J. Berry, M. D. McGehee and S. F. Bent, *Adv. Energy Mater.*, 2019, **9**, 1902353.

260 A. F. Palmstrom, J. A. Raiford, R. Prasanna, K. A. Bush, M. Sponseller, R. Cheacharoen, M. C. Minichetti, D. S. Bergsman, T. Leijtens and H. P. Wang, *Adv. Energy Mater.*, 2018, **8**, 1800591.

261 R. Cheacharoen, N. Rolston, D. Harwood, K. A. Bush, R. H. Dauskardt and M. D. McGehee, *Energy Environ. Sci.*, 2018, **11**, 144–150.

262 N. Rolston, B. L. Watson, C. D. Bailie, M. D. McGehee, J. P. Bastos, R. Gehlhaar, J.-E. Kim, D. Vak, A. T. Mallajosyula and G. Gupta, *Extreme Mech. Lett.*, 2016, **9**, 353–358.

263 J. Liu, Y. Guo, M. Zhu, Y. Li and X. Li, *J. Power Sources*, 2020, **476**, 228648.

264 Q. Luo, H. Ma, F. Hao, Q. Hou, J. Ren, L. Wu, Z. Yao, Y. Zhou, N. Wang, K. Jiang, H. Lin and Z. Guo, *Adv. Funct. Mater.*, 2017, **27**, 1703068.

265 Y. Wang, C. Duan, J. Li, W. Han, M. Zhao, L. Yao, Y. Wang, C. Yan and T. Jiu, *ACS Appl. Mater. Interfaces*, 2018, **10**, 20128–20135.

266 P. Fabiola Mendez, S. K. M. Muhammed, E. M. Barea, S. Masi and I. Mora-Sero, *Sol. RRL*, 2019, **3**, 1900191.

267 K. Jung, J. Kim, S. Ko, J. W. Choi, K. C. Kim, S.-G. Lee and M.-J. Lee, *J. Mater. Sci. Technol.*, 2020, **59**, 195–202.

268 F. Li, M. Xu, X. Ma, L. Shen, L. Zhu, Y. Weng, G. Yue, F. Tan and C. Chen, *Nanoscale Res. Lett.*, 2018, **13**, 1–7.

269 J. Xie, K. Huang, X. Yu, Z. Yang, K. Xiao, Y. Qiang, X. Zhu, L. Xu, P. Wang, C. Cui and D. Yang, *ACS Nano*, 2017, **11**, 9176–9182.

270 Y. Ai, W. Liu, C. Shou, J. Yan, N. Li, Z. Yang, W. Song, B. Yan, J. Sheng and J. Ye, *Sol. Energy*, 2019, **194**, 541–547.

271 Z. Liu, K. Deng, J. Hu and L. Li, *Angew. Chem., Int. Ed.*, 2019, **58**, 11497–11504.

272 E. H. Jung, B. Chen, K. Bertens, M. Vafaie, S. Teale, A. Proppe, Y. Hou, T. Zhu, C. Zheng and E. H. Sargent, *ACS Energy Lett.*, 2020, **5**, 2796–2801.

273 C. Huang, P. Lin, N. Fu, K. Sun, M. Ye, C. Liu, X. Zhou, L. Shu, X. Hao, B. Xu, X. Zeng, Y. Wang and S. Ke, *J. Mater. Chem. A*, 2018, **6**, 22086–22095.

274 D. Yang, R. Yang, K. Wang, C. Wu, X. Zhu, J. Feng, X. Ren, G. Fang, S. Priya and S. F. Liu, *Nat. Commun.*, 2018, **9**, 1–11.

275 Z. Zhang, J. Zhang, N. Chen and L. Qu, *Energy Environ. Sci.*, 2012, **5**, 8869–8890.

276 J. Chen, H. Dong, L. Zhang, J. Li, F. Jia, B. Jiao, J. Xu, X. Hou, J. Liu and Z. Wu, *J. Mater. Chem. A*, 2020, **8**, 2644–2653.
277 W. Hui, Y. Yang, Q. Xu, H. Gu, S. Feng, Z. Su, M. Zhang, J. Wang, X. Li and J. Fang, *Adv. Mater.*, 2020, **32**, 1906374.
278 J. Jia, C. Qian, Y. Dong, Y. F. Li, H. Wang, M. Ghoussoub, K. T. Butler, A. Walsh and G. A. Ozin, *Chem. Soc. Rev.*, 2017, **46**, 4631–4644.
279 S. Y. Abate, D.-C. Huang and Y.-T. Tao, *Org. Electron.*, 2020, **78**, 105583.
280 F. Ali, C. Roldán-Carmona, M. Sohail and M. K. Nazeeruddin, *Adv. Energy Mater.*, 2020, **10**, 2002989.
281 F. Han, G. Hao, Z. Wan, J. Luo, J. Xia and C. Jia, *Electrochim. Acta*, 2019, **296**, 75–81.
282 S. Y. Kim, S. J. Cho, S. E. Byeon, X. He and H. J. Yoon, *Adv. Energy Mater.*, 2020, **10**, 2002606.
283 G. Yang, C. Wang, H. Lei, X. Zheng, P. Qin, L. Xiong, X. Zhao, Y. Yan and G. Fang, *J. Mater. Chem. A*, 2017, **5**, 1658–1666.
284 J. Yan, Z. Lin, Q. Cai, X. Wen and C. Mu, *ACS Appl. Energy Mater.*, 2020, **3**, 3504–3511.
285 G.-W. Kim, Y. Choi, H. Choi, J. Min, T. Park and S. Song, *J. Mater. Chem. A*, 2020, **8**, 21721–21728.
286 H. Anizelli, T. W. David, P. Tyagi, E. Laureto and J. Kettle, *Sol. Energy*, 2020, **203**, 157–163.
287 G. Tumen-Ulzii, T. Matsushima, D. Klotz, M. R. Leyden, P. Wang, C. Qin, J.-W. Lee, S.-J. Lee, Y. Yang and C. Adachi, *Communications Materials*, 2020, **1**, 1–7.
288 P. Huang, Q. Chen, K. Zhang, L. Yuan, Y. Zhou, B. Song and Y. Li, *J. Mater. Chem. A*, 2019, **7**, 6213–6219.
289 W. Wang, Z. Su, B. Sun, L. Tao, H. Gu, W. Hui, Q. Wei, W. Shi, X. Gao and Y. Xia, *Adv. Mater. Interfaces*, 2021, **8**, 2001683.
290 Y. Wang, P. Xiang, A. Ren, H. Lai, Z. Zhang, Z. Xuan, Z. Wan, J. Zhang, X. Hao and L. Wu, *ACS Appl. Mater. Interfaces*, 2020, **12**, 53973–53983.
291 L. Yang, Y. Dall'Agnese, K. Hantanasirisakul, C. E. Shuck, K. Maleski, M. Alhabeb, G. Chen, Y. Gao, Y. Sanehira and A. K. Jena, *J. Mater. Chem. A*, 2019, **7**, 5635–5642.
292 K. Hantanasirisakul and Y. Gogotsi, *Adv. Mater.*, 2018, **30**, 1804779.
293 M. Naguib, M. Kurtoglu, V. Presser, J. Lu, J. J. Niu, M. Heon, L. Hultman, Y. Gogotsi and M. W. Barsoum, *Adv. Mater.*, 2011, **23**, 4248–4253.
294 H. Xu, A. B. Ren, J. Wu and Z. M. Wang, *Adv. Funct. Mater.*, 2020, **30**, 2000907.
295 A. Agresti, A. Pazniak, S. Pescetelli, A. Di Vito, D. Rossi, A. Pecchia, M. Auf der Maur, A. Liedl, R. Larciprete, D. V. Kuznetsov, D. Saranin and A. Di Carlo, *Nat. Mater.*, 2019, **18**, 1228–1234.
296 Z. Guo, L. Gao, Z. Xu, S. Teo, C. Zhang, Y. Kamata, S. Hayase and T. Ma, *Small*, 2018, **14**, e1802738.
297 X. Liu, P. Li, Y. Zhang, X. Hu, Y. Duan, F. Li, D. Li, G. Shao and Y. Song, *J. Power Sources*, 2019, **413**, 459–466.
298 X. Meng, X. Cui, M. Rager, S. Zhang, Z. Wang, J. Yu, Y. W. Harn, Z. Kang, B. K. Wagner and Y. Liu, *Nano Energy*, 2018, **52**, 123–133.
299 F. Zhang, X. Yang, M. Cheng, J. Li, W. Wang, H. Wang and L. Sun, *J. Mater. Chem. A*, 2015, **3**, 24272–24280.
300 Q. Guo, F. Yuan, B. Zhang, S. Zhou, J. Zhang, Y. Bai, L. Fan, T. Hayat, A. Alsaedi and Z. a. Tan, *Nanoscale*, 2019, **11**, 115–124.
301 I. Jeon, A. Shawky, S. Seo, Y. Qian, A. Anisimov, E. I. Kauppinen, Y. Matsuo and S. Maruyama, *J. Mater. Chem. A*, 2020, **8**, 11141–11147.
302 Z. Li, C. Liu, G. Ren, W. Han, L. Shen and W. Guo, *Sol. RRL*, 2020, **4**, 1900369.
303 Q. Luo, H. Ma, Q. Hou, Y. Li, J. Ren, X. Dai, Z. Yao, Y. Zhou, L. Xiang and H. Du, *Adv. Funct. Mater.*, 2018, **28**, 1706777.
304 A. Mei, X. Li, L. Liu, Z. Ku, T. Liu, Y. Rong, M. Xu, M. Hu, J. Chen, Y. Yang, M. Gratzel and H. Han, *Science*, 2014, **345**, 295–298.
305 M. Paszkiewicz-Gawron, E. Kowalska, M. Endo-Kimura, J. Zwara, A. Pancielejko, K. Wang, W. Lisowski, J. Łuczak, A. Zaleska-Medynska and E. Grabowska-Musiał, *Appl. Surf. Sci.*, 2021, **541**, 148425.
306 S. Wang, Y. Zhu, B. Liu, C. Wang and R. Ma, *J. Mater. Chem. A*, 2019, **7**, 5353–5362.
307 S. Zhang, H. Si, W. Fan, M. Shi, M. Li, C. Xu, Z. Zhang, Q. Liao, A. Sattar and Z. Kang, *Angew. Chem., Int. Ed.*, 2020, **59**, 11573–11582.
308 X. Zhao, L. Tao, H. Li, W. Huang, P. Sun, J. Liu, S. Liu, Q. Sun, Z. Cui, L. Sun, Y. Shen, Y. Yang and M. Wang, *Nano Lett.*, 2018, **18**, 2442–2449.
309 A. F. Castro-Méndez, J. Hidalgo and J. P. Correa-Baena, *Adv. Energy Mater.*, 2019, **9**, 1901489.
310 B. Chen, M. Yang, S. Priya and K. Zhu, *J. Phys. Chem. Lett.*, 2016, **7**, 905–917.
311 H.-W. Chen, N. Sakai, M. Ikegami and T. Miyasaka, *J. Phys. Chem. Lett.*, 2015, **6**, 164–169.
312 J. Wei, Y. Zhao, H. Li, G. Li, J. Pan, D. Xu, Q. Zhao and D. Yu, *J. Phys. Chem. Lett.*, 2014, **5**, 3937–3945.
313 P. Calado, A. M. Telford, D. Bryant, X. Li, J. Nelson, B. C. O'Regan and P. R. F. Barnes, *Nat. Commun.*, 2016, **7**, 13831.
314 Z. Li, C. Xiao, Y. Yang, S. P. Harvey, D. H. Kim, J. A. Christians, M. Yang, P. Schulz, S. U. Nanayakkara, C.-S. Jiang, J. M. Luther, J. J. Berry, M. C. Beard, M. M. Al-Jassim and K. Zhu, *Energy Environ. Sci.*, 2017, **10**, 1234–1242.
315 T. Zhang, H. Chen, Y. Bai, S. Xiao, L. Zhu, C. Hu, Q. Xue and S. Yang, *Nano Energy*, 2016, **26**, 620–630.
316 T. Zhang, C. Hu and S. Yang, *Small Methods*, 2020, **4**, 1900552.
317 Q. Jiang, M. Chen, J. Li, M. Wang, X. Zeng, T. Besara, J. Lu, Y. Xin, X. Shan and B. Pan, *ACS Nano*, 2017, **11**, 1073–1079.
318 S. Cao, H. Wang, H. Li, J. Chen and Z. Zang, *Chem. Eng. J.*, 2020, **394**, 124903.
319 Q. JIANG, *Nat. Energy*, 2016, **2**, 1–7.
320 K. Jung, W.-S. Chae, Y. C. Park, N.-G. Park and M.-J. Lee, *Chem. Eng. J.*, 2021, **409**, 128215.
321 J. Chen, J. Zhang, C. Huang, Z. Bi, X. Xu and H. Yu, *Chem. Eng. J.*, 2021, **410**, 128436.

322 L. Lin, T. W. Jones, J. T. W. Wang, A. Cook, N. D. Pham, N. W. Duffy, B. Mihaylov, M. Grigore, K. F. Anderson and B. C. Duck, *Small*, 2020, **16**, 1901466.

323 D. Aidarkhanov, Z. Ren, C.-K. Lim, Z. Yelzhanova, G. Nigmetova, G. Taltanova, B. Baptayev, F. Liu, S. H. Cheung and M. Balanay, *Sol. Energy Mater. Sol. Cells*, 2020, **215**, 110648.

324 H. Wang, F. Li, P. Wang, R. Sun, W. Ma, M. Chen, W. Miao, D. Liu and T. Wang, *Adv. Energy Mater.*, 2020, **10**, 2000615.

325 X. Ye, H. Cai, J. Su, J. Yang, J. Ni, J. Li and J. Zhang, *J. Mater. Sci. Technol.*, 2020, **61**, 213–220.

326 D.-Y. Son, S.-G. Kim, J.-Y. Seo, S.-H. Lee, H. Shin, D. Lee and N.-G. Park, *J. Am. Chem. Soc.*, 2018, **140**, 1358–1364.

327 Z. Tang, S. Uchida, T. Bessho, T. Kinoshita, H. Wang, F. Awai, R. Jono, M. M. Maitani, J. Nakazaki and T. Kubo, *Nano Energy*, 2018, **45**, 184–192.

328 M. Gratzel, *Nature*, 2001, **414**, 338–345.

329 Q. Jiang, D. Rebollar, J. Gong, E. L. Piacentino, C. Zheng and T. Xu, *Angew. Chem.*, 2015, **127**, 7727–7730.

330 M. Zhang, F. Wu, D. Chi, K. Shi and S. Huang, *Mater. Adv.*, 2020, **1**, 617–624.

331 X. Huang, J. Du, X. Guo, Z. Lin, J. Ma, J. Su, L. Feng, C. Zhang, J. Zhang and J. Chang, *Sol. RRL*, 2020, **4**, 1900336.

332 Y. Wang, C. Duan, X. Zhang, N. Rujisamphan, Y. Liu, Y. Li, J. Yuan and W. Ma, *ACS Appl. Mater. Interfaces*, 2020, **12**, 31659–31666.

333 Z. Chen, Z. Zhang, J. Yang, W. Chen, Z. L. Teh, D. Wang, L. Yuan, J. Zhang, J. A. Stride and G. J. Conibeer, *J. Mater. Chem. C*, 2018, **6**, 9861–9866.

334 M. Zhu, X. Liu, S. Liu, C. Chen, J. He, W. Liu, J. Yang, L. Gao, G. Niu, J. Tang and J. Zhang, *ACS Appl. Mater. Interfaces*, 2020, **12**, 2566–2571.

335 N. H. Nickel, F. Lang, V. V. Brus, O. Shargaieva and J. Rappich, *Adv. Electron. Mater.*, 2017, **3**, 1700158.

336 H. Shan, E. Rezaee, X. Leng, X. Wang, Q. Chen and Z. X. Xu, *ChemSusChem*, 2018, **11**, 3000–3006.

337 H. Hussain, G. Tocci, T. Woolcot, X. Torrelles, C. Pang, D. Humphrey, C. Yim, D. Grinter, G. Cabailh and O. Bikondoa, *Nat. Mater.*, 2017, **16**, 461–466.

338 B. Roose, J.-P. C. Baena, K. C. Gödel, M. Graetzel, A. Hagfeldt, U. Steiner and A. Abate, *Nano Energy*, 2016, **30**, 517–522.

339 B. Roose, C. M. Johansen, K. Dupraz, T. Jaouen, P. Aebi, U. Steiner and A. Abate, *J. Mater. Chem. A*, 2018, **6**, 1850–1857.

340 R. Liu, L. Wang, Y. Fan, Z. Li and S. Pang, *RSC Adv.*, 2020, **10**, 11551–11556.

341 P. Hang, J. Xie, G. Li, Y. Wang, D. Fang, Y. Yao, D. Xie, C. Cui, K. Yan and J. Xu, *Iscience*, 2019, **21**, 217–227.

342 M. M. Tavakoli, F. Giordano, S. M. Zakeeruddin and M. Gratzel, *Nano Lett.*, 2018, **18**, 2428–2434.

343 D. P. McMeekin, G. Sadoughi, W. Rehman, G. E. Eperon, M. Saliba, M. T. Hörantner, A. Haghighirad, N. Sakai, L. Korte and B. Rech, *Science*, 2016, **351**, 151–155.

344 J. Chen, X. Zhao, S.-G. Kim and N.-G. Park, *Adv. Mater.*, 2019, **31**, 1902902.

345 K. Choi, J. Lee, H. I. Kim, C. W. Park, G.-W. Kim, H. Choi, S. Park, S. A. Park and T. Park, *Energy Environ. Sci.*, 2018, **11**, 3238–3247.

346 Y. Guo, H. Lei, C. Wang, J. Ma, C. Chen, X. Zheng, G. Yang, L. Xiong and Z. Tan, *Sol. RRL*, 2020, **4**, 1900482.

347 S. Mu, Q. Ye, X. Zhang, S. Huang and J. You, *Front. Optoelectron.*, 2020, **13**, 265–271.

348 C. Tian, K. Lin, J. Lu, W. Feng, P. Song, L. Xie and Z. Wei, *Small Methods*, 2020, **4**, 1900476.

349 W. Zhang, Y. Li, X. Liu, D. Tang, X. Li and X. Yuan, *Chem. Eng. J.*, 2020, **379**, 122298.

350 Y.-W. Jang, S. Lee, K. M. Yeom, K. Jeong, K. Choi, M. Choi and J. H. Noh, *Nat. Energy*, 2021, **6**, 63–71.

351 Q. Dong, M. Chen, Y. Liu, F. T. Eickemeyer, W. Zhao, Z. Dai, Y. Yin, C. Jiang, J. Feng, S. Jin, S. Liu, S. M. Zakeeruddin, M. Grätzel, N. P. Padture and Y. Shi, *Joule*, 2021, **5**, 1587–1601.

352 Q. Dong, C. Zhu, M. Chen, C. Jiang, J. Guo, Y. Feng, Z. Dai, S. K. Yadavalli, M. Hu, X. Cao, Y. Li, Y. Huang, Z. Liu, Y. Shi, L. Wang, N. P. Padture and Y. Zhou, *Nat. Commun.*, 2021, **12**, 973.

353 N. Ren, B. Chen, R. Li, P. Wang, S. Mazumdar, B. Shi, C. Zhu, Y. Zhao and X. Zhang, *Sol. RRL*, 2021, **5**, 2000795.

354 Y. Zhou, S. Yang, X. Yin, J. Han, M. Tai, X. Zhao, H. Chen, Y. Gu, N. Wang and H. Lin, *J. Mater. Chem. A*, 2019, **7**, 1878–1888.

355 Q. Dong, J. Li, Y. Shi, M. Chen, L. K. Ono, K. Zhou, C. Zhang, Y. Qi, Y. Zhou and N. P. Padture, *Adv. Energy Mater.*, 2019, **9**, 1900834.

356 D.-K. Lee, D.-N. Jeong, T. K. Ahn and N.-G. Park, *ACS Energy Lett.*, 2019, **4**, 2393–2401.

357 K.-S. Lim, D.-K. Lee, J.-W. Lee and N.-G. Park, *J. Mater. Chem. A*, 2020, **8**, 9345–9354.

358 B. Taheri, F. De Rossi, G. Lucarelli, L. A. Castriotta, A. Di Carlo, T. M. Brown and F. Brunetti, *ACS Appl. Energy Mater.*, 2021, **4**, 4507–4518.

359 S. Tian, J. Li, S. Li, T. Bu, Y. Mo, S. Wang, W. Li and F. Huang, *Sol. Energy*, 2019, **183**, 386–391.

360 T. Bu, X. Liu, J. Li, W. Huang, Z. Wu, F. Huang, Y.-B. Cheng and J. Zhong, *Sol. RRL*, 2020, **4**, 1900263.

361 G. Jang, H. C. Kwon, S. Ma, S. C. Yun, H. Yang and J. Moon, *Adv. Energy Mater.*, 2019, **9**, 1901719.